MECHANICAL PROPERTIES OF MULTI-YEAR SEA ICE

PHASE II: TEST RESULTS

Draft Report
May 1984

INTRODUCTION

This report presents the test results from the second phase of a continuing, government-industry study designed to obtain a comprehensive understanding of the structure and mechanical properties of ice samples obtained from multi-year pressure ridges. We are particularly interested in the mechanical properties of multi-year ice, as multi-year pressure ridges may govern the design of offshore structures in exposed areas of the Beaufort and Chukchi Seas.

The first phase of the study included a field sampling program in the Southern Beaufort Sea, the development of a variety of ice testing techniques, and performing a total of 282 uniaxial compression, tension, and conventional triaxial tests. In Phase I, the majority of the tests were uniaxial constant strain-rate compression tests. We were interested in determining the variation of ice strength within and between ten sampled ridges. These tests were performed at two strain rates (10^{-5} and 10^{-3} s^{-1}) and two temperatures (-20 and -5°C). In addition, a limited number of constant strain rate tension, constant load compression, and conventional triaxial tests were performed on ice samples obtained from a multi-year floe. These tests were performed to establish our testing techniques and procedures. The results from Phase I are given in three reports: Mellor et al. (1984) describe the testing techniques used in the program; Cox et al. (1984) present the test results; and Rand (In Prep) describes the coring equipment specially developed for this study to obtain 4 1/4-inch diameter core.

In Phase II, ice samples were again obtained from multi-year pressure ridges in the Beaufort Sea and shipped to CRREL for testing. As no significnt difference was found between the mean strength of ridges during Phase I, sampling was restricted to four ridges to simplify the logistics. Unlike Phase I, the tests in Phase II were divided among constant strain rate compression and tension, constant load compression and triaxial tests. A total of 188 tests were performed.

This report includes a discussion of the field sampling program and presents the tests results of the second phase of the program. The sample preparation and testing techniques used in Phase II have already been described in detail by Mellor et al. (1984).

FIELD SAMPLING PROGRAM

We had originally scheduled the field program for the first two weeks of April, as in Phase I. However, delays associated with establishing the funding level of the project prevented the field operation from starting until 14 April 1982. We were very concerned that a period of warm weather would cause us difficulties, such that we would have to pack the ice sample boxes with dry ice while at the sampling sites. Fortunately this did not occur. We were also favored with extremely good flying and working weather (limited ice fog and light winds). This good fortune combined with the fact that our coring systems performed extremely well allowed us to exceed our sampling goals and complete the program in 10 days. We mention this good fortune to stress the point that, in planning field programs, such optimal working conditions and system performance cannot be relied upon.

Under more typical conditions we would estimate that our field program could have taken up to 16 days to complete.

Site Selection and Description

During the winter of 1982, there were relatively few multi-year floes with suitable ridges in the Prudhoe Bay area. Fortunately, we were able to arrange for ice reconnaissance flights by Shell and Oceanographic Services. As these flights were completed before we arrived in Deadhorse, we were able to fly directly to the most likely locations in our area to select suitable ridges for sampling. Even so, we found it difficult to select suitable ridges as the majority of the multi-year floes were quite small and the ridges were unimpressive. In addition, many of the ridges appeared to be located on second-year ice. The ridge profiles were still somewhat blocky and the surfaces of the undeformed floes did not show well developed melt relief. Based on last year's sampling program, we found that second-year ridges contain a large number of voids that are only partially refilled with ice. Ice from such ridges provides relatively few good test specimens as it is difficult to obtain suitably long cores. We finally selected a floe north of Leavitt Island where several floes were located near to each other and contained several well-rounded ridges that we estimated to be at least two summers old (Fig. 1). The first sampling location (Ridge A) was on a thick multi-year floe with lateral dimensions of roughly 50 m. Although the ice had been deformed, there were no clearly delineated linear ridges. Therefore, we chose two of our sampling locations on high points and two sampling locations in swales. A sketch map showing the general topography of the sampling area is given in Figure 2.

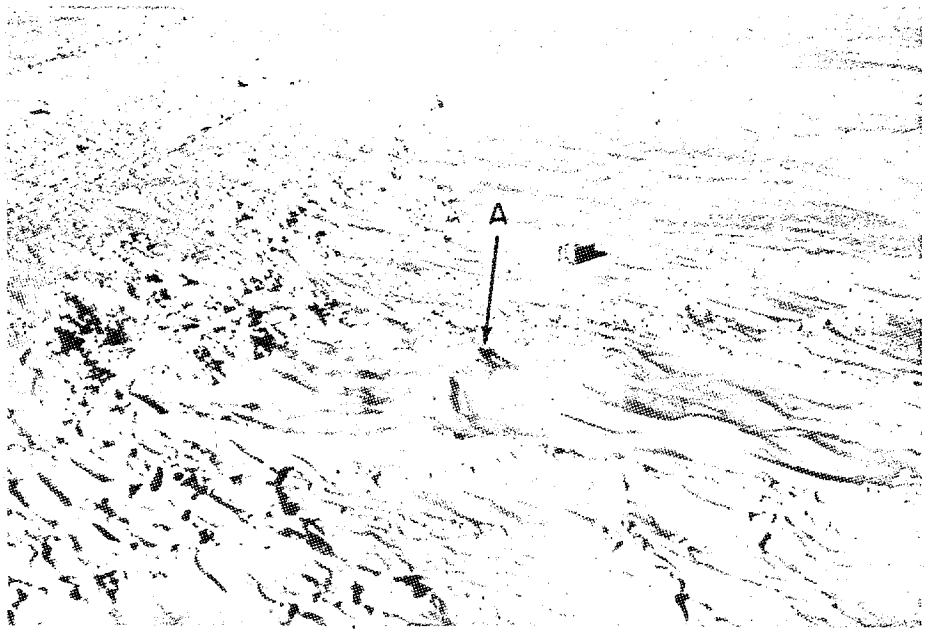

Figure 1: Aerial view of multi-year floe, designated as Ridge A, where first 11 cores were obtained.

THE MECHANICAL PROPERTIES OF MULTI-YEAR SEA ICE,

PHASE II: TEST RESULTS

by

G.F.N. Cox, J.A. Richter-Menge, W.F. Weeks, M. Mellor,
H.W. Bosworth, G. Durell and N. Perron

U.S. Army Cold Regions Research and Engineering Laboratory
72 Lyme Road
Hanover, NH 03755

prepared for

Shell Development Company

and

Minerals Management Service
U.S. Department of the Interior

Figure 3 shows an oblique aerial photograph of the site (located in the foreground). The small, one-room building (which was transported to the site by helicopter) provides a sense of scale. Figure 4 shows a surface view of the floe. The 1 to 1.5 m freeboard is evident. A total of 11 sites were sampled at this location for a total core length of 48.70 m. The ice at this location was generally characterized by a high volume of included air as compared with the ridges that we had sampled in 1981. We therefore decided to sample several other ridges in the vicinity to see if they also contained large amounts of air or perhaps would prove to be similar to the ridges we sampled during Phase I.

These ridges were found on two floes located approximately 200 m to the north of our first sampling area. The second ridge (Ridge B) was approximately 27 m long and was located on the smaller of these two floes (Fig. 5). It is possible that these two floes were initially part of the same larger floe, which had been split. The ice proved to be quite solid and massive with significantly less air voids. A sketch of a profile of this ridge showing the location of specific core sites is given in Figure 6. Note the sharp vertical termination of the ridge on the "right-hand" edge of the floe. The total length of core obtained from this ridge was 50.32 m.

The third ridge sampled was approximately 75 m long and was the largest ridge on the adjoining floe. A profile of this ridge (Ridge C) is given in Figure 7. Figure 5 shows an aerial view of this ridge (marked as C) as well as of Ridges B and D. Ridge C, although broad, was quite clearly defined. Figure 8 shows coring underway on this ridge. A total of

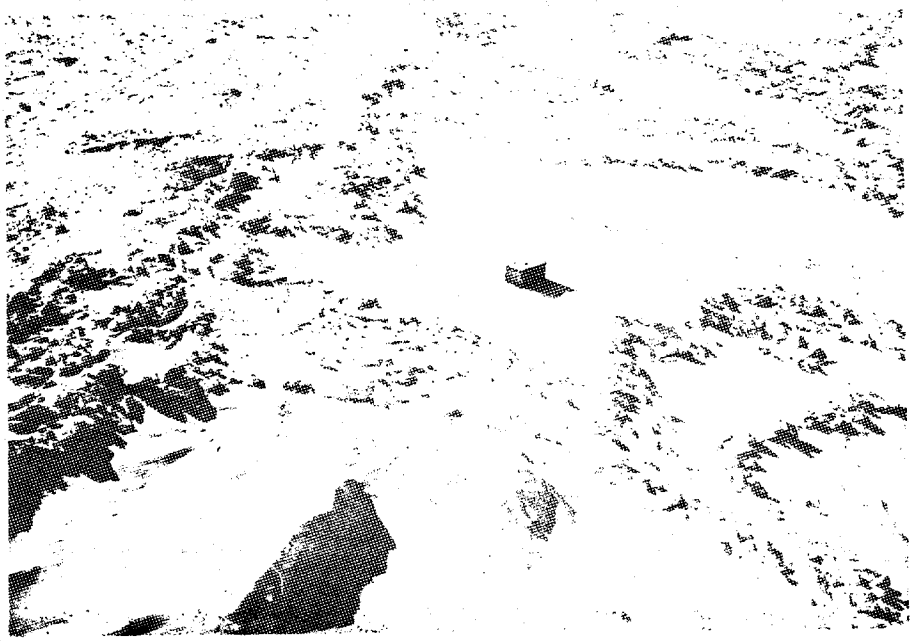

Figure 3: Oblique aerial view of Ridge A sampling site.

Figure 4: Surface view of Ridge A sampling site.

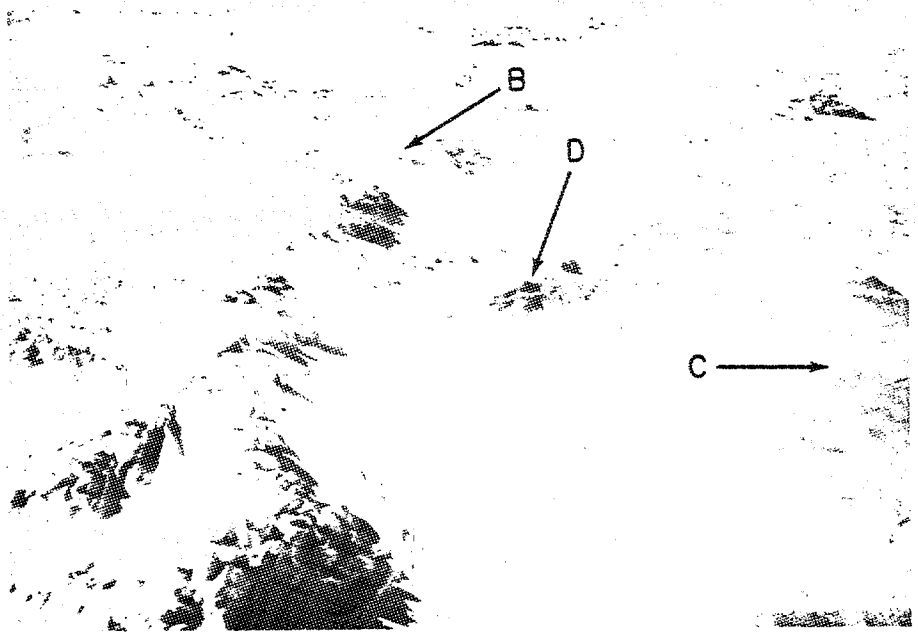

Figure 5: Aerial view of sampling area containing Ridges B, C, and D.

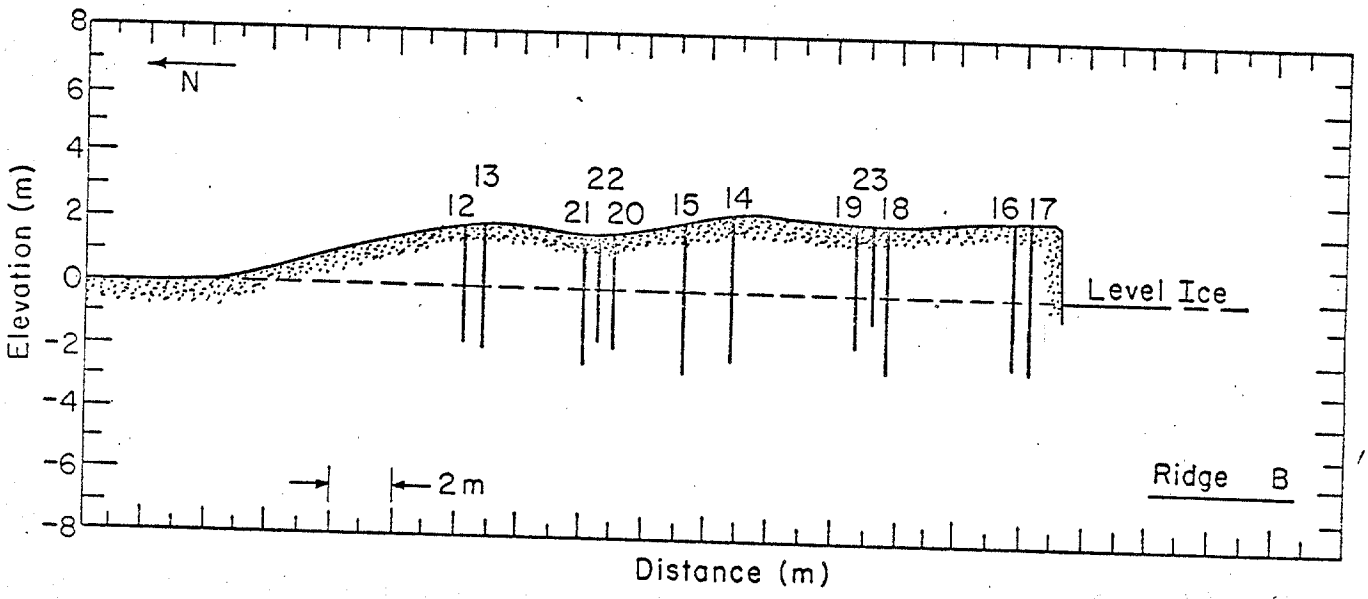

Figure 6: Sketch of Ridge B profile showing the location of the ice sampling sites.

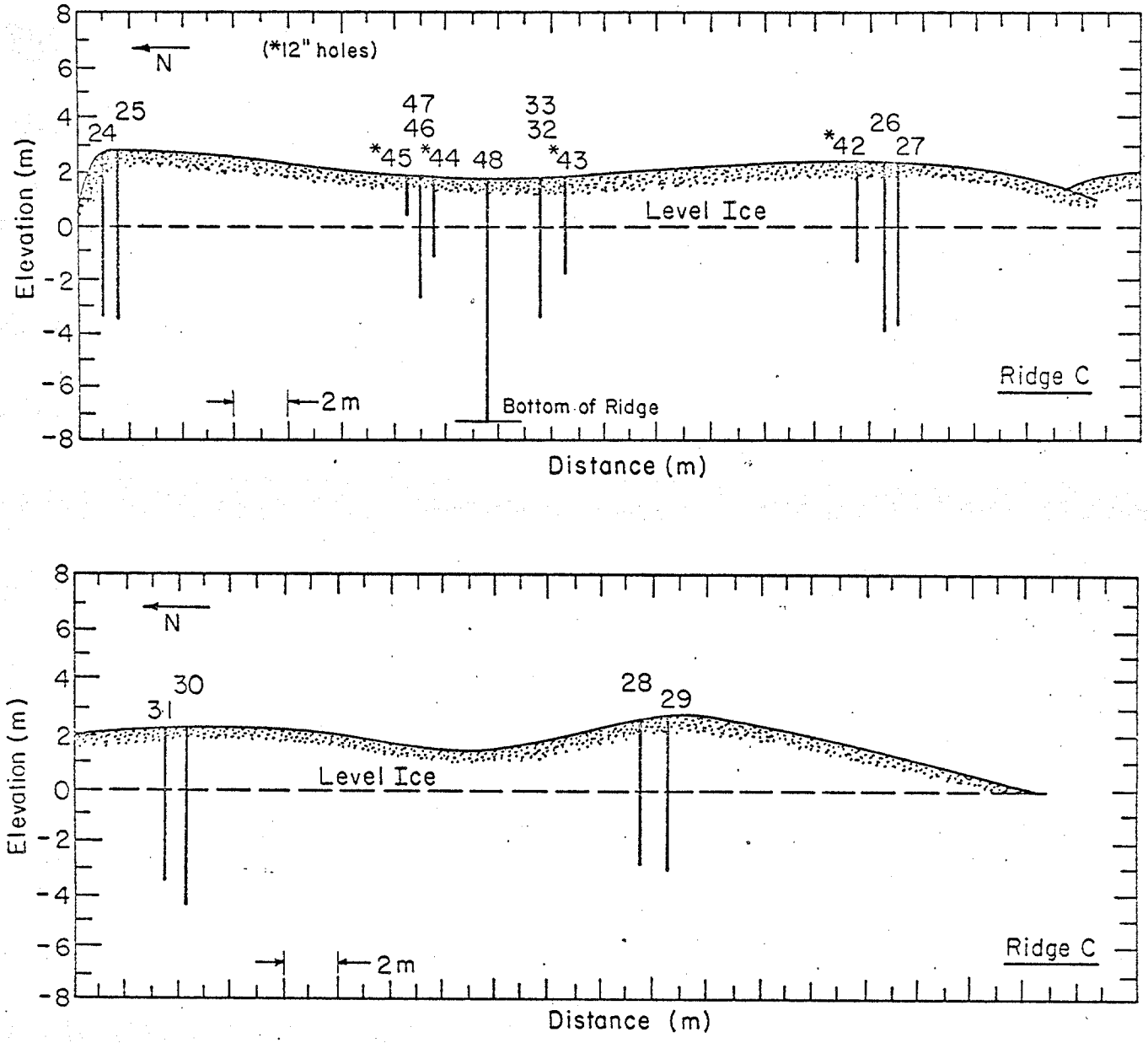

Figure 7: Sketch of Ridge C profile showing the location of the ice sampling sites.

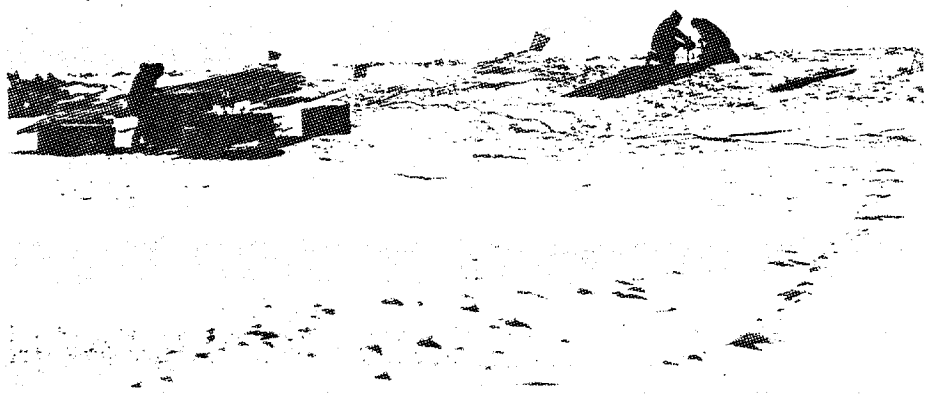

Figure 8: Coring operation on Ridge C.

67.11 m of core were obtained from this ridge for use as test specimens. A 9.53 m core was also obtained through the ridge to use in petrographic studies.

The last ridge sample ran roughly parallel to Ridge C. Ridge D can also be seen in Figure 5. This ridge was 53.6 m in length and was clearly delineated. Figure 9 shows the split end of the ridge where its blocky deformed structure could be examined. The total core recovery from Ridge D was 47.93 m.

In addition, 3.83 m of core were obtained from a floe which appeared to contain undeformed multi-year ice. Figure 10 shows an aerial view of the site. Table 1 summarizes the estimated height of the top of each core hole above level ice (approxiate sea level). Also given is the penetration depth (the total length cored from each hole). Table 2 gives the daily drilling log and Table 3 provides a summary of this data. The primary part of the coring program was carried out with the 4-1/4 in. corer in four days (15-18 April) with a total of 205.6 m of core recovered. The total number of vertical samples obtained from this core were 439 or roughly 100 samples per day. The total length of 12 in.-diameter core obtained was 12.79 m which resulted in 61 horizontal specimens giving a grand total of 500 specimens for the season. As mentioned earlier, we also obtained 8.75 m of core for petrographic studies.

Coring Procedures

Much of the success of the field program can be credited to the efficiency with which our coring equipment obtianed the samples. The 4-1/4 in. diameter coring augers were the same augers that were used in

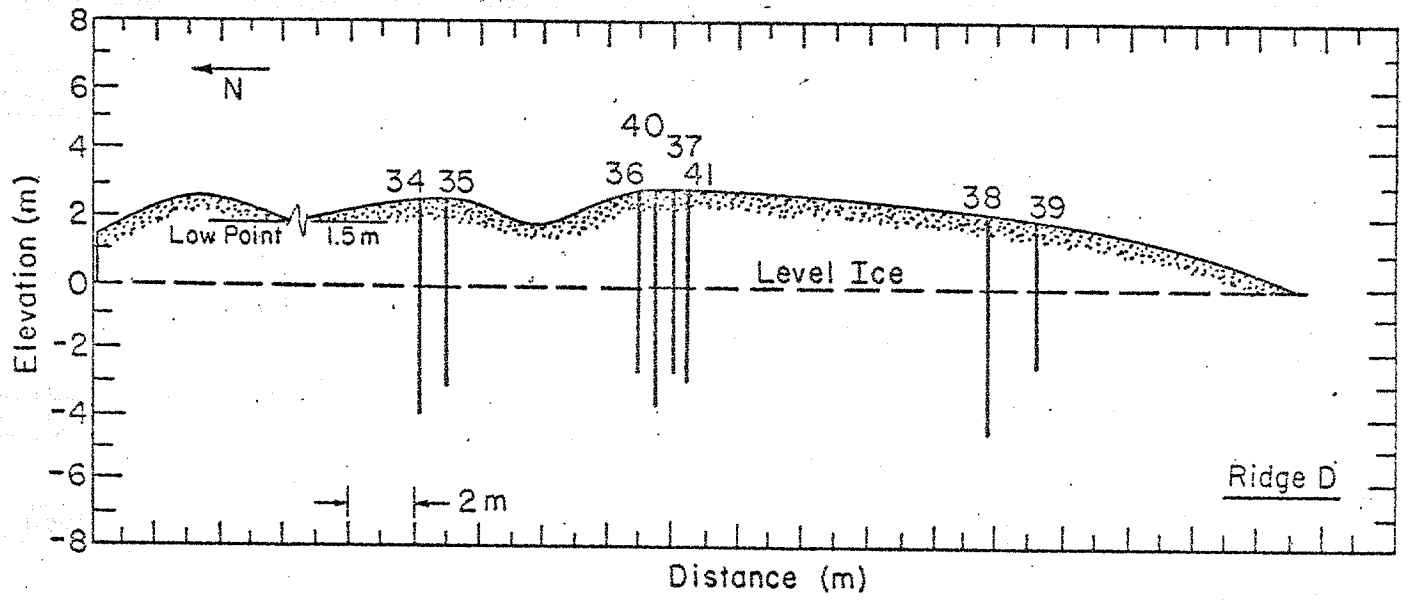

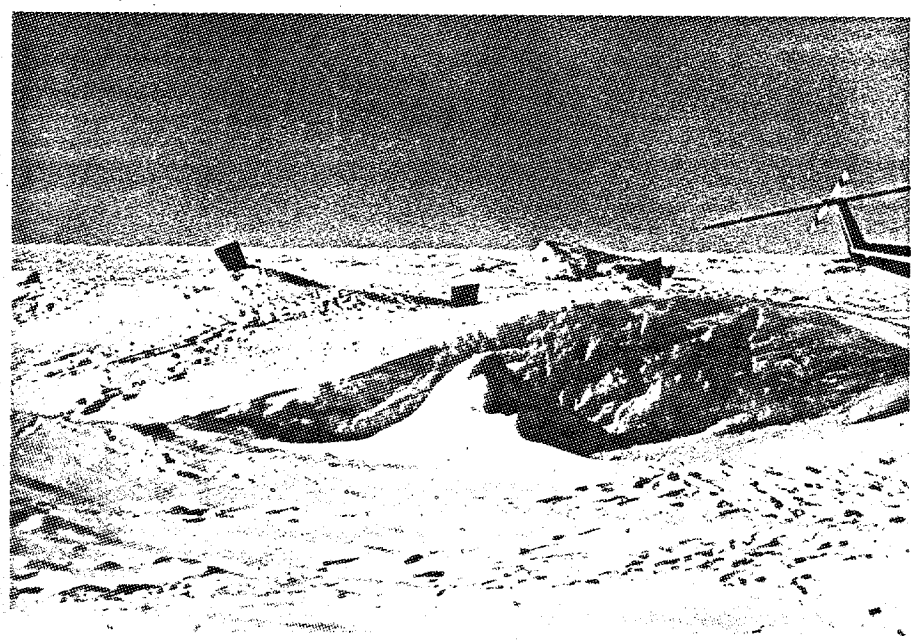

Figure 9: Split end portion of Ridge D.

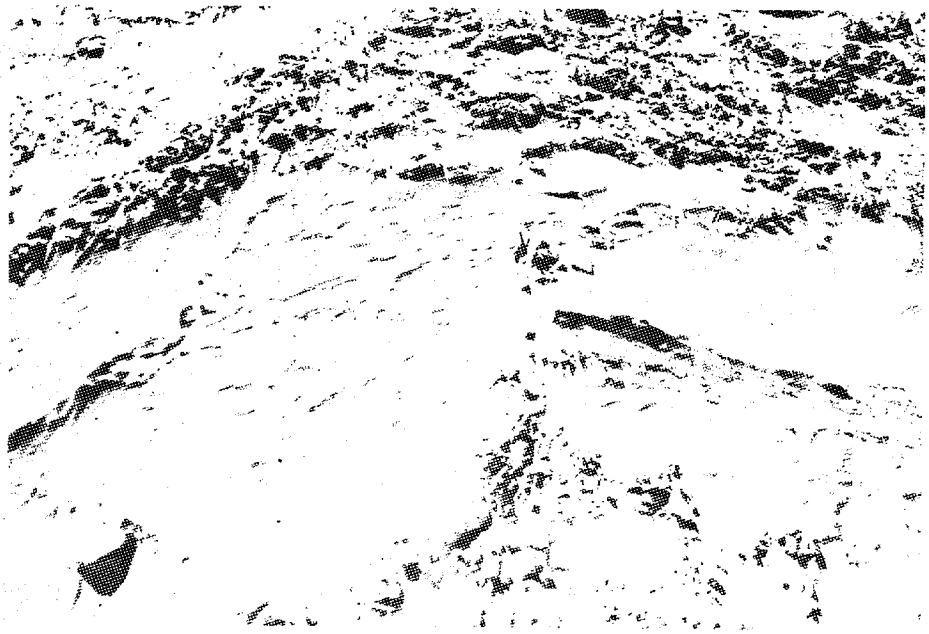

Figure 10: Aerial view of multi-year floe where undeformed samples were obtained.

Table 1. 1982 Ridge heights and penetration depths.

Location	Date	Hole #	Height (cm)	Depth (cm)	Height (ft)	Depth (ft)	Dia. (in.)	Remarks
RA	15 Apr 82	1	230	461	7.7	15.0	4.25	
		2	234	384	7.7	12.6	4.25	
		3	234	473	7.7	14.3	4.25	
		4	300	581	9.8	19.1	4.25	
		5	345	454	11.3	14.9	4.25	
		6	300	502	9.8	16.5	4.25	
		7	234	373	7.7	12.2	4.25	
		8	234	373	7.7	12.2	4.25	
		9	234	377	7.7	12.4	4.25	
		10	503	601	16.5	19.7	4.25	
		11	406	327	13.3	10.7	4.25	
RB	16 Apr 82	12	203	380	6.7	12.5	4.25	
		13	203	409	6.7	13.4	4.25	
		14	249	472	8.2	15.5	4.25	
		15	218	479	7.2	15.7	4.25	
		16	249	473	8.2	15.5	4.25	
		17	249	482	8.2	15.8	4.25	
		18	234	473	7.7	15.5	4.25	
		19	234	396	7.7	13.0	4.25	
		20	185	361	6.1	11.8	4.25	
		21	185	427	6.1	14.0	4.25	
		22	185	354	6.1	11.6	4.25	
		23	234	326	7.7	10.7	4.25	
RC	17 Apr 82	24	269	624	8.8	20.5	4.25	
		25	269	639	8.8	21.0	4.25	
		26	234	652	7.7	21.4	4.25	
		27	234	544	7.7	17.8	4.25	
		28	269	565	8.8	18.5	4.25	
		29	269	558	8.8	18.3	4.25	
		30	221	680	7.3	22.3	4.25	
		31	221	576	7.3	18.9	4.25	
		32	173	563	5.7	18.5	4.25	SL 163 cm/5.3 ft
		33	173	470	5.7	15.4	4.25	OD 1410 cm/46.3 ft
RD	18 Apr 82	34	269	676	8.8	22.2	4.25	
		35	269	564	8.8	18.5	4.25	
		36	300	567	9.8	18.6	4.25	
		37	300	577	9.8	18.9	4.25	
		38	218	682	7.2	22.4	4.25	
		39	218	466	7.2	15.3	4.25	
		40	300	678	9.8	22.2	4.25	
		41	300	583	9.8	19.1	4.25	
FC	19 Apr 82	42	234	404	7.7	13.3	12	
RC	20 Apr 82	43	173	389	5.7	12.8	12	SL 163 cm/5.3 ft
		44	173	323	5.7	10.6	12	"
		45	173	163	5.7	5.3	12	"

		46	173	364	5.7	11.9	4.25	"
		47	173	476	5.7	15.6	4.25	"
RC	22 Apr 82	48	173	953	5.7	31.3	4.25	"
RE	22 Apr 82	49	30	383	1.0	12.6	4.25	SL 53 cm/1.7 ft OD 1920 cm/63 ft

*SL = Sea level below top of hole
OD = Ocean depth

Table 2. Daily Core Log.
1982 Phase II Field Program.

Date	Ridge Location	Hole #	Drill used	Core lengths (cm)	Total depth (m)
4/15/82	RA	1	Blue 4-1/4	122, 108, 100, 94, 37	4.62
		2	"	122, 112, 97, 53	3.84
		3	"	119, 115, 98, 66, 39	4.37
		4	"	128, 102, 102, 94, 100, 55	5.81
		5	"	122, 93, 91, 102, 46	4.54
		6	"	126, 104, 100, 96, 76	5.02
		7	"	121, 112, 95, 45,	3.73
		8	"	127, 103, 105, 38	3.73
		9	"	125, 106, 99, 47	3.77
		10	"	127, 101, 105, 92, 105, 71	6.01
		11	"	74, 48, 98, 107	3.27
4/16/82	RB	12	Blue 4-1/4	127, 105, 56, 32, 40	3.80
		13	"	130, 91, 108, 80	4.09
		14	"	115, 111, 104, 96, 46	4.72
		15	"	118, 107, 106, 98, 50	4.79
		16	"	119, 105, 102, 101, 46	4.73
		17	"	118, 114, 98, 106, 46	4.82
		18	"	121, 105, 110, 92, 45	4.73
		19	"	110, 111, 102, 73	3.96
		20	"	122, 104, 98, 37	3.61
		21	"	121, 116, 103, 87	4.27
		22	"	126, 107, 96, 24	3.54
		23	"	121, 106, 99	3.26
4/17/82	RC	24	Orange 4-1/4	105, 113, 100, 106, 102, 98	6.24
		25	"	128, 102, 96, 101, 99, 113	6.39
		26	"	120, 114, 106, 114, 96, 102	6.52
		27	"	120, 126, 120, 80, 98	5.44
		28	"	117, 126, 124, 100, 98	5.65
		29	"	106, 109, 121, 116, 106	5.58
		30	"	114, 123, 100, 123, 110, 110	6.80
		31	"	121, 108, 115, 112, 120	5.76
		32	"	110, 110, 116, 110, 117	5.63
		33	"	126, 107, 121, 116	4.70
4/18/82	RD	34	Orange 4-1/4	114, 119, 111, 106, 123, 103	6.76
		35	"	115, 110, 109, 120, 110	5.64
		36	"	110, 117, 122, 113, 105	5.67
		37	"	116, 112, 125, 114, 110	5.77
		38	"	122, 111, 122, 113, 120, 94	6.82
		39	"	121, 112, 112, 121	4.66
		40	"	120, 123, 112, 124, 89, 110	6.78
		41	"	120, 114, 122, 124, 103	5.83
4/19/82	RC	42	Blue 12"	96, 82, 100, 60, 66	4.04
4/20/82	RC	43	"	103, 80, 88, 52, 66	3.89
		44	"	94, 102, 71, 56	3.23

		45	"	101, 62	1.63
		46	Orange 4-1/4	120, 122, 122	3.64
		47	"	121, 117, 124, 114	4.76
4/21/82	No drilling		High Winds	Blowing Snow	
4/22/82	RC	48	Orange 4-1/4	112, 116, 124, 113, 112, 102, 46, 58, 103, 67*	9.53
	RE	49	Orange 4-1/4	114, 30, 100, 68, 66*	3.83

*Denotes bottom of pressure ridge.

Table 3. Summary of daily drilling.

Date	Drill	# Holes	# Cores	Average core length (cm)	Total length of core obtained (m)
4/15/82	Blue 4-1/4	11	52	93	48.7
4/16/82	Blue 4-1/4	12	53	95	50.32
4/17/82	Orange 4-1/4	10	53	110	58.71
4/18/82	Orange 4-1/4	8	42	114	47.93
4/19/82	Blue 12 in.	1	5	81	4.04
4/20/82	Blue 12 in.	3	11	79	8.75
	Orange 4-1/4	2	7	120	8.4
4/22/82	Orange/Blue 4-1/4	2	13	92	13.36

Total length of 4 in. diameter core obtained - 226.09 m
Total length of 12 in. diameter core obtained - 12.79 m
Longest 4 in. diameter core obtained - 128 cm; hole no. 25
Longest 12 in. diameter core obtained - 103 cm; hole no. 43

1981, with some important modifications. In 1981, we experienced difficulty with the core dogs. They did not grip the sample firmly to produce a clean break at the base of the core. Instead the dogs frequently formed long gouges in the sides of the samples. These gouges were of sufficient depth such that the gouged ice could not be used for test specimens. During the 1982 field season, this problem was resolved. A new core dog was designed and fabricated to provide a more aggressive cutting edge. An inverted impact hammer was also added to give the extension rods a sharp upward impact. This impact both seated the dogs and caused the core to break cleanly at the bottom of the hole. Figure 11 shows the impact hammer in use. A third change that was made to the 4-1/4 inch coring system included the addition of a short length of helical flighting directly above the augers. This kept snow from packing into the top of the core barrel and reduced the friction when the core barrel was being removed from the hole. The helical flighting can be seen in Figure 12. We believed that this attachment allowed the drillers to obtain longer cores ranging from 100 cm to a maximum 128 cm.

The major addition to the coring equipment in Phase II was a 12-in. diameter coring system. Large diameter core was needed to provide horizontal test specimens from deep within the ridges. The auger itself was designed to obtain 12-in. diameter samples up to 1 m in length. Simply stated, it was an exploded version of the 4 in. auger. Figure 13 shows the auger attached to the winch and drive system. A commercial, gasoline post hole digger was modified to provide the rotation and lifting requirements

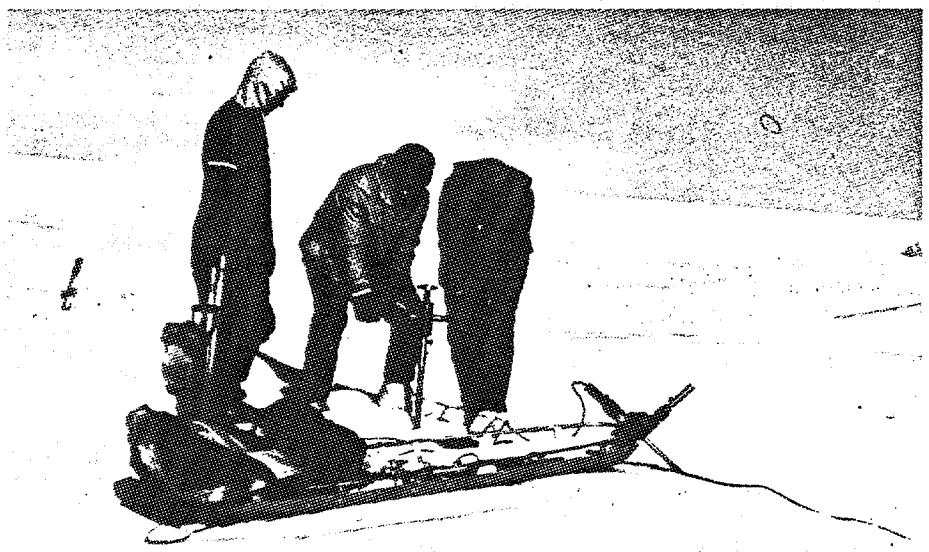

Figure 11: Impact hammer used to engage core dogs and break core.

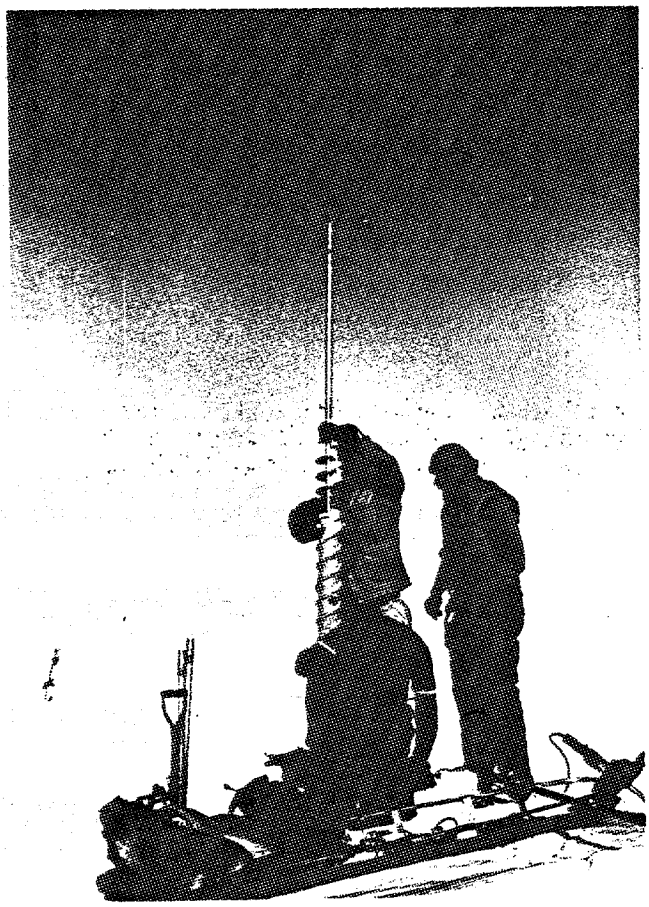

Figure 12: Helical flight on top of core barrel to prevent packing of cuttings above core barrel.

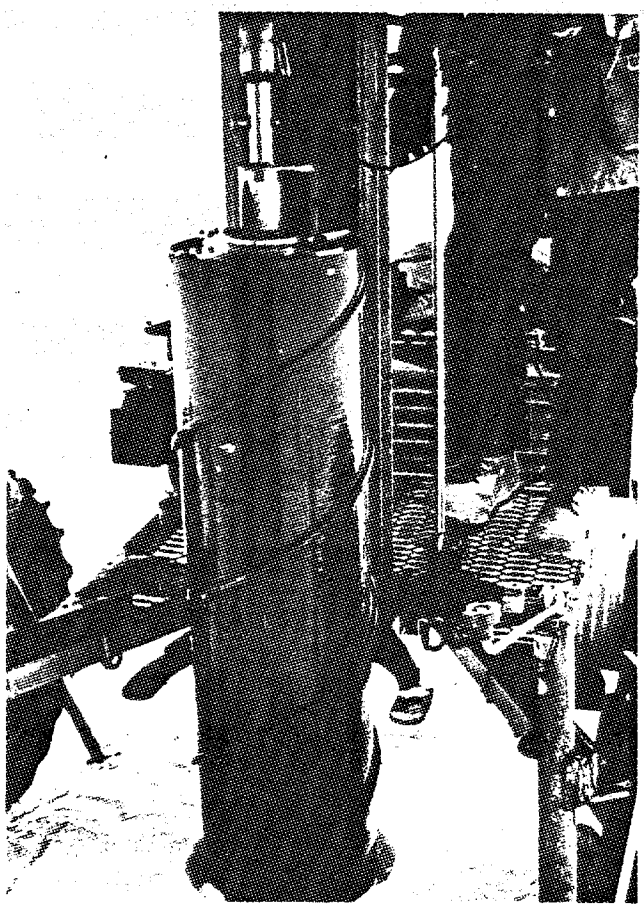

Figure 13: Twelve-inch diameter core barrel.

to operate the drill. Figure 14 shows the mobile drilling rig winching itself up a pressure ridge.

The following procedure was used to obtain the large diameter core and horizontal test samples. Once the drill had augered approximately 1 m, the drill was removed from the hole. A core retrieval system (Fig. 15) was then lowered into the hole to break and catch the core. A horizontally mounted hydraulic cylinder at the top of the core catcher was next activated to shear the core at the bottom of the hole. Two core dogs located at the bottom of the catcher retained the core in the barrel as it was lifted to the surface. The core was then removed from the retrieval system (Fig. 16) and placed in a (log) carrier to move the core to the horizontal sampling drill. To obtain horizontal samples, a simple drill press was designed such that 4-1/4 in. diameter cores could be obtained from the 12 in. core. Figure 17 shows this system in operation. The only problem encoutered while using this system was vibration of the horizontal sampling drill. This can be easily corrected by adding additional stiffening elements to the drill frame.

The entire 12 in. drilling system was transported to the sampling site by sling-loading the mobile frame under a helicopter. Once on the ground, a winching system allowed the operators to maneuver the system to the drilling location.

Core Logging Procedures

There were some differences in the core logging procedures between the 1981 and 1982 field seasons. As a result of the Phase I testing program, we had found that some of our field measurements did not prove to be

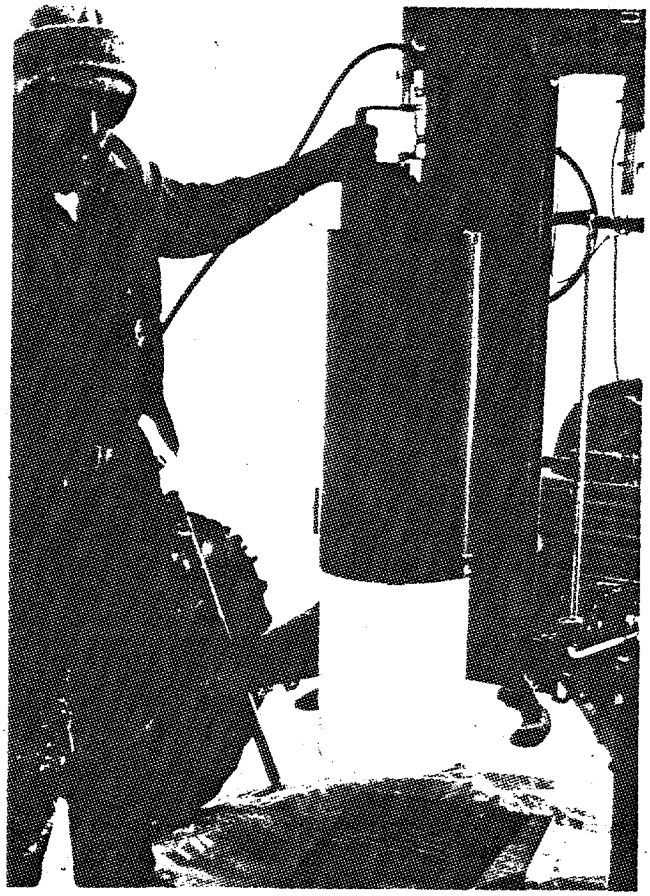

Figure 15: Core catcher used to break and retrieve 12-inch diameter core.

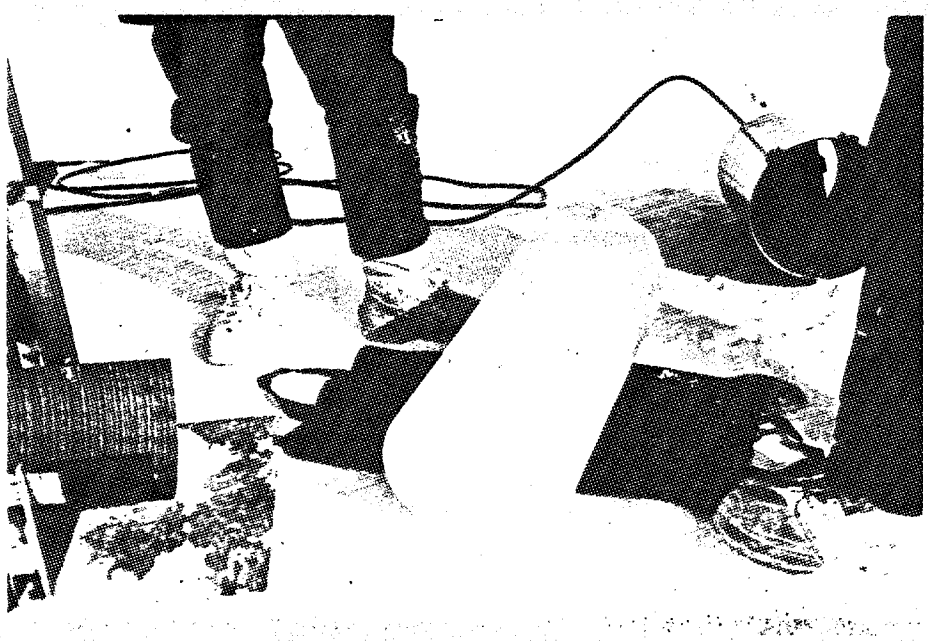

Figure 16: Removing 12-inch diameter core from core catcher.

Figure 17: Drill press used to obtain horizontal samples from the 12-inch diameter core.

particularly useful. For instance, in 1981, we took rather detailed temperature and salinity profiles in the field. As the important temperature is the ice temperature at the time of testing, we reduced the number of temperature measurements in the field to three or four per core in 1982. This was sufficient to indicate the general temperature profile in the ice. We also reduced the number of subsidiary salinity measurements. We have found that brine drainage is not an important problem in low salinity multi-year ice and our routine laboratory procedures include a salinity determination on each test specimen.

In 1981, we shipped large quantities of extra core back to CRREL for use in petrographic studies. Much of this core had been damaged during extraction when the extended core dogs gouged the core sides instead of cleanly breaking the core off at the bottom of the hole. Such core could not be used for test specimens. In 1982, this problem was resolved and very little damaged core was obtained. We also had found that we were able to save sufficient ice from each 33 cm rough-cut test specimen as collected in the field to prepare the necessary subsidiary thin sections. Therefore, it was not necessary to ship extra-long test specimens or to include extra ice from each core. Samples were cut to 33 cm lengths in the field and extra ice was not included. This resulted in a great saving in time and in shipping costs.

Shipping and Storage of Ice Samples

The ice samples were packed in core tubes and placed in insulated boxes. They were temporarily stored in Deadhorse and then shipped in two consignments from Deadhorse to Boston and on to Hanover.

Upon removal from the ice, ice cores were cut to length, catalogued, and packed in core tubes. In Deadhorse, gaps in the core tubes were packed with paper to protect the core ends from damage due to excessive motion during shipment. The core tubes were then placed in insulated shipping boxes. The core shipping boxes were constructed of heavy-weight, wax-coated cardboard with three-inch thick styrofoam on the bottom, sides, and top of the container. Each box could accomodate six, meter-long tubes, snow for packing, and dry ice for refrigeration. The shipping boxes were kept in an unheated trailer at ambient temperatures. As temperatures were sufficiently cold, it was not necessary to refrigerate the samples. No problems were experienced with brine drainage.

The ice samples were shipped directly to CRREL in two consignments. Each shipping box was packed with two to three inches of snow and charged with about 75 lbs of dry ice. The snow was placed on top of the core tubes to prevent thermal cracking of the core that might result from direct contact with the dry ice.

The ice samples were shipped via Alaska International Air Cargo (AIA) to Emery Air Freight in Anchorage. Before each shipment left Deadhorse, Emery reserved space on a Flying Tigers flight to Boston. In Anchorage, Emery transferred the cargo to Flying Tigers. CRREL personnel finally met each of the Flying Tiger flights in Boston with a refrigerated truck and transported the ice to Hanover.

Originally we have planned to store the ice in Anchorage, and then arrange for one shipment to Hanover, as we had done in Phase I. However, because of the delay of going into the field, we were not able to arrange

for refrigerated storage in Anchorage. The majority of the refrigerated space is owned by fishing companies, and the fishing season had already started. This problem acutally did us a favor as it forced us to ship directly to Boston, a procedure that was easier and successful. We plan to ship all ice samples directly from Deadhorse to Boston in the future.

ICE DESCRIPTION

Before presenting the results from the different mechanial property tests performed in Phase II, it is appropriate to examine the test material. This will facilitate our interpretation of the test results and make any comparisons to the Phase I data more meaningful.

In general, the ice samples collected during Phase II were different from the samples obtained during Phase I. The Phase II samples had a slightly lower density and contained more columnar ice. The average salinity of the samples collected during Phase I and II were similar.

Salinity and Density

Ice samples from Ridges A, B, and C were used in the Phase II test program. Average salinities and densities of the ice samples from these ridges are given in Table 4. The data are grouped according to whether the samples were obtained from the ridge sails (above level ice) or the ridge keels (below level ice). Average salinities and densities for each ridge and averages for all the samples are also given. Phase I data are included for comparisons.

The test samples from the pressure ridge sails had an average salinity of 0.8 °/oo and an average density of 0.841 Mg/m^3 at -20°C. The samples from the ridge keels had an average salinity of 1.89 °/oo and an averge

Table 4. Average salinity and density (-20°C) of ice samples obtained from Ridges A, B, and C during Phase II and all ridges from Phase I.

	Ridge A	Ridge B	Ridge C	Three Ridges	Phase I
Above Level Ice					
Salinity (°/oo)	0.08±0.14	0.86±0.56	1.68±1.06	0.77±0.91	0.71±0.57
Density (Mg/m^3)	0.807±0.032	0.850±0.038	0.879±0.030	0.841±0.045	0.875±0.032
Below Level Ice					
Salinity (°/oo)	0.89±0.46	1.66±0.91	2.68±1.11	1.89±1.16	1.56±0.77
Density (Mg/m^3)	0.877±0.024	0.888±0.018	0.894±0.018	0.888±0.020	0.899±0.018
Above and Below Level Ice					
Salinity (°/oo)	0.38±0.49	1.29±0.87	2.29±1.19	1.34±1.18	1.26±0.82
Density (Mg/m^3)	0.834±0.046	0.870±0.035	0.888±0.024	0.865±0.042	0.891±0.026

density of 0.888 Mg/m^3. The mean salinity and density of all the test samples were 1.3 °/oo and 0.865 Mg/m^3, respectively. Samples from Ridge A had a much lower average salinity and density than the test samples from Ridges B and C. This was particularly true for the samples collected from the pressure ridge sails.

Structure

While detailed structure analyses on all the test samples will not be performed unitl a later date, it was clearly evident that the ice samples collected during Phase II contained significantly more columnar ice than the samples obtained during Phase I. It is conceivable that in Phase I we mostly sampled highly granulated shear ridges, whereas in Phase II, we sampled compression ridges which contained large blocks of columnar sea ice.

Of the three ridges tested in Phase II, we have, at this time, only examined the structure of ice samples from Ridge C in a systematic manner. A continuous core was specifically obtained from Ridge C for petrograhic work. In addition, horizontal and vertical sample pairs were obtained from Ridge C for uniaxial compression tests. The structure of these samples was subsequently analyzed to explain the variation of ice strength between the sample pairs.

A detailed structural profile of the continuous core obtained from Ridge C is presented in Appendix A. The profile was prepared by splicing together photographs of vertical ice thin-sections which were taken in crossed polarized light. A few photographs of horizontal thin-sections are also presented. The salinity profile and a schematic structural profile of

the core are given in Figure 18. It should be noted that the core was obtained through the full thickness of the ridge, 9.53 meters.

The upper 40 cm of the core consists primarily of very porous, coarse columnar grains. Some fine grained granular material is mixed throughout this section. From 40 to 85 cm, the ice structure is mixed, made up of large pieces of columnar ice separated by fine granular crystals. At 85 cm, the core becomes 100% columanr with the direction of elongation of the crystals 0° from the vertical. The columnar grains are medium grained and unaligned at 85 cm. At 100 cm, the c-axes become aligned and the grain size of the crystals increases with depth to about 180 cm where a 3 cm thick band of brecciated ice is encountered. Below this band, the direction of elongation of the coarse columnar crystal changes to 10° from the vertical. Conceivably, this is another block of sea ice that was incorporated into the ridge. This block of columnar ice contains well defined, fine granular bands.

From 245 to 330 cm the ice is brecciated consisting of large fragments of columnar ice floating in a fine grained granular matrix. The columnar fragments are up to 10 cm in diameter. At 330 cm, the ice structure alternates between 50 cm thick bands of fine to coarse grained columnar ice and 20 to 50 cm thick bands of fine granular, mixed granular and columnar material. This sequence continues to about 650 cm.

At 650 cm, a 2 meter thick layer of brecciated ice is found containing both large and small columnar fragments. The remainder of the core is mostly columnar with some fine grained granular material mixed throughout the section.

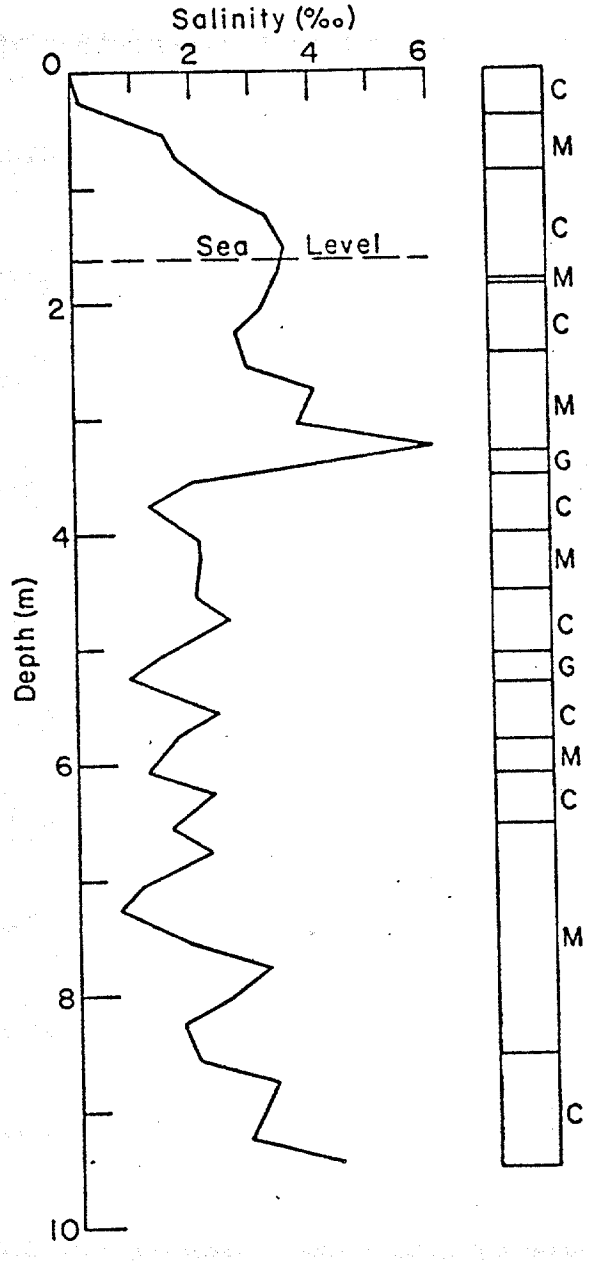

Figure 18: Salinity profile and schematic structural profile of continuous core from Ridge C. C denotes columnar ice; G is granular ice; and M is mixed ice, C and G.

About 50% of this multi-year pressure ridge core consists of columnar ice. The rest of the core is a combination of granular ice and mixed granular and columnar crystals. The mixed ice is predominatly brecciated. Only about one-third of the petrographic ridge core studied in Phase I contained well-defined columnar zones. In general, more columnar ice was encountered in the Phase II ice sampling program. As in Phase I, samples containing a variety of ice types were obtained and large, structure-dependent variations in the ice mechanical properties were anticipated.

CONSTANT STRAIN RATE COMPRESSION TESTS

Test Variables

Sixty-two constant strain-rate uniaxial compression tests were performed in Phase II. The tests were conducted at two strain-rates, 10^{-4} s^{-1} and 10^{-2} s^{-1}, and two temperatures, -20°C (-4°F) and -5°C (23°F), to supplement the tests performed in Phase I. In Phase I the compression tests were conducted at strain-rates of 10^{-5} s^{-1} and 10^{-3} s^{-1} and at temperatures of -20°C (-4°F) and -5°C (23°F). Unlike Phase I, tests in Phase II were performed on both horizontal and vertical samples to assess the effect of sample orientation on ice strength. The number of tests at each test condition is summarized in Table 5. Details on the sample preparation and testing techniques are given in Mellor et al. (1984). The procedure used in Phase II were identical to those used in Phase I.

Uniaxial Compressive Strength

A detailed tabulation of the results from the constant strain-rate, uniaxial compression tests is given in Appendix B. The average compressive strength of the ice is plotted against strain-rate in Figure 19 and 20.

Table 5. Number of uniaxial compression tests at different temperatures and strain-rates.

$\dot{\varepsilon}$ / T	10^{-4} s^{-1}	10^{-2} s^{-1}	
-5°C (23°F)	9V 10H	9V	18V 10H
-20°C (-4°F)	13V 12H	9V	22V 12H
Total	22V 22H	18V	40V 22H

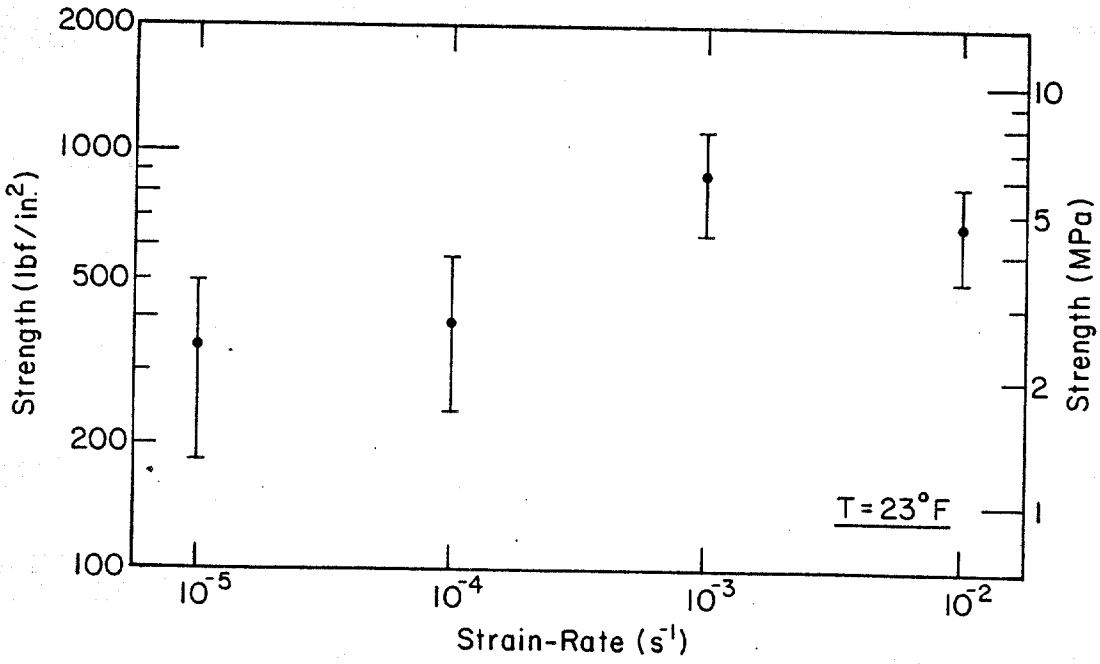

Figure 19: Uniaxial compression strength versus strain-rate for samples tested at -5°C (23°F). The bars denote one standard deviation.

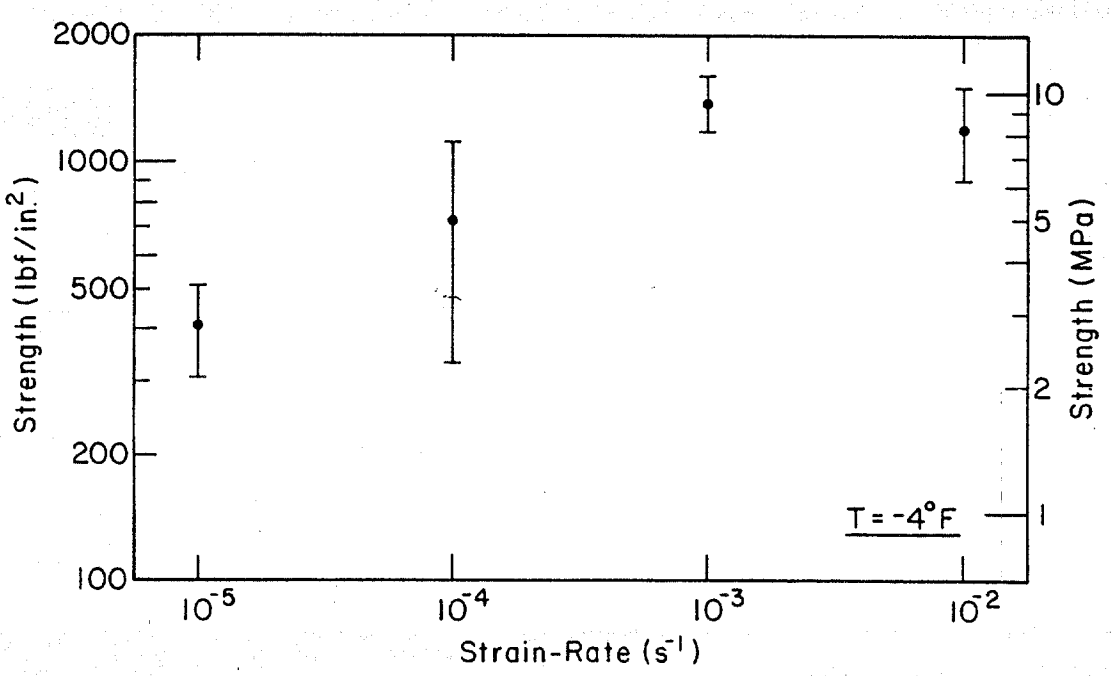

Figure 20: Uniaxial compressive strength versus strain-rate for samples tested at -20°C (-4°F). The bars denote one standard deviation.

Table 6. Summary of compressive strength data for Phases I and II.

	Uniaxial Compressive Strength							
	Maximum		Minimum		Mean		Mean Porosity	
	(MPa)	(lbf/in.^{2})	(MPa)	(lbf/in.^{2})	(MPa)	(lbf/in.^{2})	(ppt)	Samples
-5°C (23°F)								
10^{-5} s^{-1} V	7.52	1090	0.47	68	2.34±1.08	340±157	44	71
10^{-4} s^{-1} V	5.52	800	1.87	271	3.07±1.23	445±179	69	9
10^{-4} s^{-1} H	3.87	561	1.21	175	2.35±0.74	341±108	78	10
10^{-4} s^{-1} all	5.52	800	1.21	175	2.69±1.04	390±151	73	19
10^{-3} s^{-1} V	10.90	1580	2.39	346	6.06±1.63	879±237	46	69
10^{-2} s^{-1} V	6.42	931	2.69	390	4.67±1.17	677±169	68	9
-20°C (-4°F)								
10^{-5} s^{-1} V	4.26	617	1.17	170	2.79±0.69	404±100	36	41
10^{-4} s^{-1} V	12.73	1846	3.34	485	6.17±3.10	894±450	50	13
10^{-4} s^{-1} H	7.02	1018	1.68	243	3.74±1.67	543±242	33	12
10^{-4} s^{-1} all	12.73	1846	1.68	243	5.00±2.70	725±392	42	25
10^{-3} s^{-1} V	12.68	1838	7.03	1020	9.63±1.39	1396±202	39	41
10^{-2} s^{-1} V	10.48	1520	4.12	597	8.24±2.05	1195±297	74	9

H - Horizontal V - Vertical

Figure 19 contains the results from those tests conducted at -5°C (23°F), and Figure 20 contains the results from those tests conducted at -20°C (-4°F). The bars denote one standard deviation from the mean. The test results from Phase I at 10^{-5} and 10^{-3} are also included for comparison. Average strength values from Phases I and II are listed in Table 6.

At a given temperature and strain-rate, the Phase II strength data show considerable scatter. These large variations in strength can be explained by large variations in the ice structure and porosity (Richter and Cox, 1984). The strength of each specimen not only depends on the type of ice present in the specimen, which is highly variable from sample to sample, but also on the ice grain size and crystal orientation. Strength variations are further increased by variations in the ice porosity.

Based on our understanding of the variation of ice strength with strain-rate we would expect a power law relationship between ice strength and strain-rate in the ductile range (Mellor, 1983). On log-log paper, strength versus strain-rate would plot as a straight line. The combined average test results of Phases I and II at -5°C (23°F) do not show this tendency. The average strength of the 10^{-4} s^{-1} tests is lower than anticipated. However, at -20°C (-4°F) the 10^{-4} s^{-1} Phase II test average is in reasonable agreement with the 10^{-5} s^{-1} and 10^{-3} s^{-1} averages obtained in Phase I.

Since the strength of sea ice decreases with increasing porosity, it appears that the above observations can be explained in terms of the average ice porosity of the samples tested at each strain-rate and temperature. In Table 6 mean porosities are given for the samples tested

at each test condition. In can be seen that at -5°C (23°F), the 10^{-4} s^{-1} tests have a much higher porosity than the tests conducted at 10^{-5} s^{-1} and 10^{-3} s^{-1}. At -20°C (-4°F), the mean porosities of the 10^{-5} s^{-1}, 10^{-4} s^{-1}, and 10^{-3} s^{-1} are similar and the average strength values do show a power law relationship.

In both the -5 and -20°C (23 and -4°F) tests conducted at a strain-rate of 10^{-2} s^{-1}, there is an apparent decrease in ice strength relative to the tests conducted at 10^{-3} s^{-1}. We attribute this decrease in strength to the much larger porosity of the 10^{-2} s^{-1} samples.

Strength and Structure

In Phase II, the effect of structure on the compressive strength of multi-year ridge ice samples was further investigated in an effort to explain the difference in ice strength between horizontal and vertical samples. The horizontal and vertical samples were obtained in close proximity to one another and grouped in pairs according to sampling depth. Each pair was tested at the same strain-rate and temperature. A total of 44 tests conducted at a strain-rate of 10^{-4} s^{-1} were examined. Of these 44 tests, 19 tests were performed at -5°C (23°F) and 25 tests at -20°C (-4°F). The structural analysis was similar to that described in Phase I. Thin sections were prepared of both the tested sample and the end pieces adjacent to the test specimen. Ice type, grain size, and crystal orientation were determined by studying photographs of the thin sections taken in cross-polarized light. Additional photographs of the test specimen taken before and after the test were used to document the failure characteristics of the ice.

The strength, structure, and porosity of these samples are given in Tables 7 and 8. In these tables the vertical samples are denoted by a V and the horizontal samples by an H. The σ:z angle for the columnar samples is defined as the angle between the loading direction and the columns or elongated axes of the crystals. The σ:c angle is defined as the angle between the loading direction and the c-axes of the crystals. The angle measurements provided were estimated from the thin section photographs taken of each sample. The ice type classification is in accordance with the structural classification scheme established in Phase I. Porosity values were calculated using the relationship given by Cox and Weeks (1983) which related sample salinity, density, and temperature to sample porosity.

The results of the Phase II structural analysis were similar to the results of Phase I. However, the different nature of the Phase II ice and the horizontal and vertical pairs provided an opportunity to observe additional trends in the structure-to-strength relationship. In general, the Phase II ice was more porous and consisted of more well defined columnar blocks than the Phase I ice. Furthermore, the 10^{-4} s^{-1} samples, although randomly selected, were dominated by one ice type at each test temperature. The majority of the samples tested at 10^{-4} s^{-1} and -5°C (23°F) consisted of mixed or brecciated ice (Type III). The specimens at -20°C (-4°F) were mostly columnar (Type IIA).

Our observations on the structural variation of ice strength for columnar samples tested at -20°C (-4°F) are in agreement with the findings of Peyton (1966) and Wang (1979). Columnar samples loaded parallel to the

Table 7. Strength, structure, and porosity of horizontal and vertical sample pairs tested at 10^{-4} s^{-1} and -20°C (-4°F).

Sample No.	Strength ($lbf/in.^2$)	Ice Type	Average Grain Size (mm)	Porosity (°/oo)
RC32-231/258V	963	IIA Aligned σ:z=15°	30x15	46.2
RC43-245H	546	IIA Aligned σ:z=90°, σ:c=0°	30x7	29.9
RC32-267/294V	661	IIA Aligned σ:z=15°	42x20	42.1
RC33-268/295V	899	IIA Aligned σ:z=15°	25x12	24.0
RC43-280H	708	IIA Aligned σ:z=90°, σ:c=0°	30x10	38.5
RC32-303/328V	573	IIIB 60% Granular 40% Columnar	Granular <1	64.1
RC43-316H	342	IIA Aligned σ:z=90°, σ:c=20°	60x20	29.8
RC32-343/396V	485	III		88.5
RC43-357H	597	IIIB 60% Granular 40% Columnar	Granular <1	58.7
RC33-242/268V	947	IIA σ:z=20°	45x15	30.1
RC43-257H	541	IIA Aligned σ:z=90°, σ:c=0°	30x15	24.4
RC33-368/395V	939	III		40.6
RC43-381H	867	III		31.0
RC46-121/147V	517	IIIB 50% Granular	Granular <1	72.1
RC44-128H	255	IIA Aligned σ:c=35°	48x22	28.4

RC46-173/199V	493	IIIB 60% Granular	Granular <1	70.4
RC44-186H	1018	IIA Aligned σ:z=0°, σ:c=90°	50x18	31.6
RC46-276/303V	629	IIIB 60% Granular	Granular <1	68.7
RC44-299H	609	IIIB 70% Granular	Granular <1	48.9
RC47-090/116V	1798	IIA Aligned σ:z=0°	35x10	41.0
RC44-103H	505	IIA Aligned σ:z=90°, σ:c=0°	40x12	34.8
RC44-116H	243	IIA Aligned σ:z=90°, σ:c=35°	40x12	25.3
RC47-127/153V	1846	IIA Aligned σ:z=90°	45x10	36.0
RC44-141H	287	IIA Aligned σ:z=90°, σ:c=35°	45x12	16.6
RC47-302/329V	875	Type III: Top III Middle-Bottom IIA Aligned σ:z=0	65x20	23.5

Table 8. Strength, structure, and porosity of horizontal and vertical sample pairs tested at 10^{-4} s^{-1} and -5°C (23°F).

Sample No.	Strength ($lbf/in.^2$)	Ice Type	Average Grain Size (mm)	Porosity (°/oo)
RC32-133/160V	330	IIIB 50% Granular 50% Columnar	Granular <1	78.8
RC43-150H	386	IIIB 80% Granular	Granular ≤1	104.0
RC33-205/232V	478	TYPE IIIB: Top II Aligned σ:z=0° Middle I (30%) Bottom IIA σ:z=20°	50x10 ≤1 20x6	70.6
RC43-222H	402	III 70% Granular 30% Columnar	Granular ≤1	60.4
RC46-047/073V	362	TYPE IIIB: Top-Middle IIIB 70% Granular Bottom IIA Aligned σ:z=10°	30x10	63.3
RC44-073H	326	IIIA 20% Granular 80% IIA σ:z=90°	Granular ≤1 Columnar 25x10	86.2
RC44-060H	227	III 60% IIA Aligned σ:z=90°, σ:c=55° 40% IIIB	28x7	127.7
RC46-083/110V	800	IIIA 90% IIA Aligned σ:z=0° 10% Granular	35x12 <1	66.7
RC44-086H	390	IIA Aligned σ:z=90°, σ:c=90°	30x10	25.8

RC46-147/173V	271	IIA Aligned σ:z=25°	30x8	69.7
RC44-156H	175	IIIA 90% IIA Aligned σ:z=90°, σ:c=30°	45x12	54.0
RC46-246/272V	446	IIIA 90% IIA Aligned σ:z=5°	30x10	76.5
RC44-256H	271	IIIB 30% Granular	Granular <1	56.4
RC47-025/053V	322	TYPE IIIB: Top IIA Aligned σ:z=90° Middle I (20%) Bottom II-Aligned σ:z=90°	50x15 <1 25x8	81.8
RC45-040H	306	IIIA Vertical crack 90% IIA Aligned σ:z=90°, σ:c=75°	22x10	42.2
RC47-191/217V	669	IIIA 90% IIA Aligned σ:z=15°	35x10	50.2
RC44-204H	561	IIIA 90% IIA		46.7
RC47-275/302V	326	IIA σ:z=20°	Top-Middle 20x15 Bottom 18x8	59.9
RC44-288H	366	IIIB 50% Granular	Granular <1	73.5

elongated crystal axes and normal to the c-axis were extremely strong. Specimens loaded perpendicular to the elongated axes and parallel or normal to the c-axis had a significantly lower strength value. As the angle between the c-axis and the applied load approached 45° in these columnar samples, the strength decreased further. The compressive strength of the mixed and granular ice samples tested at these conditions was comparable to the strength of horizontal columnar samples loaded in the strong direction (σ:z=90 and σ:c=0° or σ:c=90°). The mixed and granular specimens also tended to decrease in strength as the ice porosity increased.

The mixed ice samples tested at -5°C (23°F) were very blocky in nature. It became apparent that the orientation of columnar blocks within the sample had an influence on the strength value. If the columnar ice in the sample was oriented with the elongated crystal axes parallel to the load, the sample failed at a relatively high load (comparable to the strength of a σ:z=90°, σ:c=0° loading in a columnar sample). As the angle between the elongated axes approached 45°, the strength of the mixed brecciated ice decreased.

The difference in strength between horizontal and vertical pairs was also found to depend on the ice structure. In general, the vertical samples had a higher strength value. At -5°C (23°F) the average strength of the vertical samples was 30% higher. At -20°C (-4°F) the average strength of the vertical and horizontal samples differed by 65%. The most significant differences in strength occurred in sample pairs of columnar ice.

Our observations indicate that many of the columnar ice blocks in a multi-year ridge lie horizontally or in a near horizontal position. In this position, large ice blocks in a ridge are the most stable. Consequently, a substantial number of the vertically oriented columnar samples have vertical elongation and a high strength. Horizontal columnar samples tend to have an angle of 90° between the long columns and the applied load and a much lower strength. Work by Peyton (1966) has also shown that strength values can differ between these two loading orientations by as much as a factor of three. Should additional field studies of block orientation in first-year and multi-year pressure ridges show a preference for horizontal block orientation, it may be justifiable to use lower ice force values for in-plane ridge loading on structures. Utilization of strength data from vertically orientation specimens would be conservative.

In general, sample pairs of mixed and granular ice had comparable strength values. As many of these samples appear to be isotropic, this is not surprising. Some vertical samples tended to have slightly higher strength. This may be the influence of internal columnar fragment orientations as discussed earlier.

Strength and Porosity

The compressive strength of the samples is plotted against the total porosity of the ice in Figures 21 through 24. The air and brine volume equations given in Cox and Weeks (1983) were used to calculate the ice porosity from the ice salinity, temperature, and density. As in Phase I, there is a tendency for the ice strength to decrease with increasing

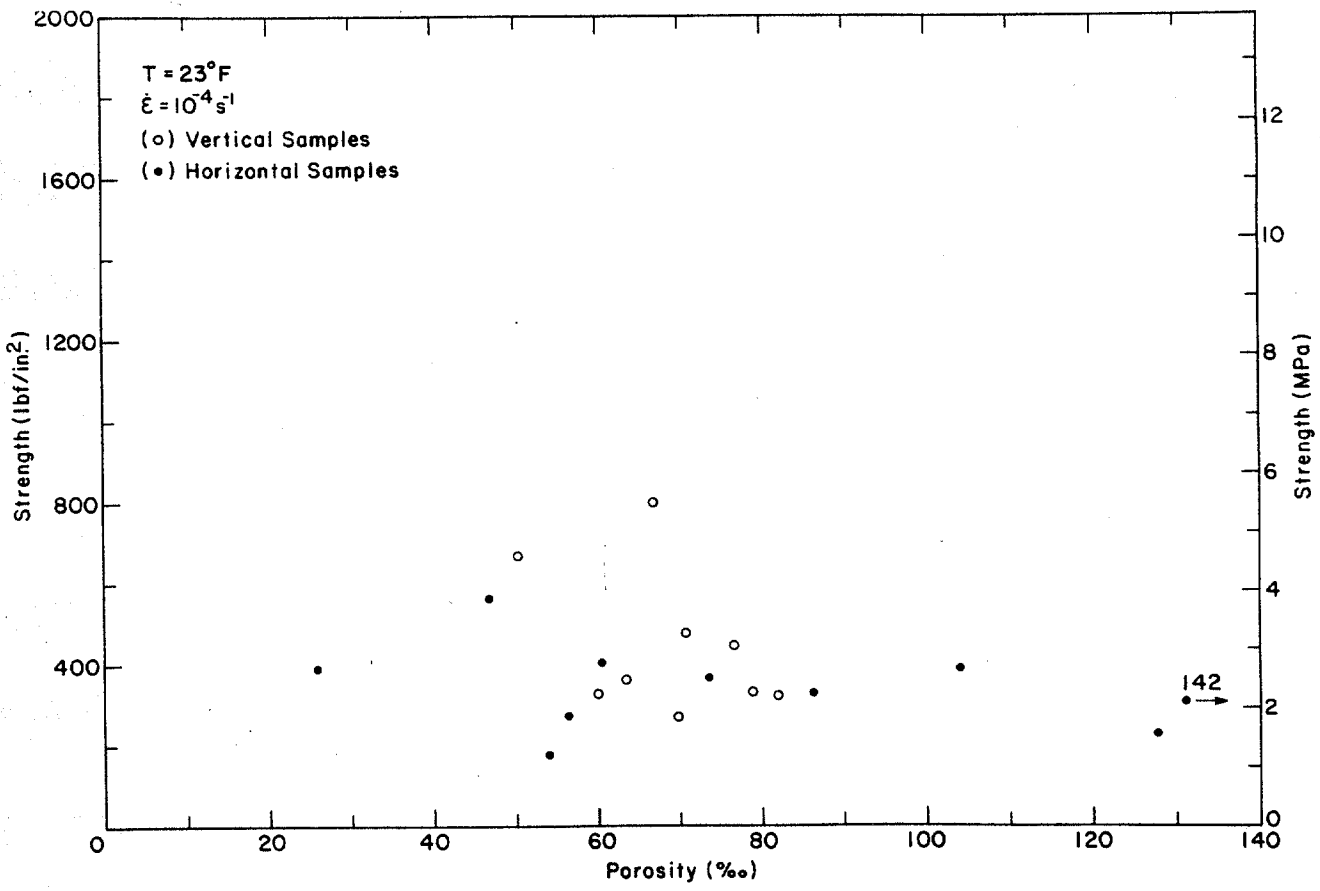

Figure 21: Uniaxial compressive strength versus porosity for horizontal and vertical samples tested at -5°C (23°F) and 10^{-4} S^{-1}.

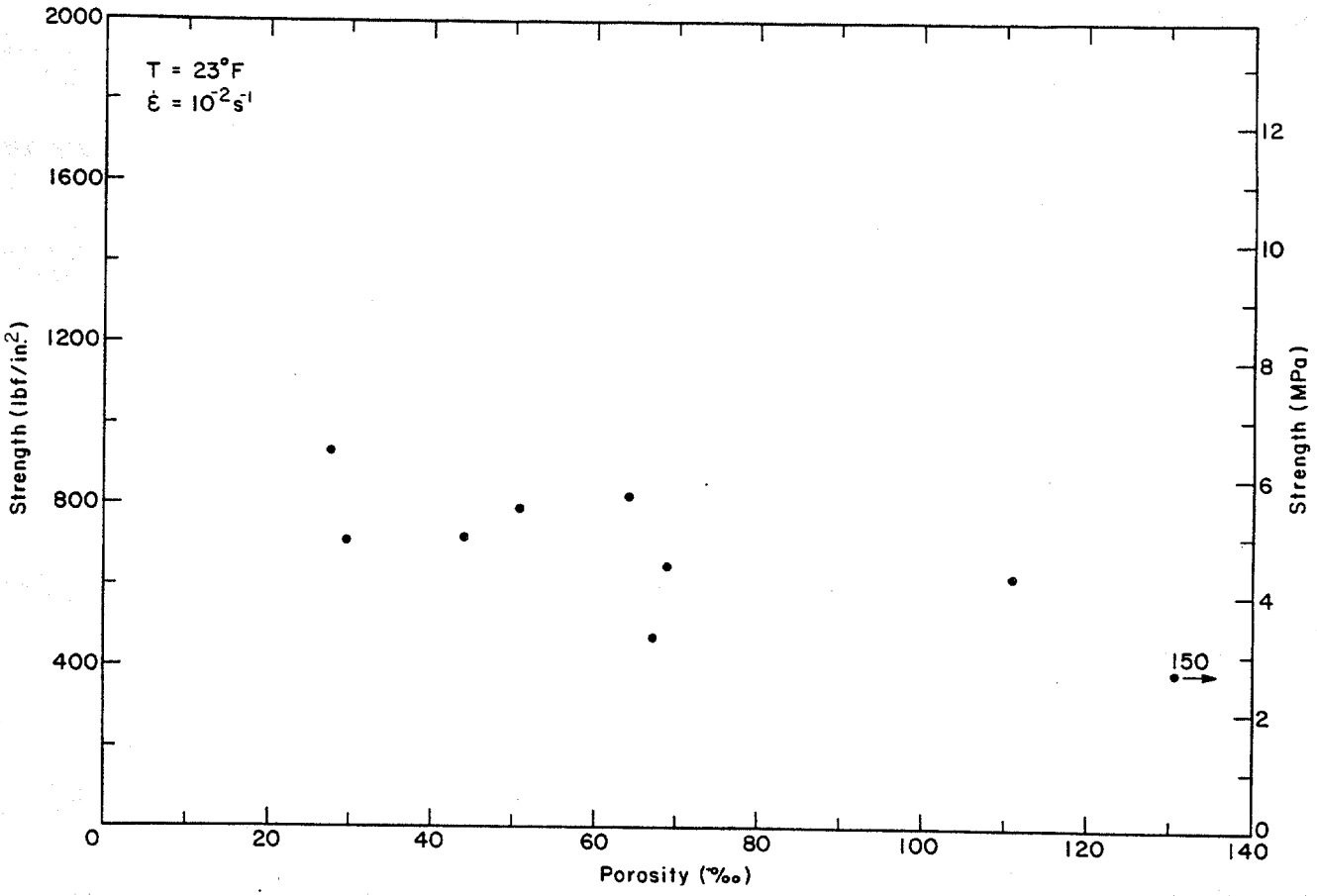

Figure 22: Uniaxial compressive strength versus porosity for tests conducted at -5°C (23°F) and 10^{-2} S^{-1}.

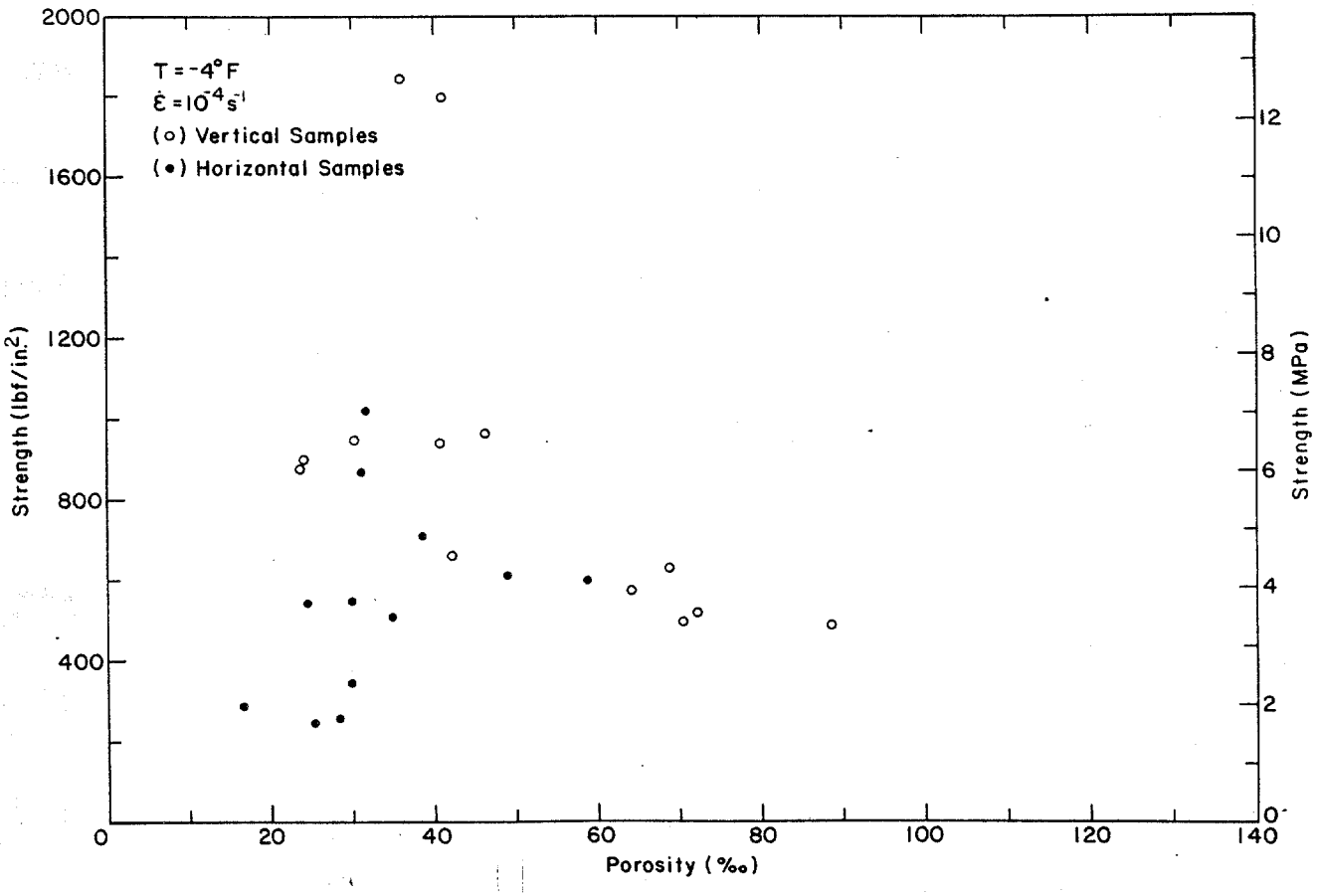

Figure 23: Uniaxial compressive strength versus porosity for horizontal and vertical samples tested at -20°C (-4°F) and 10^{-4} S^{-1}.

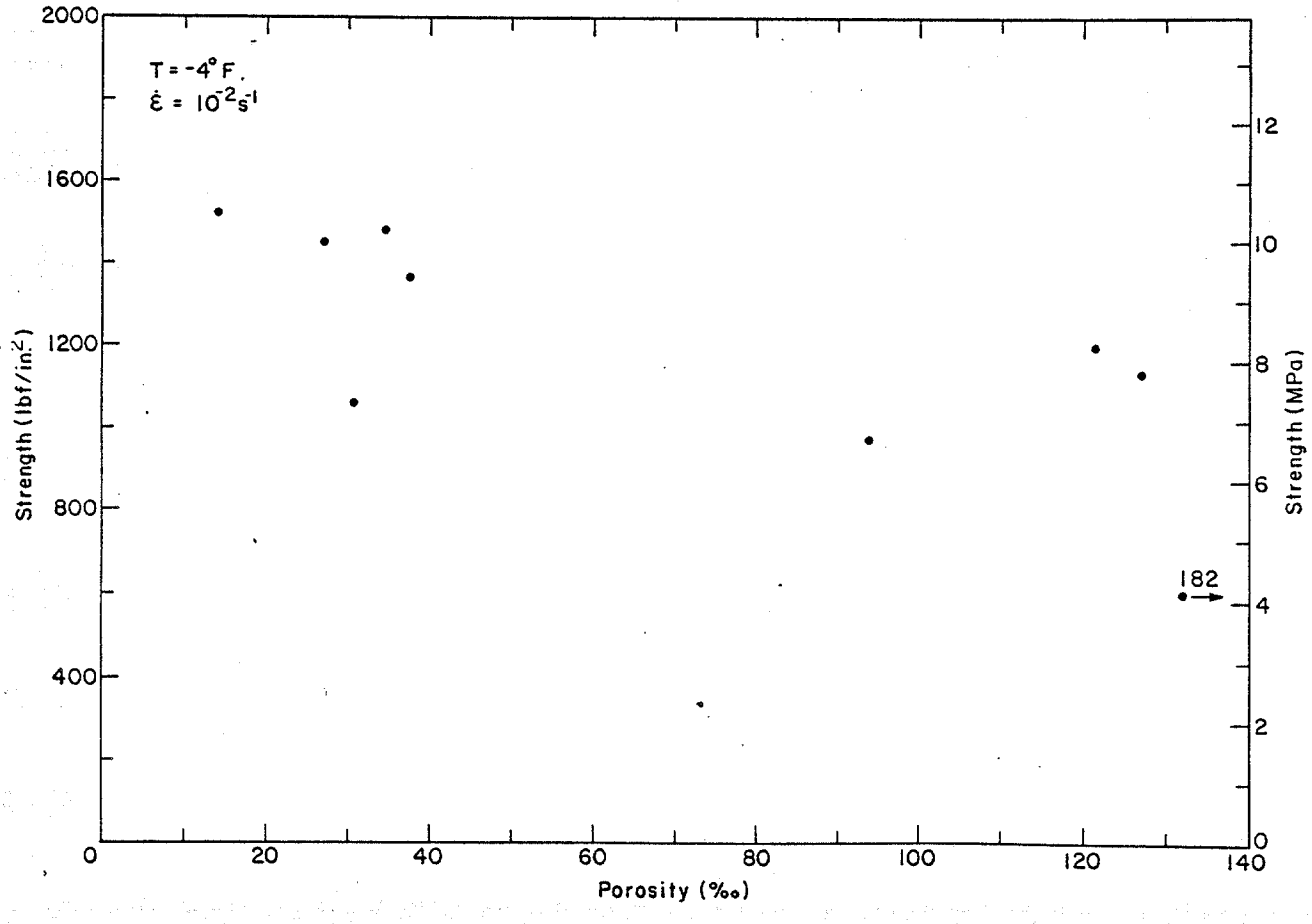

Figure 24: Uniaxial compressive strength versus porosity for tests conducted at -20°C (-4°F) and 10^{-2} S^{-1}.

porosity. This trend is again most pronounced at high strain-rates, 10^{-2} s^{-1}, where flaws and cavities play a more important role in brittle ice behavior.

Residual Compressive Strength

The uniaxial compression tests on the testing machine were programmed to continue to 5% full sample axial strain to examine the residual strength and post-yield behavior of the ice. The residual strength is defined as the stress on the sample at 5% strain assuming a constant 10.16 cm (4.000 in.) diameter specimen. Average values of the residual/maximum strength ratio of the ice samples under different loading conditions are given in Table 9. Data from Phase I are included for comparison. The results show that the residual strength/maximum strength ratio decreases with increasing strain-rate and is relatively insensitive to the ice temperature and porosity. As the strain-rate increases, fewer samples go to 5% strain and at 10^{-2} s^{-1} all the tests terminated at the peak or maximum stress.

Failure Strain

Average sample failure strain at the peak or maximum stress for the different test conditions in Phases I and II are given in Table 10. The strains were calculated from the average of the DCDT measurements on the sample. In general, there is a strong tendency for the sample failure strain to decrease with increasing strain-rate. At low strain rates of 10^{-5} and 10^{-4} s^{-1}, the failure strain also decreases as the ice gets colder. However, at high strain-rates of 10^{-3} and 10^{-2} s^{-1}, the failure strain increases the the ice gets colder. Examination of the standard

Table 9. Summary of residual/maximum compressive strength ratio data for Phases I and II.

Residual/Maximum Strength Ratios

	Maximum	Minimum	Mean	Samples	Percent to 5% strain
-5°C (23°F)					
10^{-5} s^{-1} V	1.000	0.173	0.688±0.166	68	96
10^{-4} s^{-1} V	0.591	0.244	0.396±0.096	9	100
10^{-4} s^{-1} H	0.794	0.245	0.439±0.159	10	100
10^{-4} s^{-1} all	0.794	0.244	0.418±0.131	19	100
10^{-3} s^{-1} V	0.421	0.074	0.198±0.078	43	62
10^{-2} s^{-1} V	-	-	-	-	0
-20°C (-4°F)					
10^{-5} s^{-1} V	0.970	0.315	0.642±0.162	36	88
10^{-4} s^{-1} V	0.504	0.253	0.342±0.077	9	69
10^{-4} s^{-1} H	0.675	0.202	0.405±0.137	12	100
10^{-4} s^{-1} all	0.675	0.202	0.378±0.114	21	84
10^{-3} s^{-1} V	0.746	0.047	0.194±0.148	18	44
10^{-2} s^{-1} V	-	-	-	-	0

H - Horizontal V - Vertical

Table 10. Summary of compressive failure strain data for Phases I and II.

	Failure Strain (%)			
	Maximum	Minimum	Mean	Samples
-5°C (23°F)				
10^{-5} s^{-1} V	0.83	0.06	0.38±0.17	71
10^{-4} s^{-1} V	0.62	0.09	0.18±0.17	9
10^{-4} s^{-1} H	0.26	0.06	0.12±0.07	10
10^{-4} s^{-1} all	0.62	0.06	0.14±0.12	19
10^{-3} s^{-1} V	0.20	0.05	0.13±0.03	69
10^{-2} s^{-1} V	0.10	0.02	0.07±0.02	9
-20°C (-4°F)				
10^{-5} s^{-1} V	0.73	0.10	0.31±0.14	41
10^{-4} s^{-1} V	0.21	0.10	0.15±0.04	13
10^{-4} s^{-1} H	0.14	0.07	0.10±0.03	12
10^{-4} s^{-1} all	0.21	0.07	0.13±0.04	25
10^{-3} s^{-1} V	0.25	0.05	0.19±0.04	41
10^{-2} s^{-1} V	0.16	0.08	0.12±0.03	9

H - Horizontal V - Vertical

deviation of the mean strains indicate that the observed temperature trends are not statistically significant.

Strength versus strain to failure plots are given in Figures 25 and 26. At -5°C there is a positive correlation between the strength and failure strain for the 10^{-2} s^{-1} tests, whereas at 10^{-4} s^{-1}, there is no apparent correlation. At -20°C, both the 10^{-4} and 10^{-2} s^{-1} tests show a positive correlation between the strength and failure strain.

Initial Tangent Modulus

Estimates of the initial tangent modulus were obtained from the initial slope of the force-displacement curves using the same procedures as in Phase I. The results are plotted against strain-rate in Figures 27 and 28 and listed in Table 11. Modulus values from Phase I are included in both the figures and table for comparison. The initial tangent modulus is plotted against the ice porosity for ice temperatures of -5°C and -20°C in Figures 29 and 30, respectively.

It is interesting to note that the initial tangent modulus approaches the "dynamic" Young's modulus of the ice at a lower strain-rate in the colder -20°C tests. Furthermore, at a given strain-rate and temperature there is a tendency for the modulus to decrease with increasing porosity.

CONSTANT STRAIN-RATE UNIAXIAL TENSION TESTS

Test Variables

Thirty-six constant strain-rate uniaxial tension tests were performed on vertically oriented multi-year pressure ridge samples in Phase II. The tests were conducted at two strain-rates, 10^{-5} and 10^{-3} s^{-1}, and at two temperatures, -20°C (-4°F) and -5°C (23°F). The number of tests at each

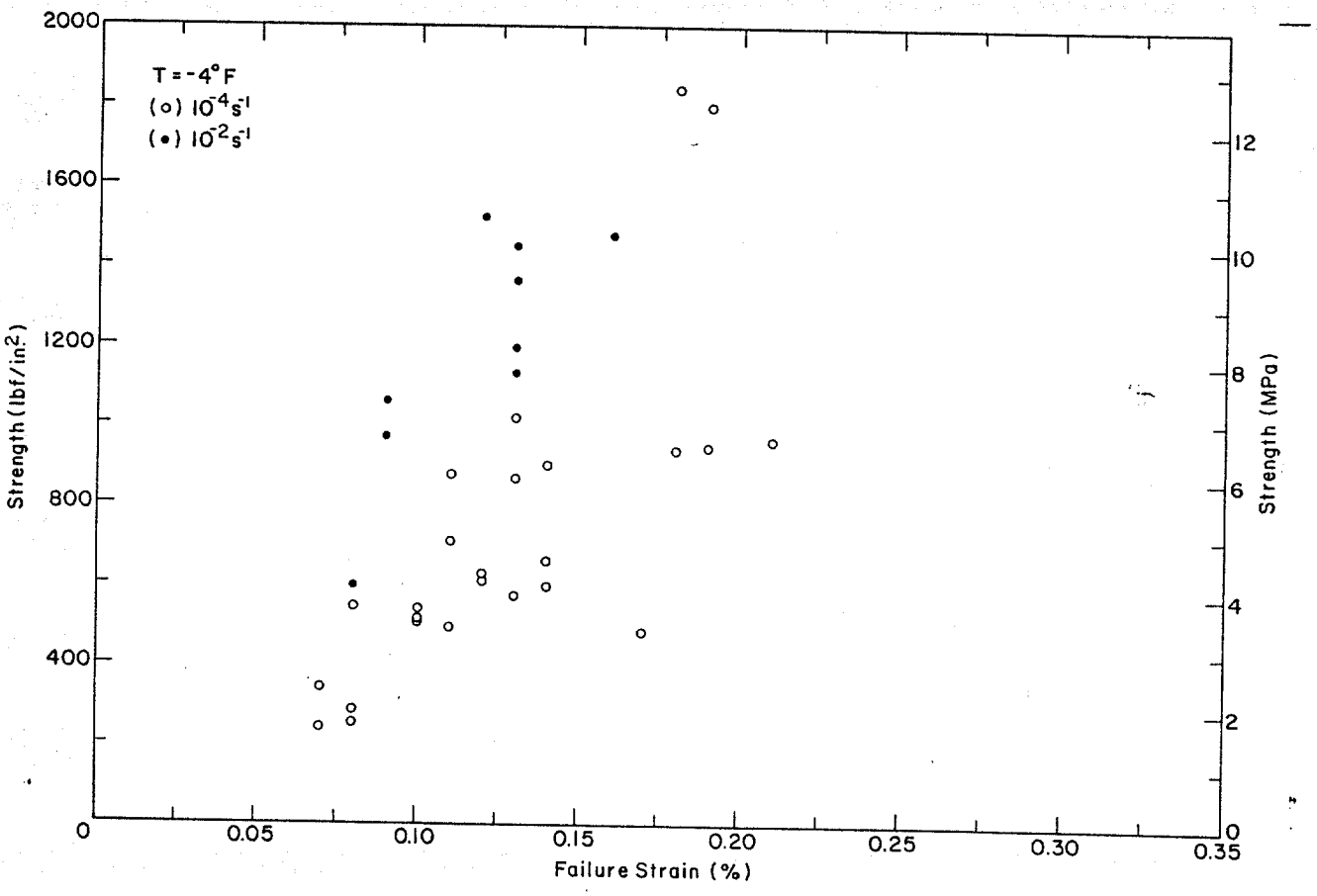

Figure 26: Uniaxial compressive strength versus failure strain for those tests conducted at -20°C (-4°F).

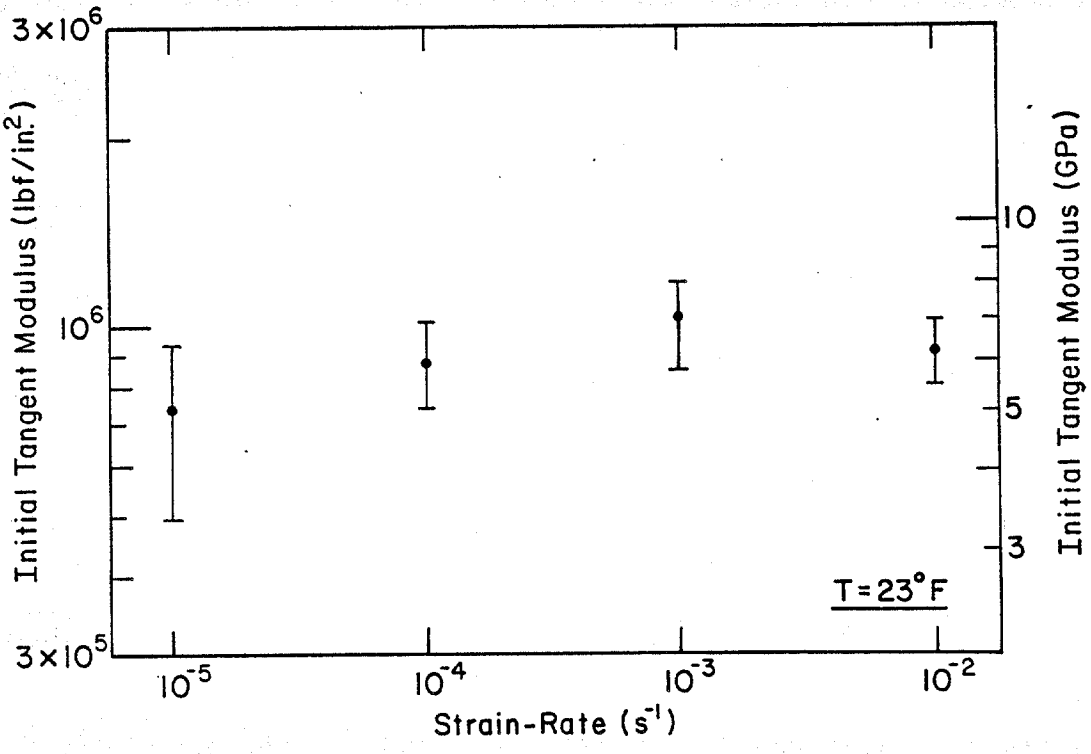

Figure 27: Initial tangent modulus in compression versus strain rate for those tests conducted at -5°C (23°F). The bars denote one standard deviation.

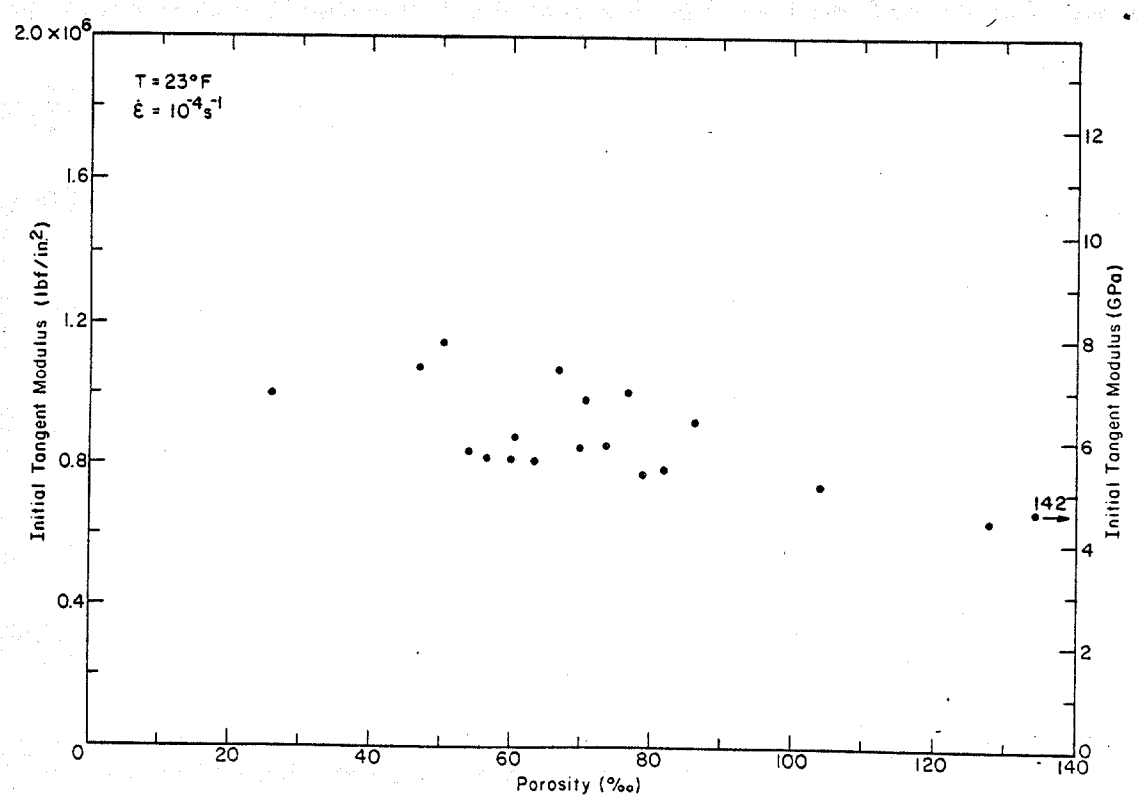

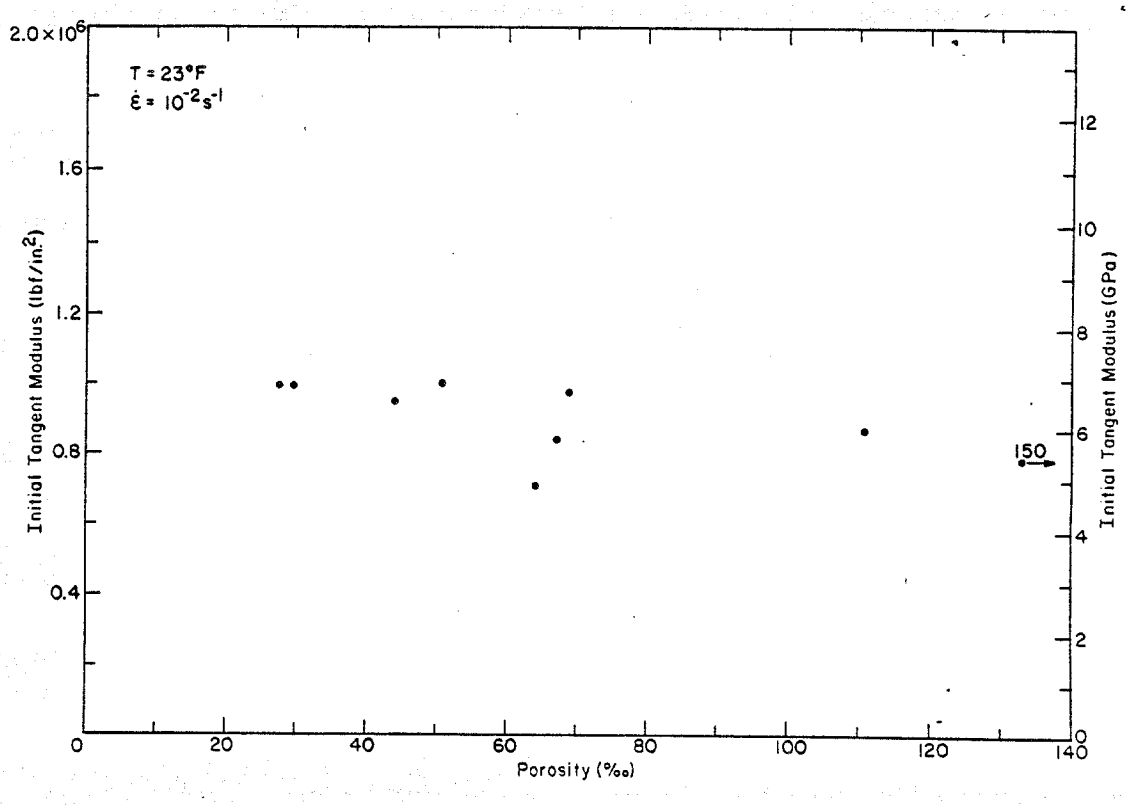

Figure 29: Initial tangent modulus in compression versus porosity for those tests conducted at -5°C (23°F).

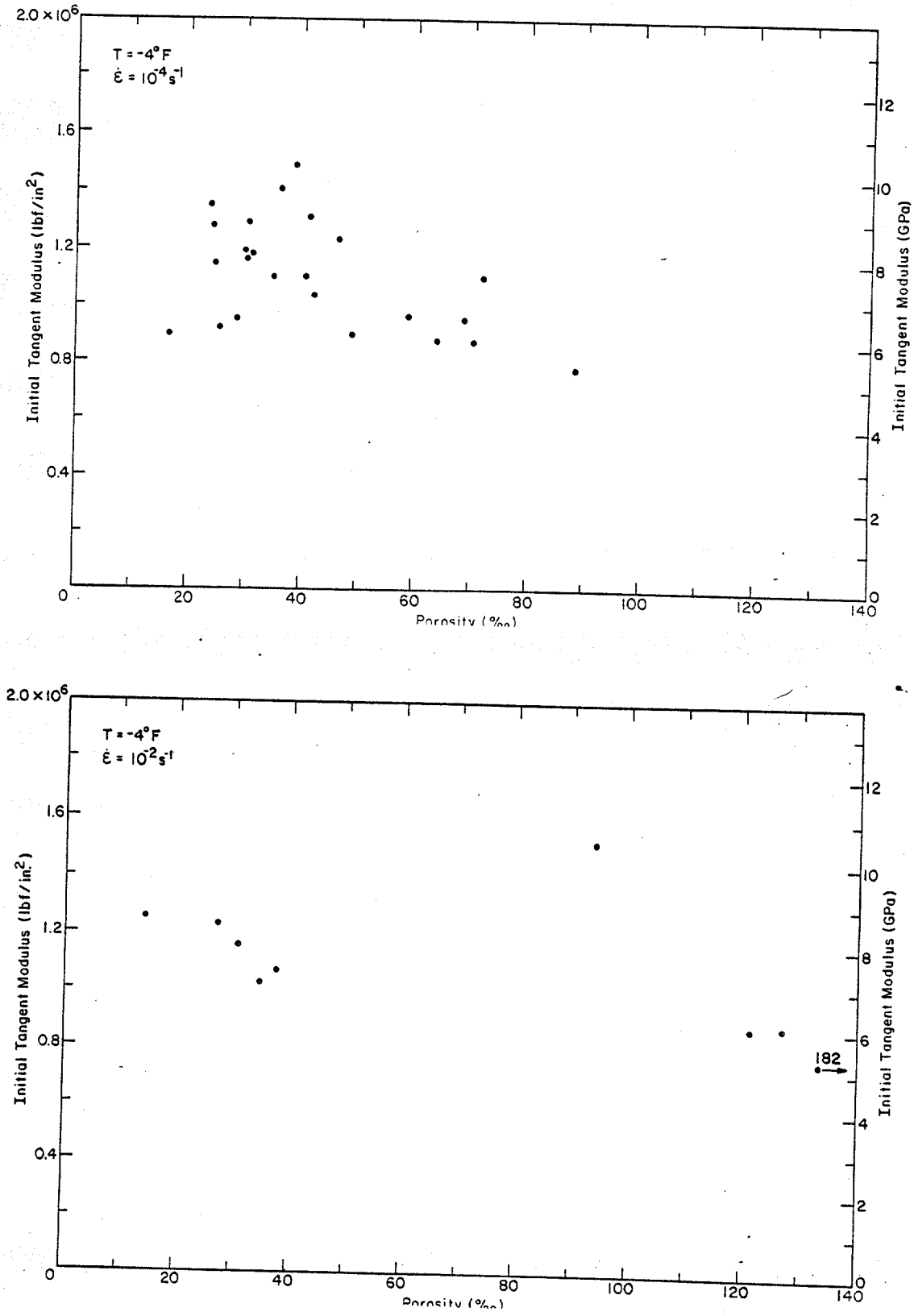

Figure 30: Initial tangent modulus in compression versus porosity for those tests conducted at -20°C (-4°F).

Table 12. Number of uniaxial tension tests at different temperatures and strain-rates.

T \ $\dot{\varepsilon}$	10^{-5} s^{-1}	10^{-3} s^{-1}	Total
-5°C (23°F)	9V	9V	18V
-20°C (-4°F)	9V	9V	18V
Total	18V	18V	36V

V - Vertical

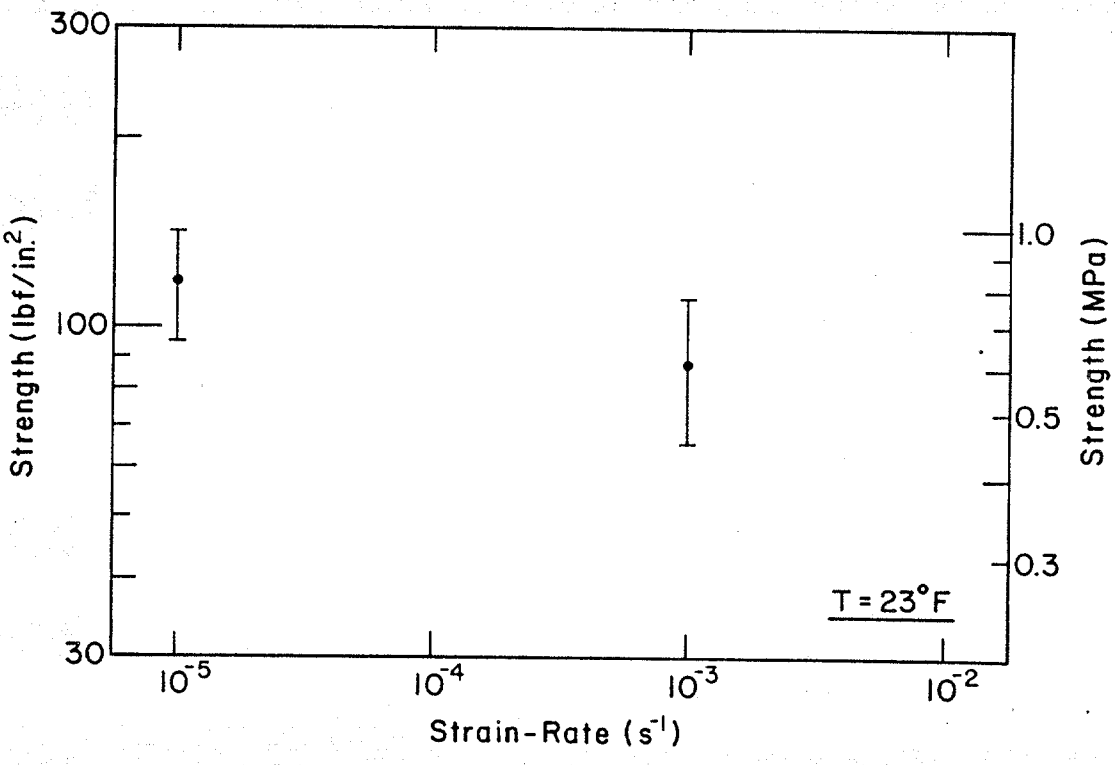

Figure 31: Uniaxial tensile strength versus strain-rate for those tests conducted at -5°C (23°F). The bars denote one standard deviation.

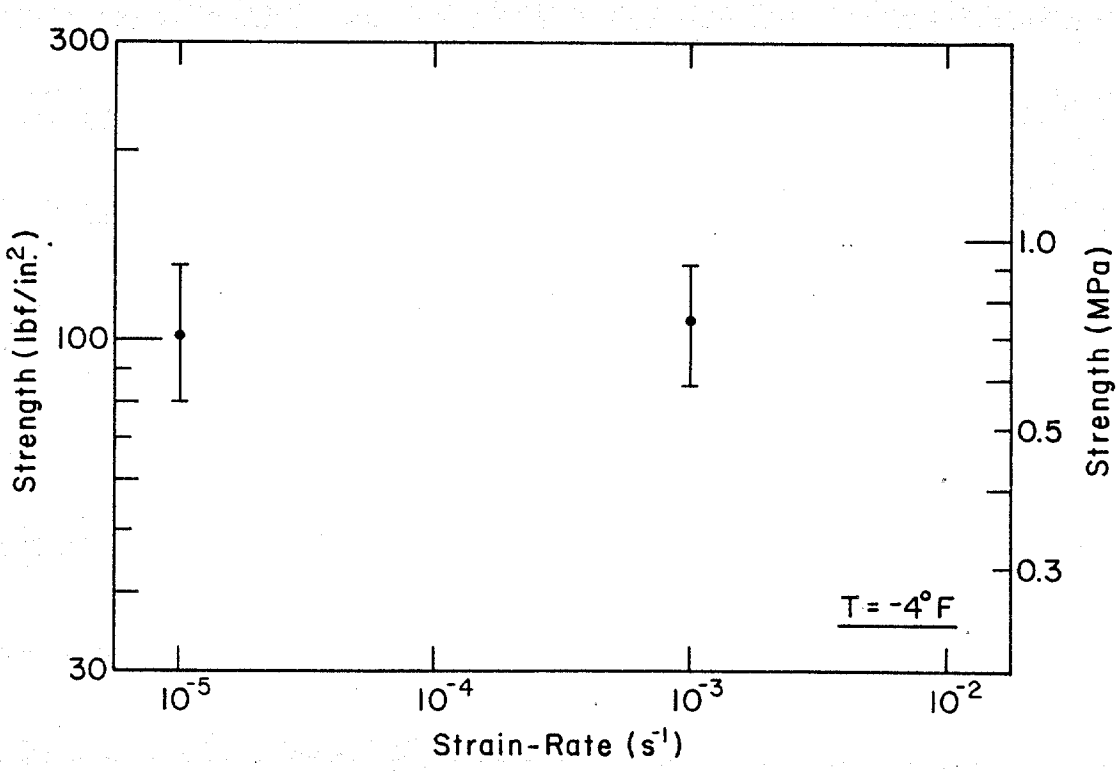

Figure 32: Uniaxial tensile strength versus strain-rate for those tests conducted at -20°C (-4°F). The bars denote one standard deviation.

Table 13. Summary of tensile strength data for Phase II.

	Uniaxial Tensile Strength							
	Maximum		Minimum		Mean		Mean Porosity	
	(MPa)	(lbf/in.^{2})	(MPa)	(lbf/in.^{2})	(MPa)	(lbf/in.^{2})	(ppt)	Samples
-5°C (23°F)								
10^{-5} s^{-1} V	1.03	149	0.57	82	0.82±0.17	119±24	78	9
10^{-3} s^{-1} V	0.83	120	0.41	60	0.61±0.16	89±23	108	9
-20°C (-4°F)								
10^{-5} s^{-1} V	0.92	134	0.49	71	0.71±0.16	103±23	82	9
10^{-3} s^{-1} V	0.92	134	0.48	69	0.75±0.16	109±23	77	9

V - Vertical

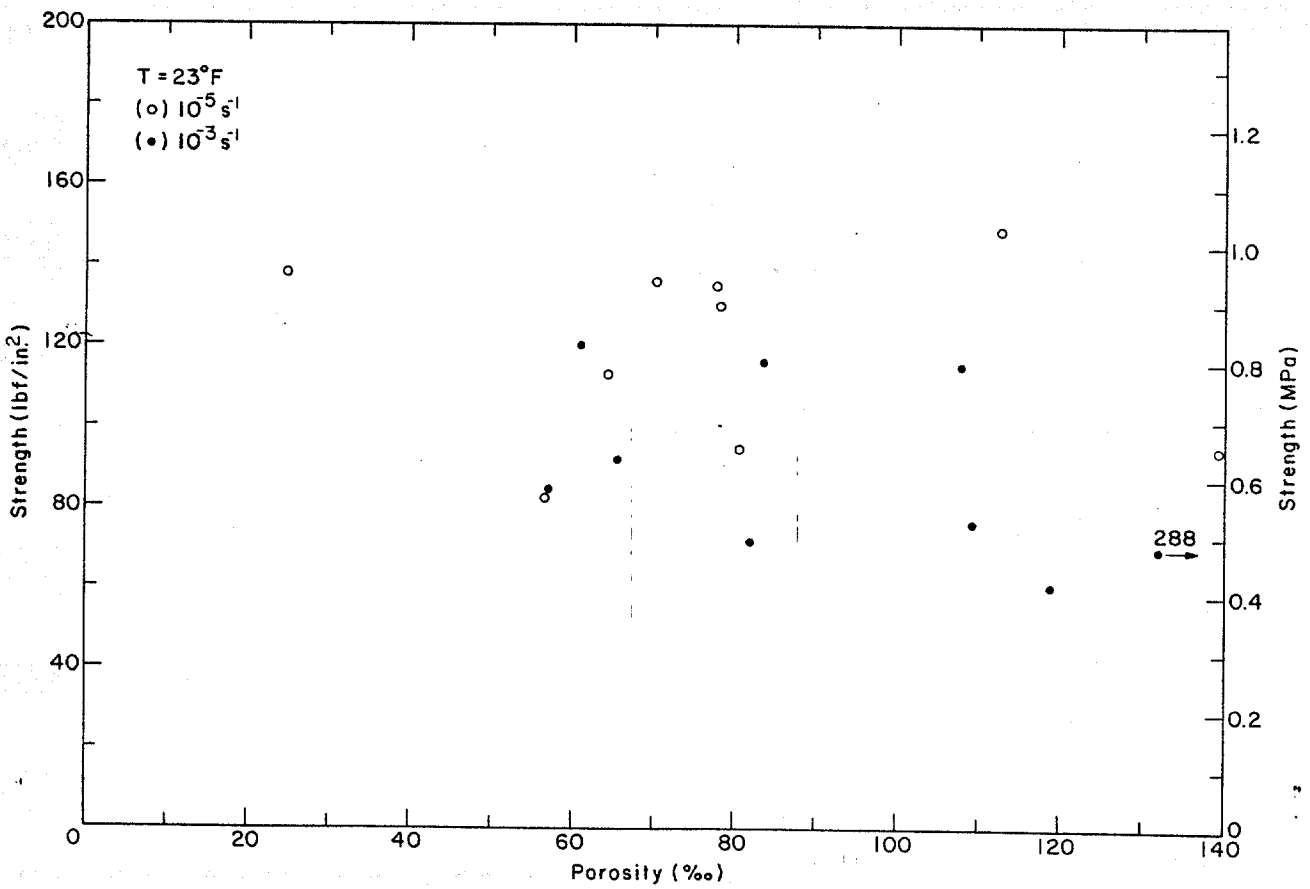

Figure 33: Uniaxial tensile strength versus ice porosity for those tests conducted at -5°C (23°F).

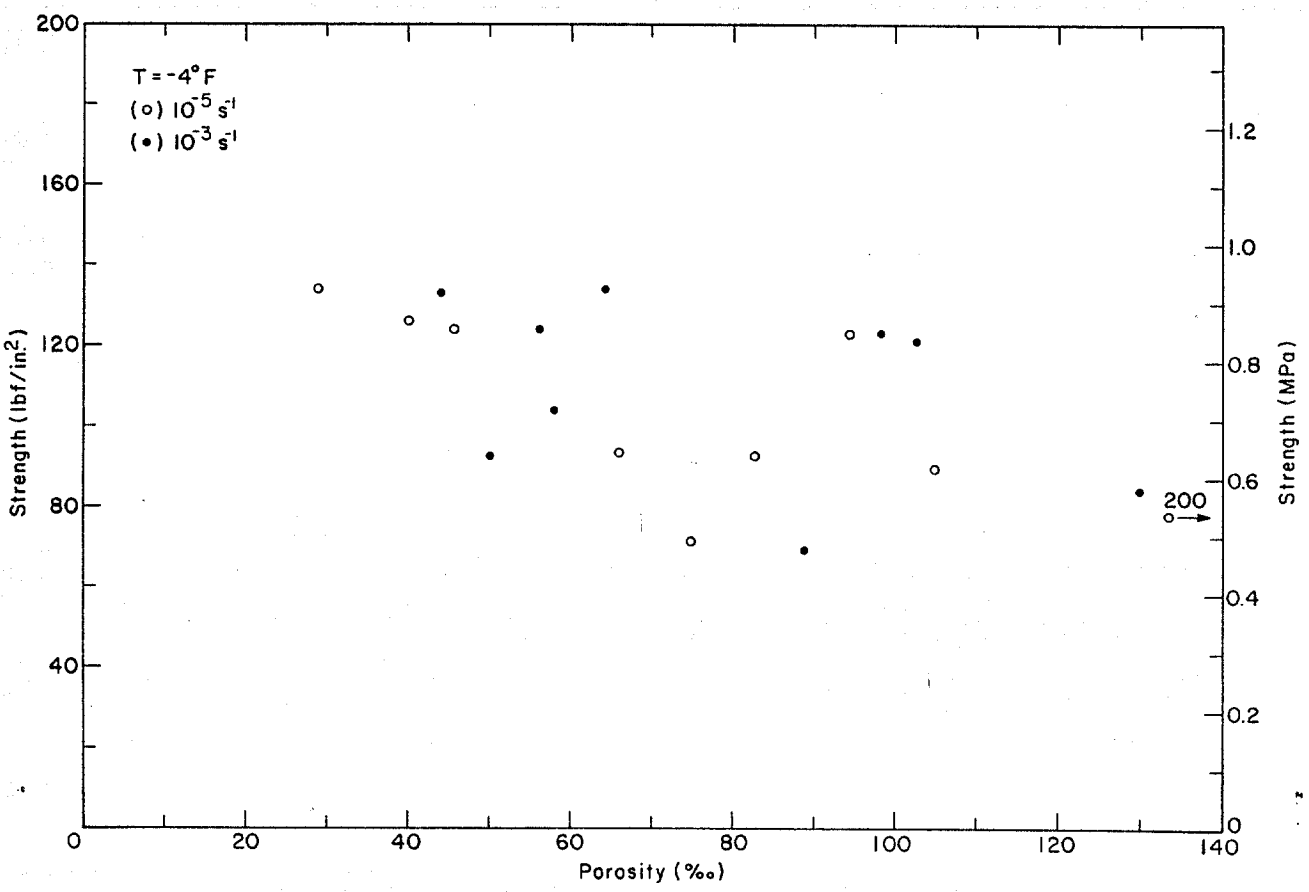

Figure 34: Uniaxial tensile strength versus ice porosity for those tests conducted at -20°C (-4°F).

Table 14. Summary of tensile failure strain data for Phase II.

	Failure Strain (%)			
	Maximum	Minimum	Mean	Samples
-5°C (23°F)				
10^{-5} s^{-1} V	0.022	0.014	0.019±0.002	9
10^{-3} s^{-1} V	0.013	0.007	0.010±0.002	9
-20°C (-4°F)				
10^{-5} s^{-1} V	0.022	0.009	0.013±0.004	9
10^{-3} s^{-1} V	0.012	0.009	0.011±0.001	9

V - Vertical

Initial Tangent Modulus

Estimates of the initial tangent modulus were obtained from the initial slope of the force-displacement curves. The results are plotted against strain-rate in Figures 35 and 36 and listed in Table 15. The modulus is also plotted against the ice porosity in Figures 37 and 38.

The initial tangent modulus show a slight increase with increasing strain-rate, and a slight decrease with increasing temperature and porosity. Relative to the compressive initial tangent modulus data, variations are small.

CONSTANT STRAIN-RATE TRIAXIAL TESTS

Equipment

Conventional triaxial tests were performed on the closed-loop testing machine using sample preparation and testing techniques similar to those employed in Phase I. As a result of our experience in Phase I, the triaxial cell was modified to increase its load bearing capacity to 350 kN (80,000 lbf) and confining pressure capacity to 24 MPa (3500 lbf/in.^{2}). Heavier latex membranes were also placed around the sample to prevent penetration of hydraulic fluid into the sample. A 22 kN (100,000 lbf) load cell was provided by Shell to measure axial forces in excess of 11 kN (50,000 lbf). The upper cylinder of the triaxial cell was also modified such that tests could be performed at confining pressure/axial stress ratios of 0.25 and 0.50.

Test Variables

A total of 55 triaxial tests were performed on multi-year pressure ridge samples at different test temperatures, nominal strain-rates, and

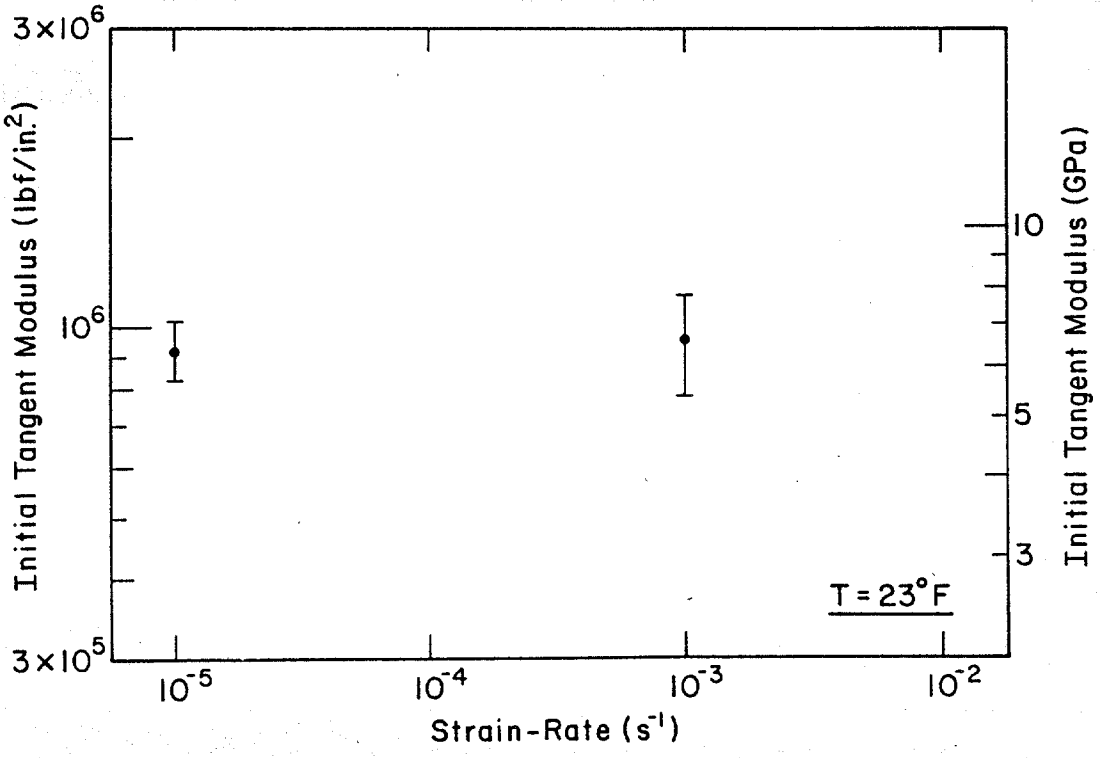

Figure 35: Initial tangent modulus in tension versus strain rate for those tests conducted at -5°C (23°F).

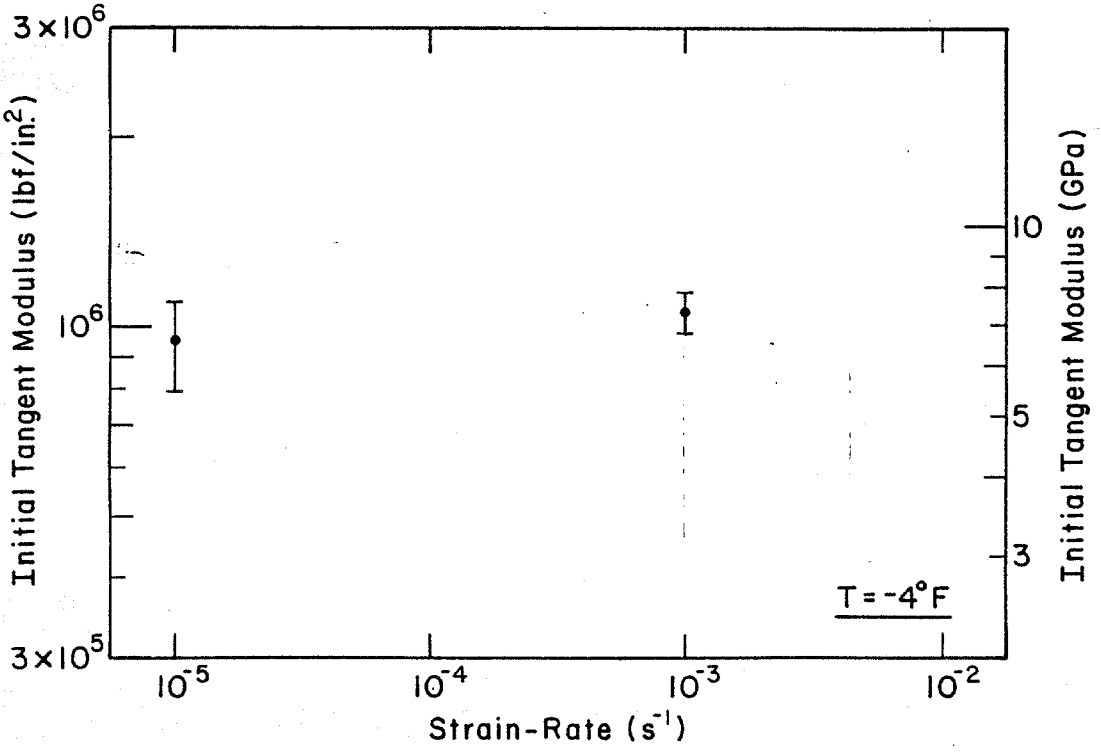

Figure 36: Initial tangent modulus in tension versus strain-rate for those tests conducted at -20°C (-4°F).

Table 15. Summary of tensile initial tangent modulus for Phase II.

	Initial Tangent Modulus							
	Maximum		Minimum		Mean		Mean Porosity	
	(GPa)	(lbf/in.^{2}x10^6)	(GPa)	(lbf/in.^{2}x10^6)	(GPa)	(lbf/in.^{2}x10^6)	(ppt)	Samples
-5°C (23°F)								
10^{-5} s^{-1} V	7.59	1.100	5.42	0.786	6.39±0.68	0.927±0.099	78	9
10^{-3} s^{-1} V	8.32	1.207	4.25	0.616	6.60±1.19	0.957±0.173	108	9
-20°C (-4°F)								
10^{-5} s^{-1} V	7.82	1.134	4.17	0.604	6.54±1.12	0.949±0.162	82	9
10^{-3} s^{-1} V	8.12	1.177	6.59	0.955	7.31±0.54	1.060±0.079	77	9

V - Vertical

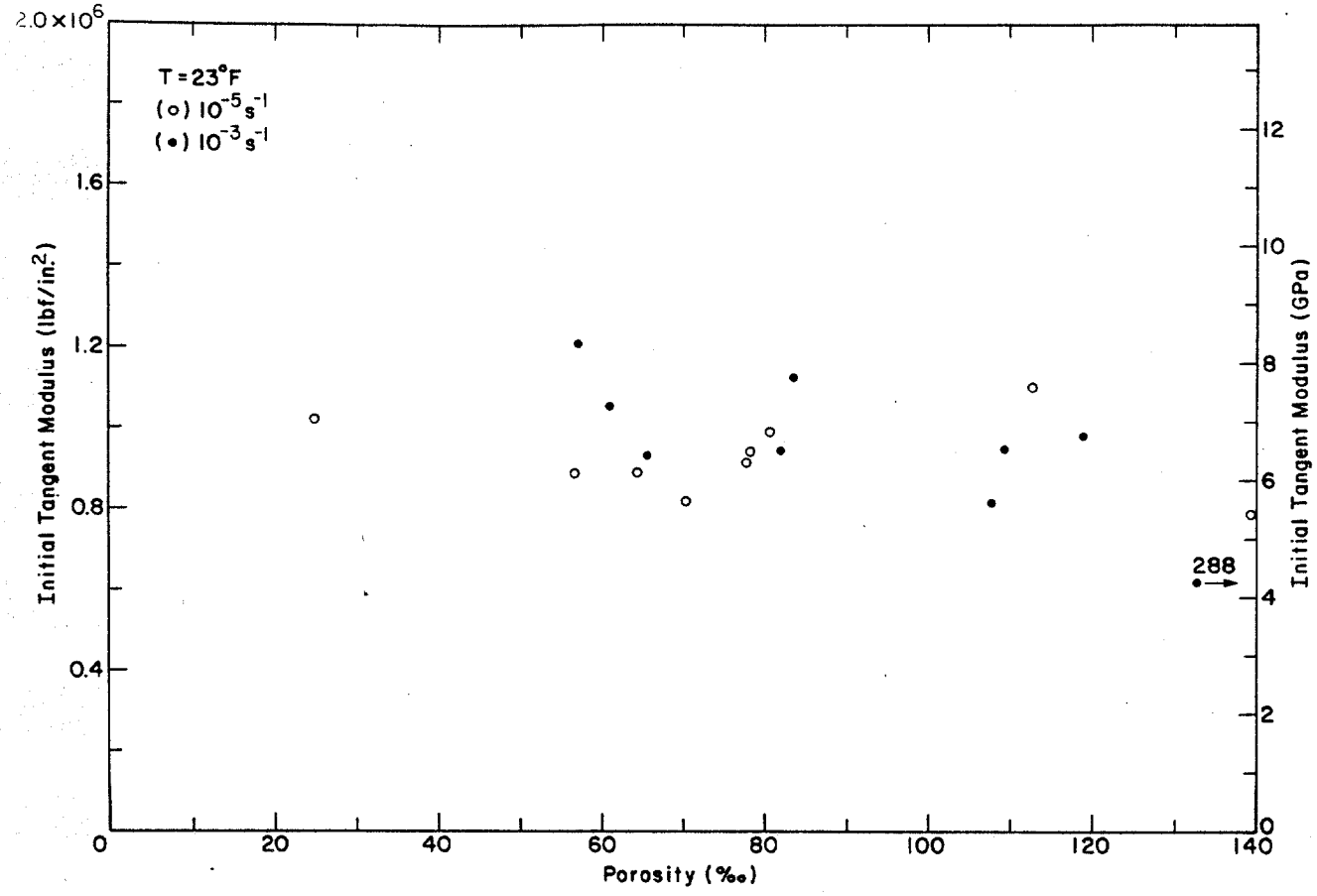

Figure 37: Initial tangent modulus in tension versus porosity for those tests conducted at -5°C (23°F).

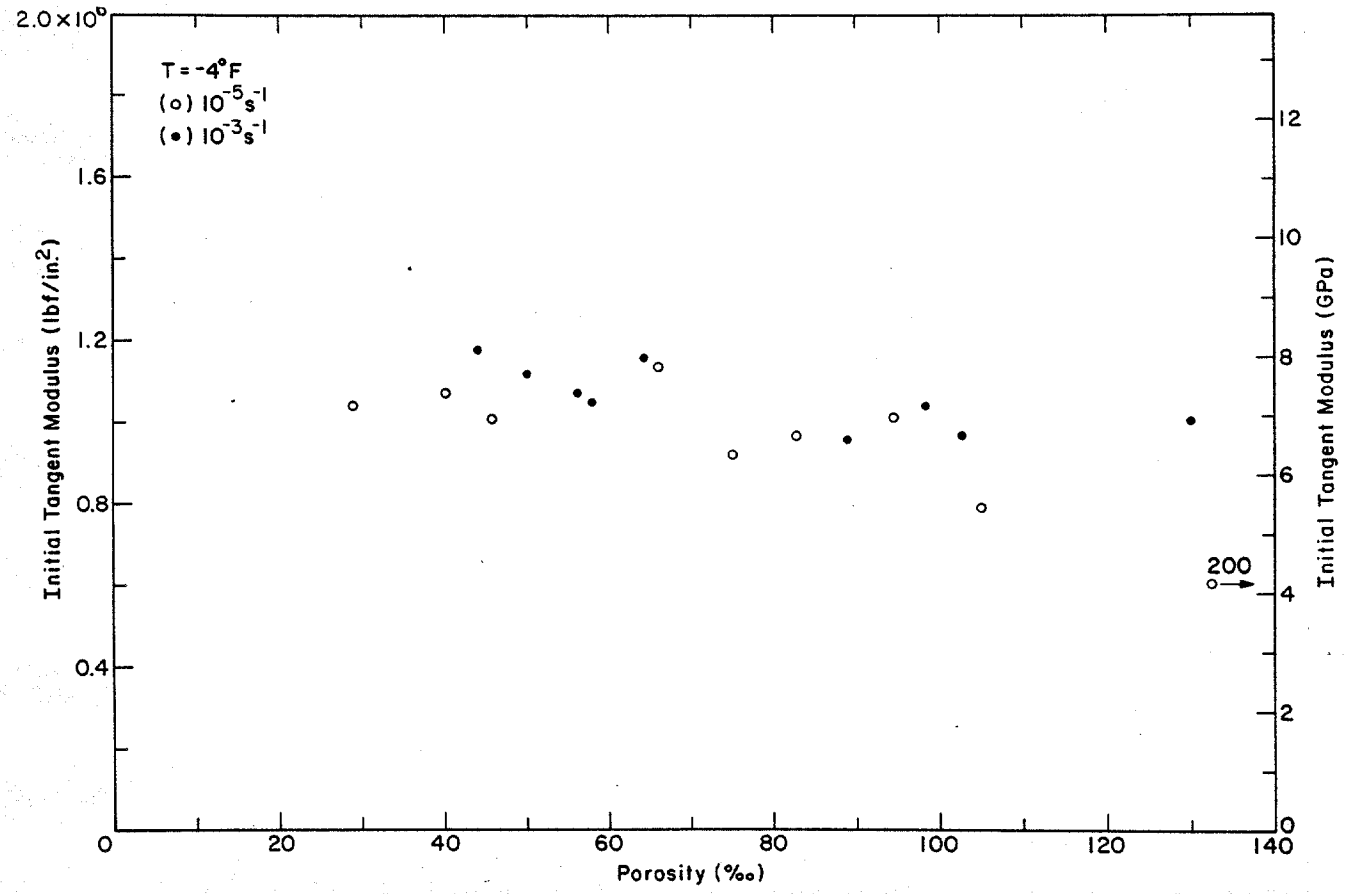

Figure 38: Initial tangent modulus in tension versus porosity for those tests conducted at -20°C (-4°F).

confining pressures. The number of tests at each test condition is summarized in Table 16. In Phase I, triaxial tests were performed on multi-year floe samples at confining pressure/axial stress ratios of 0.46 and 0.64 at the same temperatures and strain-rates.

Synthane End Caps

During the analysis of the Phase II triaxial test data it was found that the confined initial tangent modulus data of the ice were consistently lower than the initial tangent modulus data of the uniaxial or unconfined specimens. This caused some concern in that, intuitively, we would expect the confined modulus to be greater. Any confinement should reduce the axial displacement for a given load and thereby increase the measured modulus.

After checking our testing techniques and data reduction procedures, it was concluded that the lower confined modulus values were due to the use of the synthane end caps in the triaxial cell with externally mounted displacement transducers (Fig. 39). In effect, because sample displacements were measured outside the triaxial cell, the synthane end caps became a compliant element in the otherwise stiff loading system. If displacements were measured on the sample as in the uniaxial tests, the synthane end caps would not have presented any problems.

In addition to providing low confined modulus values, the synthane end caps and externally mounted displacement transducers also resulted in slightly lower ice strain-rates.

Despite the problems of using synthane end caps in the triaxial cell, it was hoped that the true ice modulus and strain-rate could be determined

Table 16. Number of triaxial tests at different temperatures, nominal strain-rates and confining pressure/axial stress ratios (σ_r/σ_a).

$\dot{\varepsilon}$ / T	σ_r/σ_a = 0.25		σ_r/σ_a = 0.50		Total
	10^{-5} s^{-1}	10^{-3} s^{-1}	10^{-5} s^{-1}	10^{-3} s^{-1}	
-5°C (23°F)	10V		9V	9V	28V
-20°C (-4°F)		9V	9V	9V	27V
Total	10V	9V	18V	18V	55V

V = Vertical

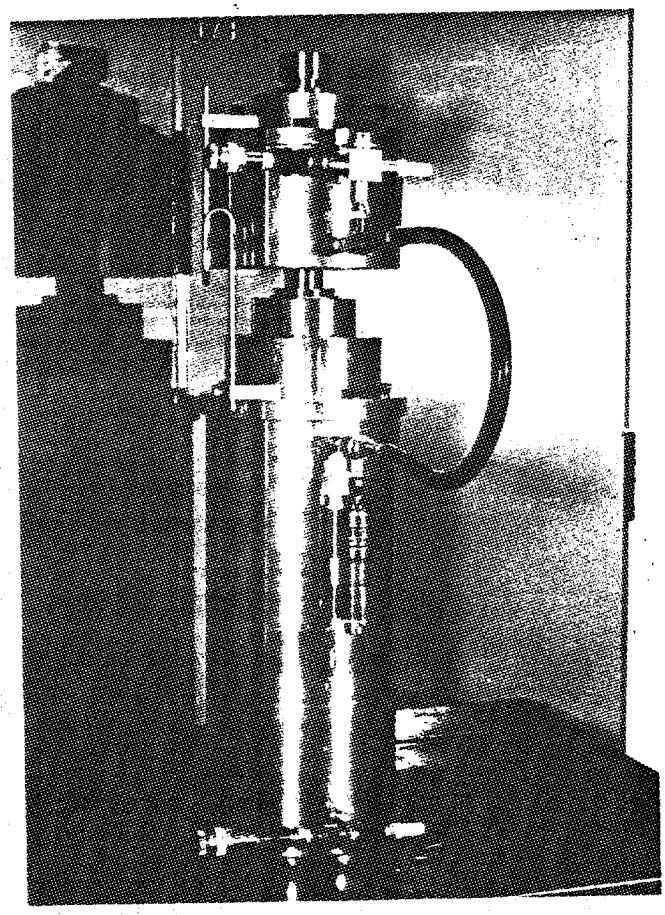

Figure 39: Triaxial cell with external mounts for extensometer.

given the mechanical properties of the synthane. Uniaxial and triaxial tests were performed on a synthane specimen to determine the synthane properties and equations were derived to calculate the actual ice modulus and strain-rate from the test results.

The uniaxial and triaxial compression tests were performed on a 4.2 in.-diam., 14-in. long synthane sample at +20 and -10°C. The tests were conducted at two strain-rates, 10^{-3} and 10^{-5} s^{-1}. Confining pressure/axial stress ratios of 0, 0.25, and 0.50 were used in the triaxial tests.

Based on our experience with the triaxial cell, means for measuring axial displacements on the triaxial cell were improved as shown in Figure 40. The test strain-rate in the new setup was controlled with the averaged output from two extensometers. The mounting positions of the extensometers were also moved from the upper cylinder to the shaft going into the triaxial cell. Previous test results indicated that the upper cylinder rotated slightly at the beginning of a test.

From the uniaxial and triaxial tests the synthane was found to have a modulus of 7.77×10^5 lbf/in.^{2} and a Poisson's ratio of 0.21. The modulus and Poisson's ratio varied little with either strain-rate or temperature. The tests also provided a measure of the loading train deflection, 1.4×10^{-7} in./lbf, which showed little variation with strain-rate, confining pressure, and temperature.

Given the synthane properties and loading train deflection, it is possible to calculate the actual test strain-rate and ice modulus. The total measured displacement, $\Delta\ell_t$, is equal to the sum of the displacements from the ice sample, $\Delta\ell_s$; the synthane end caps, $\Delta\ell_c$; and the

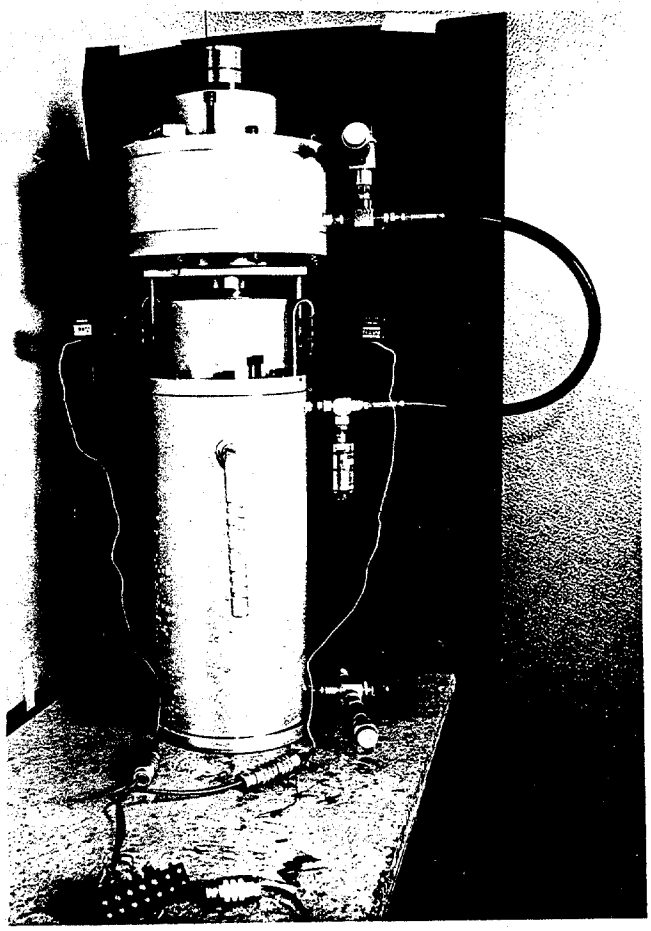

Figure 40: Triaxial cell with two external extensometers.

loading train, $\Delta\ell_\ell$:

$$\Delta\ell_t = \Delta\ell_s + \Delta\ell_c + \Delta\ell_\ell \tag{1}$$

or

$$\frac{\Delta\ell_t}{F} = \frac{\Delta\ell_s}{F} + \frac{\Delta\ell_c}{F} + \frac{\Delta\ell_\ell}{F} \tag{2}$$

where F is the applied load. From the synthane property tests, we have

$$\frac{\Delta\ell_\ell}{F} = C \tag{3}$$

where $C = 1.40 \times 10^{-7}$ in./lbf and for the two end caps

$$\frac{\Delta\ell_c}{F} = \frac{2\,\ell_c}{A_c E_c}\,(1 - 2\,\nu_c k) \tag{4}$$

where

ℓ_c = end cap thickness (2 in.)

A_c = end cap area (13.9 $in.^2$)

E_c = end cap modulus (7.77×10^5 $lbf/in.^2$)

ν_c = end cap Poisson's ratio (0.21)

k = confining pressure/axial stress ratio (0, 0.25, 0.50)

or

$$\frac{\Delta\ell_c}{F} = 3.72 \times 10^{-7}\,(1 - 0.42\,k)\ \text{in./lbf} \tag{5}$$

To put Equations (3) and (5) into perspective, a 10-in.-long, 4-in. diameter ice sample with a modulus of 7.5×10^5 $lbf/in.^2$ would deflect

$$\frac{\Delta \ell_s}{F} = 10.61 \times 10^{-7} (1-2\ \nu_s k) \text{ in./lbf}$$

Under uniaxial or low confining pressure, deformation of the load train and end caps would account for about 33% of the total displacement.

By combining Equations (1), (3) and (4) and dividing by ℓ_s, the sample length, we obtain

$$\frac{\Delta \ell_t}{\ell_s} = \frac{\Delta \ell_s}{\ell_s} + \frac{2\ \ell_c F}{\ell_s A_c E_c} (1-2\ \nu_c k) + \frac{CF}{\ell_s} \tag{6}$$

where $\Delta \ell_t / \ell_s$ is the nominal strain, ε_n, and $\Delta \ell_s / \ell_s$ is the true sample strain, ε_s. Solving for the true sample strain in terms of the nominal strain, we get

$$\varepsilon_s = \varepsilon_n - \frac{2\ell_c F}{\ell_s A_c E_c} (1-2\ \nu_c k) - C \frac{F}{\ell_s} \tag{7}$$

and by dividing by Δt

$$\dot{\varepsilon}_s = \dot{\varepsilon}_n - \frac{2\ell_c \dot{F}}{\ell_s A_c E_c} (1-2\ \nu_c k) - C \frac{\dot{F}}{\ell_s} \tag{8}$$

From Equation (7) we can also obtain a relationship between the measured (E_m) and actual (E_s) confined ice modulus by multiplying by A_s/F where A_s is the cross-sectional area of the sample:

$$\frac{\varepsilon_s A_s}{F} = \frac{\varepsilon_n A_s}{F} - \frac{A_s}{\ell_s} \left(\frac{2\ \ell_c}{A_c E_c} (1-2\ \nu_c k) + C \right) \tag{9}$$

or

$$\frac{1}{E_s} = \frac{1}{E_m} - \frac{A_s}{\ell_s} \left(\frac{2\ell_c}{A_c E_c} (1-2\ \nu_c k) + C \right) \tag{9}$$

The actual sample strain-rate during a test can be found from Equation (8) where by substitution we have

$$\dot{\varepsilon}_s = \dot{\varepsilon}_n - [3.72\text{x}10^{-8}(1-0.42\ k) + 1.4\text{x}10^{-8}]\dot{F} \qquad (10)$$

where $\dot{F}$ is the load rate in lbf/s. At the beginning of the test $\dot{F}$ is at its maximum and the actual strain-rate is at its lowest value for the entire test:

$$\dot{F} = \dot{F}_o = A_s E_m \dot{\varepsilon}_n$$

At the peak stress

$$\dot{F} = \dot{F}_p = 0$$

and

$$\dot{\varepsilon}_s = \dot{\varepsilon}_n$$

The average strain-rate up to the peak stress can be found by using

$$\dot{F}_{avg} = \frac{\sigma_m A_s}{t_m}$$

where σ_m is the peak stress and t_m is the time to failure.

The actual initial tangent modulus, E_s, can be directly determined from Equation (9). Equation (7) can be used to correct sample failure strains.

Triaxial Strength

A detailed tabulation of the measured results from the triaxial tests is given in Appendix D. The average confined compressive strength of the

ice, σ_1, for each test condition is plotted against the confining pressure ($\sigma_2=\sigma_3$) at failure in Figure 41. Average uniaxial compressive strength data from Phase I is included for comparison. In making comparisons between the unconfined and confined compressive strength data, it should be noted that the Phase I ridge samples had a much lower porosity. Table 17 summarizes the Phase II triaxial strength data.

As observed in Phase I, the confined compressive strength increases with increasing temperature, increasing strain-rate, and increasing confining pressure. Due to variability of the ice structure between samples, the data show considerable scatter. The data at 10^{-5} s^{-1} suggests that failure of the ridge ice samples at low strain-rates may be described by a Tresca or Von Mises yield criteria. The yield surface parallels the hydrostat ($\sigma_r/\sigma_a = 1$). This supports the observations made by Jones (1982) who investigated the confined compressive strength of fresh water polycrystalline ice at low strain-rates.

Failure Strains

Average failure strains at the peak or maximum stress for each confined test condition are given in Table 18. As expected, confinement reduces cracking and causes the ice to be more ductile resulting in a larger strain at failure. As the confining pressure increases, the failure strain is observed to increase in our range of test conditions.

Initial Tangent Modulus

Estimates of the initial tangent modulus were obtained from the force-displacement curves. The results are summarized in Table 19 for each test condition. As in the uniaxial compression tests the initial tangent

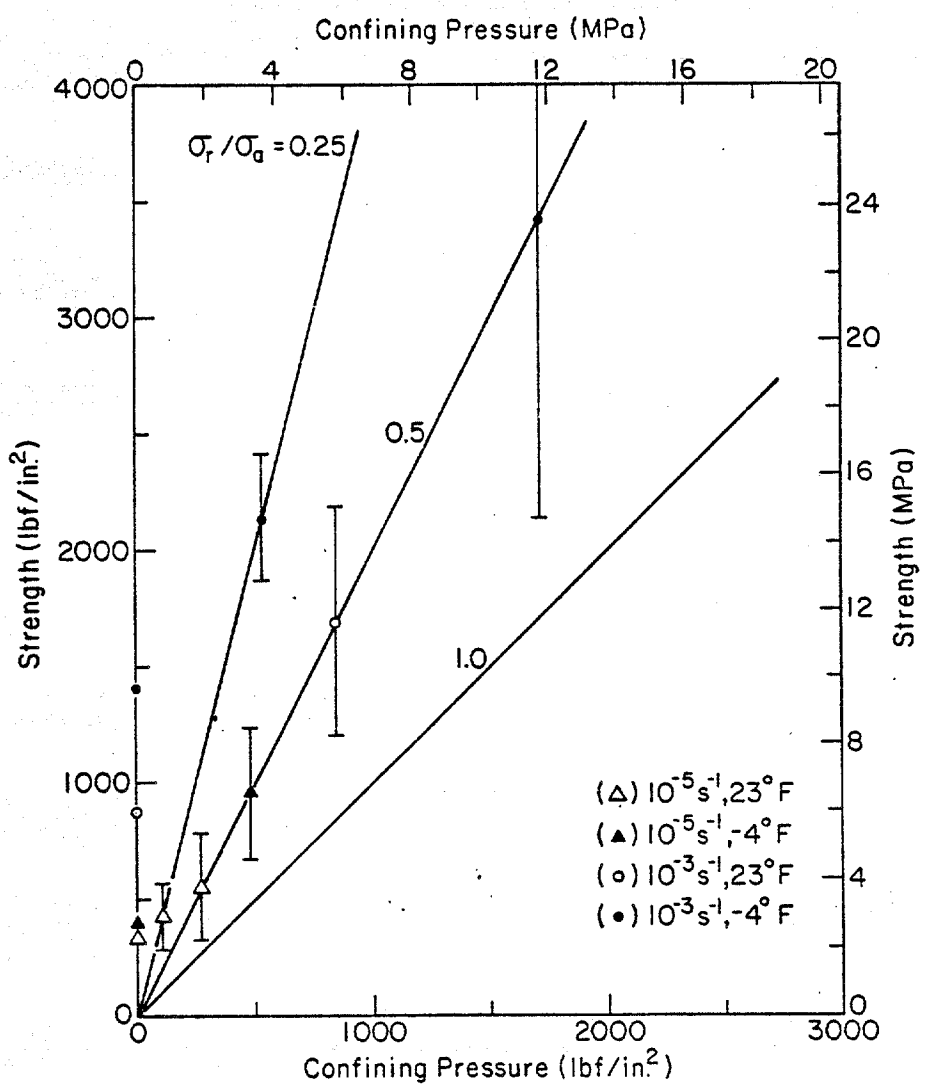

Figure 41: Compressive strength versus confining pressure for multi-year pressure ridge samples at different temperatures and nominal strain-rates. The bars denote one standard deviation from the mean.

Table 18. Summary of confined failure strain data for different nominal strain-rates, temperatures, and confining pressure/axial stress ratios. Data have been corrected for deformation of synthane end caps.

	Confined Failure Strain (%)				
	Maximum	Minimum	Mean	Mean Porosity (ppt)	Samples
-5°C (23°F)					
10^{-5} s^{-1} V, 0.25	0.97	0.35	0.70±0.25	79	10
10^{-5} s^{-1} V, 0.50	4.98	0.47	1.50±1.47	86	9
10^{-3} s^{-1} V, 0.50	0.87	0.24	0.42±0.19	78	9
-20°C (-4°F)					
10^{-3} s^{-1} V, 0.25	0.55	0.36	0.47±0.07	77	9
10^{-5} s^{-1} V, 0.50	4.97	0.59	1.86±1.79	82	9
10^{-3} s^{-1} V, 0.50	0.89	0.14	0.57±0.23	57	9

Table 19. Summary of confined initial tangent modulus data for different nominal strain-rates, temperatures, and confining pressure/axial stress ratios. Data have been corrected for deformation of synthane end caps.

	Confined Initial Tangent Modulus							
	Maximum		Minimum		Mean		Mean Porosity	
	(GPa)	(lbf/in.^{2}x10^6)	(GPa)	(lbf/in.^{2}x10^6)	(GPa)	(lbf/in.^{2}x10^6)	(ppt)	Samples
5°C (23°F)								
10^{-5} s^{-1} V, 0.25	8.41	1.219	1.38	0.200	2.78±2.24	0.403±0.325	79	9
10^{-5} s^{-1} V, 0.50	3.95	0.573	1.31	0.190	2.39±0.83	0.346±0.121	86	9
10^{-3} s^{-1} V, 0.50	8.10	1.175	3.75	0.544	5.87±1.47	0.851±0.213	78	9
-20°C (-4°F)								
10^{-3} s^{-1} V, 0.25	6.25	0.906	2.49	0.361	4.60±1.30	0.667±0.188	77	9
10^{-5} s^{-1} V, 0.50	4.48	0.649	2.30	0.334	3.09±0.81	0.448±0.117	82	9
10^{-3} s^{-1} V, 0.50	15.98	2.317	6.78	0.983	11.50±3.10	1.668±0.449	57	9

modulus is observed to increase with increasing strain-rate and decreasing temperature. Confinement also appears to increase the ice modulus; however, there are contradictory trends in the data.

Effect of Synthane End Caps on Results

The mean measured modulus, mean strength, and mean time to failure for each of the six triaxial test conditions are given in Table 20. These values were used to calculate a representative initial strain-rate, average strain-rate and corrected mean modulus for each test condition. The results are presented in Table 21.

Use of synthane end caps in the triaxial cell appears to have only a slight effect on the actual strain-rate during the test. The greatest error is introduced under test conditions where the ice is the stiffest, that is, at high pressure ($k = 0.50$), high strain-rate (10^{-3} s^{-1}), and low temperature (-20°C). Even under these conditions, the actual and nominal strain-rates only differ by 25%.

The calculated actual modulus values still appear to be too low when they are compared to the modulus values obtained from the uniaxial test specimens. This suggests that there are other displacement errors not properly accounted for, such as closure across the end cap/upper actuator interface. The Short Communication given in Appendix F demonstrates that closure errors less than 0.002 in. can significantly reduce the initial tangent modulus at the beginning of the test when displacement transducers are not placed directly on the ice.

In future triaxial tests aluminum, rather than synthane end caps will be bonded to the ice samples. The triaxial cell will also be enlarged to

Table 20. Mean measured modulus, strength, and time to failure values for each test condition.

$P/\sigma = 0.25$

	$\dot{\varepsilon}_n = 10^{-5}\ s^{-1}$	$\dot{\varepsilon}_n = 10^{-3}\ s^{-1}$
T = -5°C	$E_m = 3.02 \times 10^5$ lbf/in.^{2} $\sigma_m = 415$ lbf/in.^{2} $t_m = 720$ s	
T = -20°C		$E_m = 4.71 \times 10^5$ lbf/in.^{2} $\sigma_m = 2141$ lbf/in.^{2} $t_m = 6.00$ s

$P/\sigma = 0.50$

	$\dot{\varepsilon}_n = 10^{-5}\ s^{-1}$	$\dot{\varepsilon}_n = 10^{-3}\ s^{-1}$
T = -5°C	$E_m = 2.87 \times 10^5$ lbf/in.^{2} $\sigma_m = 552$ lbf/in.^{2} $t_m = 1540$ s	$E_m = 5.74 \times 10^5$ lbf/in.^{2} $\sigma_m = 1697$ lbf/in.^{2} $t_m = 4.97$ s
T = -20°C	$E_m = 3.56 \times 10^5$ lbf/in^2 $\sigma_m = 956$ lbf/in.^{2} $t_m = 1909$ s	$E_m = 8.57 \times 10^5$ lbf/in.^{2} $\sigma_m = 3408$ lbf/in.^{2} $t_m = 7.24$ s

Table 21. Corrected strain-rate and modulus for mean test data at each test condition.

$P/\sigma = 0.25$

	$\dot{\varepsilon}_n = 10^{-5}\ s^{-1}$	$\dot{\varepsilon}_n = 10^{-3}\ s^{-1}$
	$\dot{\varepsilon}_o = 8.21 \times 10^{-6}\ s^{-1}$	
$T = -5°C$	$\dot{\varepsilon}_{avg} = 9.66 \times 10^{-6}\ s^{-1}$	
	$E_s = 3.68 \times 10^{5}$ lbf/in.^{2}	
		$\dot{\varepsilon}_o = 7.20 \times 10^{-4}\ s^{-1}$
$T = -20°C$		$\dot{\varepsilon}_{avg} = 7.88 \times 10^{-4}\ s^{-1}$
		$E_s = 6.54 \times 10^{5}$ lbf/in.^{2}

$P/\sigma = 0.50$

	$\dot{\varepsilon}_n = 10^{-5}\ s^{-1}$	$\dot{\varepsilon}_n = 10^{-3}\ s^{-1}$
	$\dot{\varepsilon}_o = 8.44 \times 10^{-6}\ s^{-1}$	$\dot{\varepsilon}_o = 6.87 \times 10^{-4}\ s^{-1}$
$T = -5°C$	$\dot{\varepsilon}_{avg} = 9.80 \times 10^{-6}\ s^{-1}$	$\dot{\varepsilon}_{avg} = 8.14 \times 10^{-4}\ s^{-1}$
	$E_s = 3.40 \times 10^{5}$ lbf/in.^{2}	$E_s = 8.35 \times 10^{5}$ lbf/in.^{2}
	$\dot{\varepsilon}_o = 8.06 \times 10^{-6}\ s^{-1}$	$\dot{\varepsilon}_o = 5.33 \times 10^{-4}\ s^{-1}$
$T = -20°C$	$\dot{\varepsilon}_{avg} = 9.73 \times 10^{-6}\ s^{-1}$	$\dot{\varepsilon}_{avg} = 7.43 \times 10^{-4}\ s^{-1}$
	$E_s = 4.42 \times 10^{5}$ lbf/in.^{2}	$E_s = 1.61 \times 10^{6}$ lbf/in.^{2}

accommodate displacement transducers capable of withstanding hydraulic fluid and high pressures. The strain-rate will still be controlled by a pair of external extensometers, as we are interested in post-yield behaviour at large sample strains. Modulus data will be obtained from transducers on the ice.

CONSTANT LOAD COMPRESSION TESTS

Test Variables

Thirty-five constant load compression tests were performed on vertically oriented multi-year pressure ridge samples in Phase II. The tests were conducted at three loads and at two test temperatures. The number of tests at each test condition is summarized in Table 22. The small load tests at a stress of 0.69 MPa (100 lbf/in.^{2}) were performed on a specially designed pneumatic loading jig and the larger 2.07 and 4.14 MPa (300 and 600 lbf/in.^{2}) tests were conducted on the material testing machine. Sample preparation and testing techniques were identical to those used in Phase I (Mellor et al. 1984).

Test Results

A detailed tabulation of the results from the constant load compression tests is given in Appendix E. The results are summarized in Table 23 and plotted in Figures 42 through 44. The strain-rate minimum for each curve was determined by differentiating each strain time curve. The failure strain ε_f, was defined as the strain at the strain-rate minimum, marking the onset of tertiary creep.

The strain-rate minimum of each test is plotted against the applied stress in Figure 42. In general, $\dot{\varepsilon}_{min}$ increases as the applied stress

Table 22. Number of constant load compression tests performed at different loads and temperatures.

σ \ T	-5°C (23°F)	-20°C (-4°F)	Total
0.69 MPa (100 lbf/in.^{2})	9		9
2.07 MPa (300 lbf/in.^{2})	8	9	17
4.14 MPa (600 lbf/in.^{2})		9	9
Total	17	18	35

Table 23. Summary of constant load compression test data for Phase II.

Stress: 0.69 MPa (100 lbf/in.^{2}) Samples: 9
Temperature: -5°C (23°F) Porosity: 76.6±43.8°/oo

	Max	Min	Mean
$\dot{\varepsilon}_{min}$, s^{-1}	9.12×10^{-7}	1.47×10^{-8}	$1.62\times10^{-7}\pm2.85\times10^{-7}$
ε_f(FS), %	1.28	0.18	0.67 ±0.29
t_f, s	1.01×10^{5}	6.59×10^{3}	$8.05\times10^{4}\pm5.25\times10^{4}$

Stress: 2.07 MPa (300 lbf/in.^{2}) Samples: 8
Temperature: -5°C (23°F) Porosity: 53.1±19.1°/oo

	Max	Min	Mean
$\dot{\varepsilon}_{min}$, s^{-1}	1.66×10^{-4}	3.29×10^{-6}	$4.87\times10^{-5}\pm6.34\times10^{-5}$
ε_f(FS), %	0.80	0.20	0.49 ±0.20
t_f, s	1.68×10^{3}	8.29	$4.61\times10^{2}\pm5.75\times10^{2}$

Stress: 2.07 MPa (300 lbf/in.^{2}) Samples: 9
Temperature: -20°C (-4°F) Porosity: 52.1±40.2°/oo

	Max	Min	Mean
$\dot{\varepsilon}_{min}$, s^{-1}	3.03×10^{-5}	3.98×10^{-7}	$7.27\times10^{-6}\pm1.08\times10^{-5}$
ε_f(FS), %	1.03	0.07	0.46 ±0.35
t_f, s	4.79×10^{3}	7.94	$2.33\times10^{3}\pm2.05\times10^{3}$

Stress: 4.14 MPa (600 lbf/in.^{2}) Samples: 9
Temperature: -20°C (-4°F) Porosity: 60.9±40.5°/oo

	Max	Min	Mean
$\dot{\varepsilon}_{min}$, s^{-1}	1.74×10^{-4}	2.00×10^{-5}	$8.26\times10^{-5}\pm4.43\times10^{-5}$
ε_f(FS), %	0.18	0.10	0.13 ±0.03
t_f, s	1.74×10^{1}	6.75	$1.11\times10^{1}\pm3.2\times10^{0}$

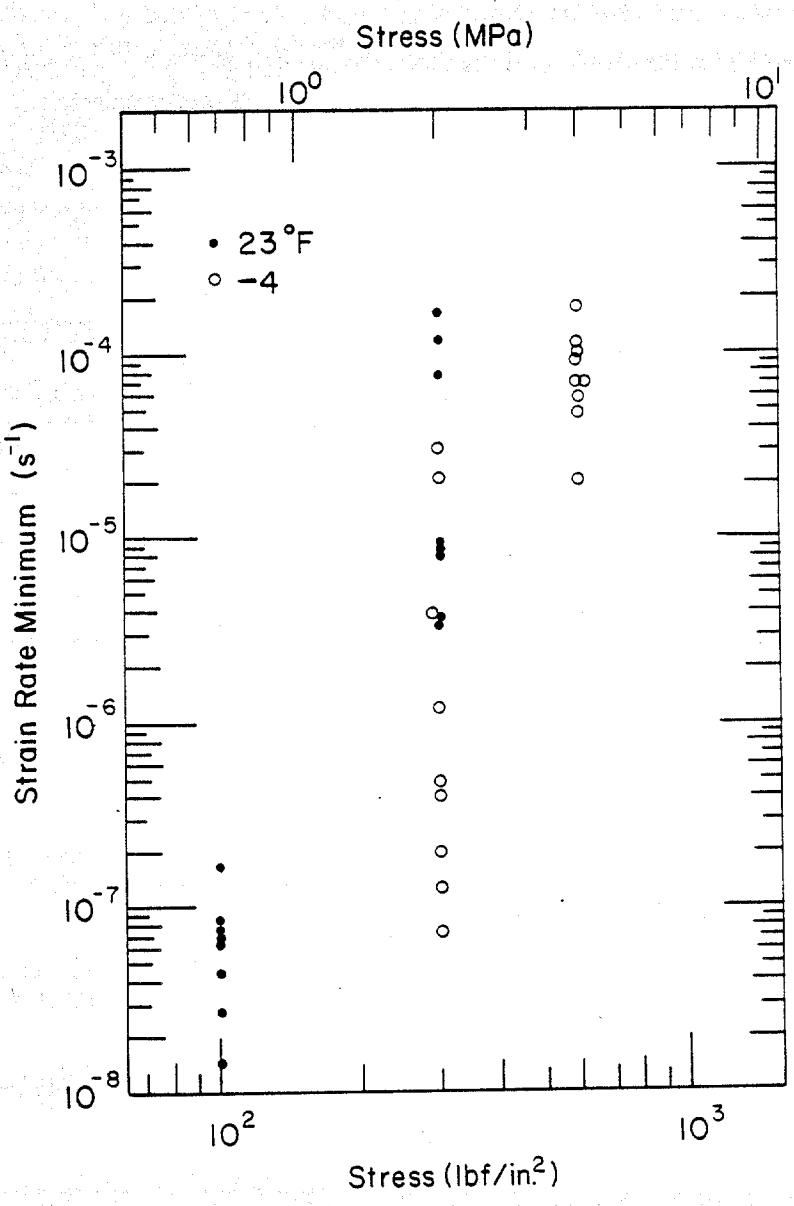

Figure 42: Strain-rate minimum versus applied stress for constant load compression test specimens at -5°C (23°F) and -20°C (-4°F).

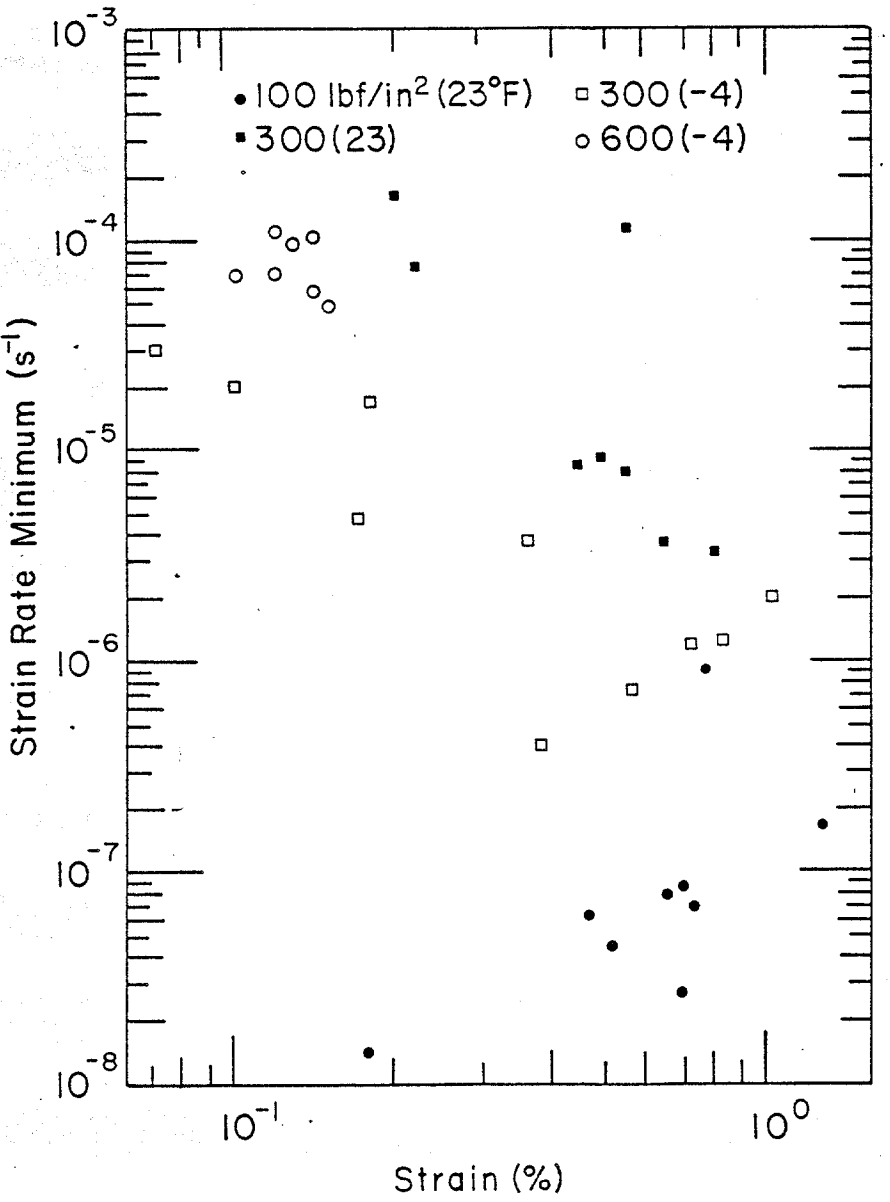

Figure 43: Strain-rate minimum versus strain at failure for constant load compression test specimens at different applied stresses and temperatures.

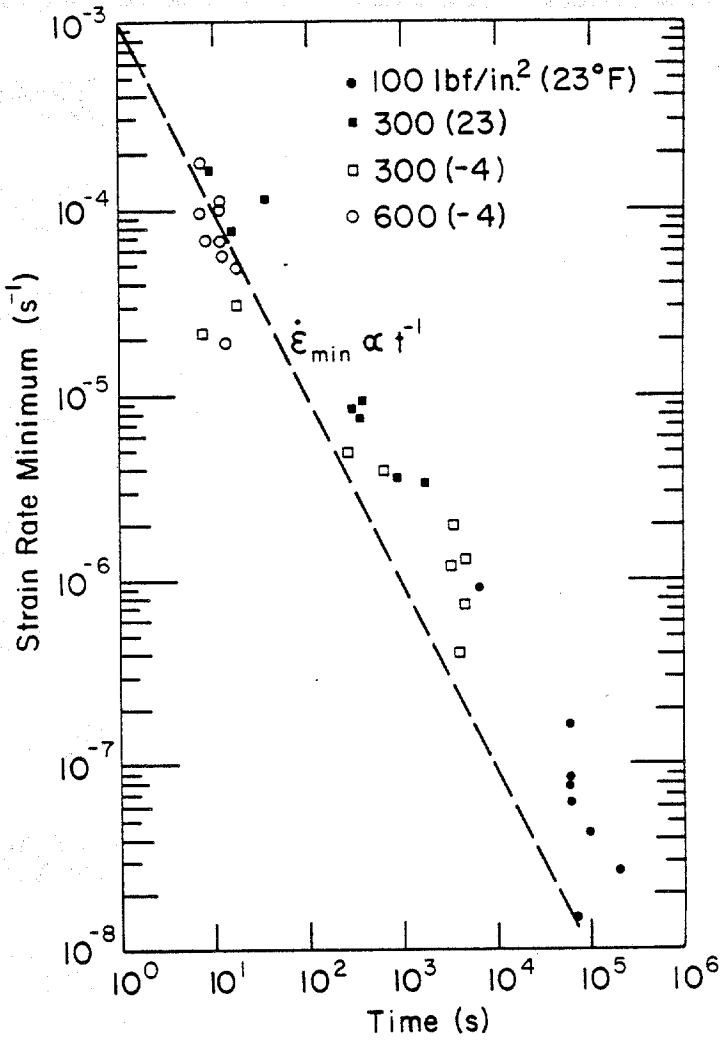

Figure 44: Strain-rate minimum versus time to failure for constant load compression test specimens at different applied stresses and temperatures.

increases and as the test temperature increases. These trends are consistent with those found in constant strain-rate tests, supporting the correspondence between these two types of tests as suggested by Mellor (1979). The large scatter in the data is attributed to the large variation in ice structure between the different samples.

The strain-rate minimum is plotted against the failure strain for each sample in Figure 43. In general, $\dot{\varepsilon}_{min}$ decreases with increasing ε_f, again supporting the correspondence between constant load and constant strain-rate tests. The strain-rate minimum is also observed to vary inversely with the time to failure as shown in Figure 44. This indicates that prior to the onset of tertiary creep, the ice can be described by a Burgers rheological model (Mellor, 1979). A Burgers model consists of a series combination of the Kelvin-Voigt and Maxwell models. It is also interesting to note that the $\dot{\varepsilon}_{min}$ decreases with decreasing temperature.

CONCLUSIONS

In Phase I a large number of uniaxial, constant strain-rate compression tests were conducted on ice samples from ten multi-year pressure ridges. These tests were performed to investigate the magnitude and variations of ice strength within and between pressure ridges. The crystallographic structure of multi-year pressure ridges was also studied for the first time. In addition, techniques and procedures were developed to perform uniaxial constant strain-rate tension tests, constant load compression tests, and conventional triaxial tests. In Phase II we used these testing techniques to provide data for developing constitutive laws and failure criteria for multi-year pressure ridges. A limited amount of

ice structure work was again performed to help us further characterize the structure of multi-year pressure ridges and explain the variation of ice strength between horizontal and vertical ice samples.

The combined test results of Phases I and II provide a foundation for developing constitutive laws and failure criteria for multi-year pressure ridges. However, before such analyses can be performed in a meaningful manner, we need to examine the ice structure of all the test specimens. Preliminary structure analyses have shown that the ice structure of multi-year pressure ridge samples is highly variable and that the structure has a profound effect on the mechanical properties of the ice. Without characterizing the structure of each specimen, we would be mixing numerous ice types in our analyses and we would have to contend with a large unexplained variance in the input data and results. Plans are therefore being made to analyze the structure of all the Phase I and Phase II samples. Ice structure classification will also become a standard procedure in future phases of the project.

It appears that, in multi-year pressure ridges containing a large proportion of columnar sheet ice blocks, the horizontal ice strength may be significantly less than the vertical ice strength. This is because there may be preference for ice blocks to lie in a near horizontal position during ridge formation. The results of this study and those of earlier investigators (Peyton, 1966) have shown that horizontal sheet ice samples are significantly weaker than vertical sheet ice samples. More field studies of the internal structure of first-year and multi-year pressure ridges are needed to capitalize on this finding. Using ice strength data

from vertically oriented ridge specimens may be conservative in horizontal ridge loading problems.

In some respects it is difficult to combine the uniaxial compression test results from Phases I and II. This is because the Phase II samples contained significantly more columnar ice and were more porous. These difficulties can be remedied by characterizing the ice structure and porosity of each sample and, in a subsequent phase of the test program, test Phase I ice under Phase II test conditions and vice versa.

Before closing, it should also be mentioned that high temperature tests are still needed to define the mechanical properties of pressure ridge keels.

REFERENCES

Cox, G.F.N. and W.F. Weeks (1983) Equations for determining the gas and brine volumes in sea ice samples. Journal of Glaciology, Vol. 29, No. 102, pp. 306-316.

Cox, G.F.N., J.A. Richter-Menge, W.F. Weeks, M. Mellor and H.W. Bosworth (1984) The mechanical properties of multi-year sea ice, Phase I: Test results. U.S. Army CRREL Report 84-9.

Jones, S.J. (1982) The confined compressive strength of polycrystalline ice. Journal of Glaciology, Vol. 28, No. 98, pp. 171-178.

Mellor, M. (1979) Mechanical properties of polycrystalline ice. In Physics and Mechanics of Ice (P. Tryde, ed.), Berlin: Springer-Verlag, pp. 217-245.

Mellor, M. (1983) Mechanical behaviour of sea ice. U.S. Army CRREL Monograph 83-1.

Mellor, M., G.F.N. Cox and H.W. Bosworth (1984) The mechanical properties of multi-year sea ice: Testing techniques. U.S. Army CRREL Research Report 84-8.

Peyton, H.R. (1966) Sea ice strength. Geophysical Institute, University of Alaska, Report UAG R-182.

Rand, J.H. (In Prep) The CRREL four-inch ice coring auger. U.S. Army CRREL Report.

Richter, J.A. and Cox, G.F.N. (1984) A preliminary examination of the effect of structure on the strength of ice samples from multi-year pressure ridges. In Proceedings of the Third International Offshore Mechanics and Arctic Engineering Symposium, February 1984, New Orleans, Vol. 3, pp. 140-144.

Wang, Y.S. (1979) Crystallographic studies and strength tests of field ice in the Alaskan Beaufort Sea. In Proceedings of the Fifth International Conference on Port and Ocean Engineering under Arctic Conditions, (POAC '79), Trondheim, Norway, August 1979, Vol. 1, pp. 346-355.

APPENDIX A

ICE STRUCTURE PROFILE OF RIDGE C CORE

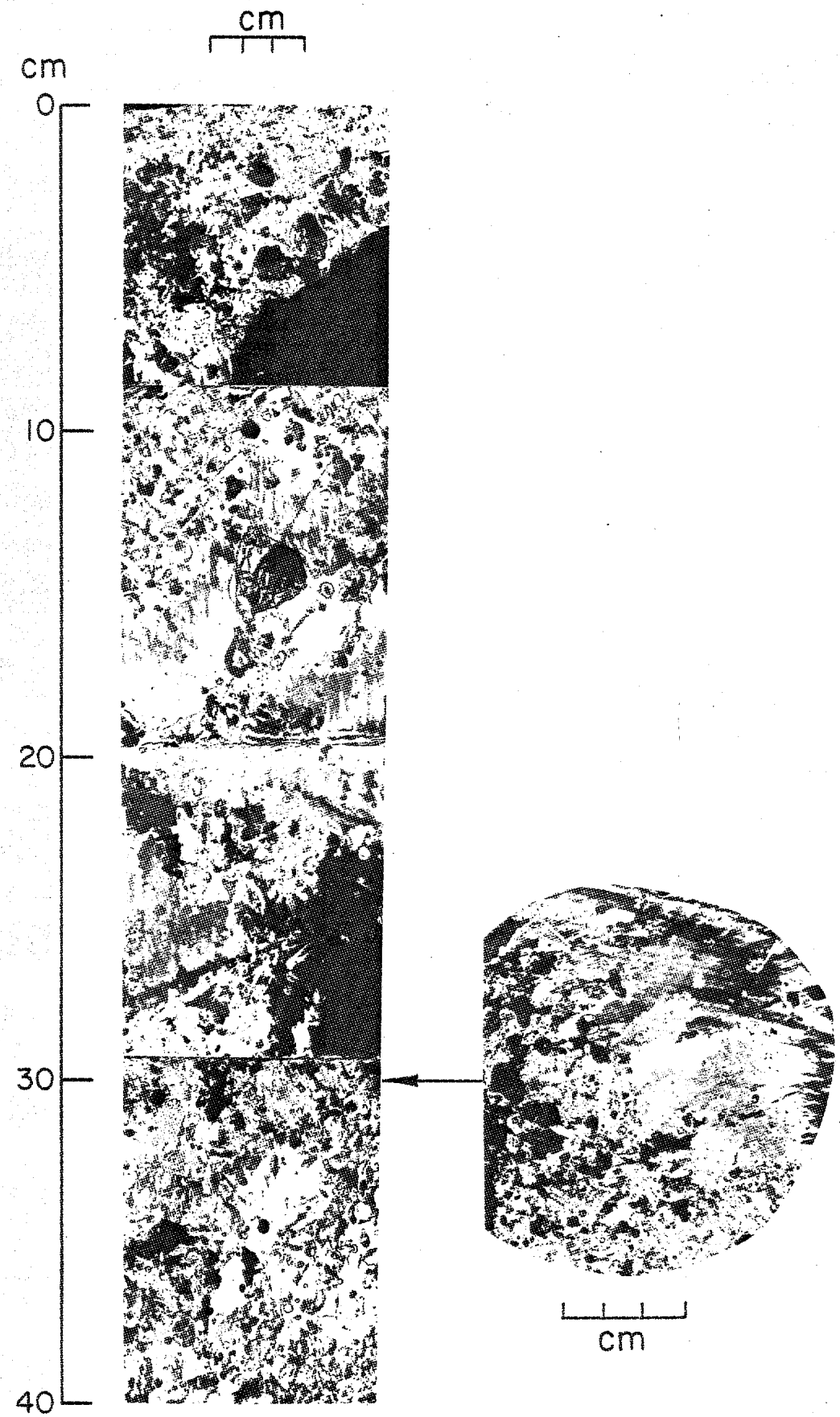
cm
cm
0
10
20
30
40
cm

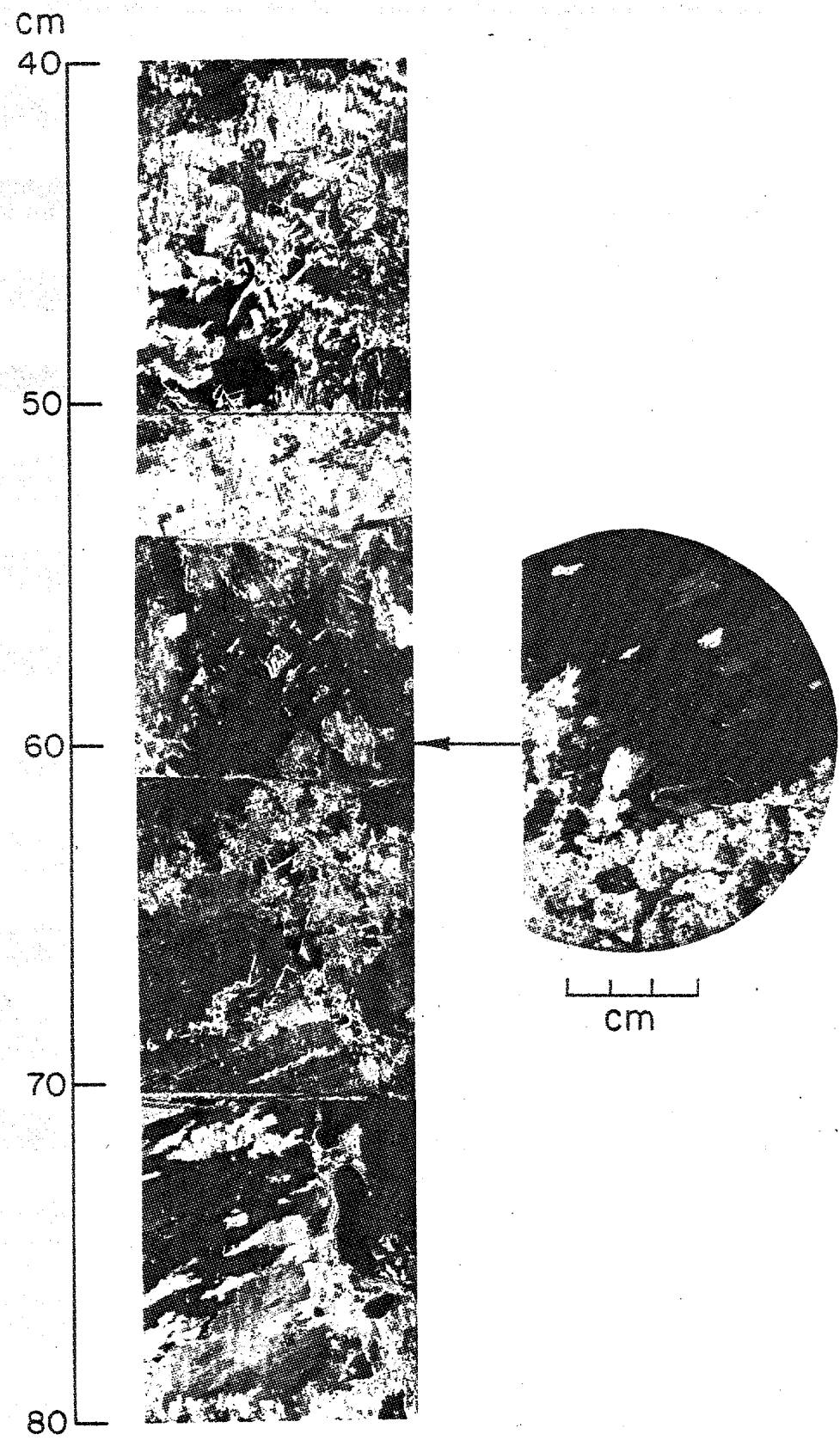
cm
40
50
60
70
80
cm

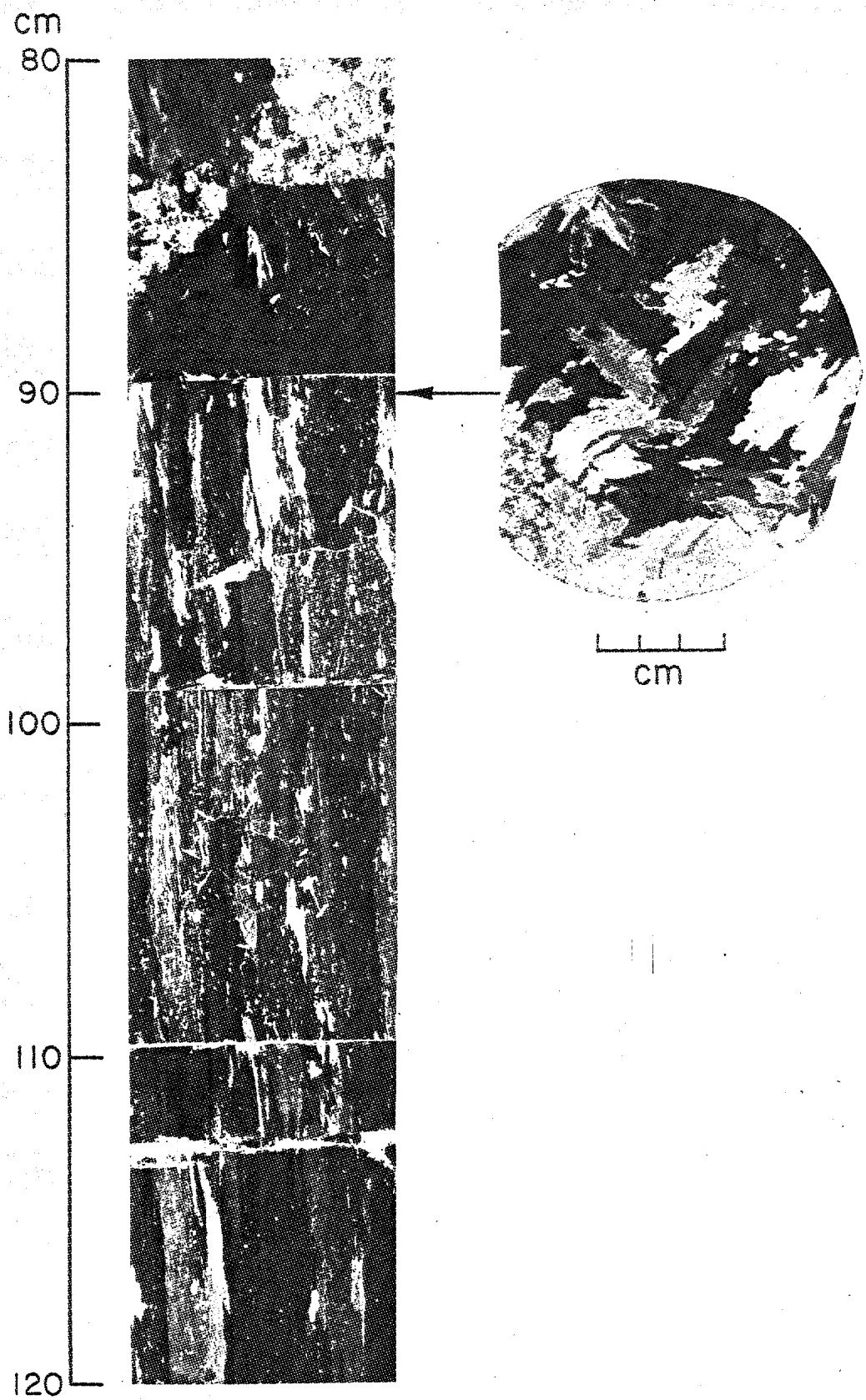
cm
80
90
100
110
120
cm

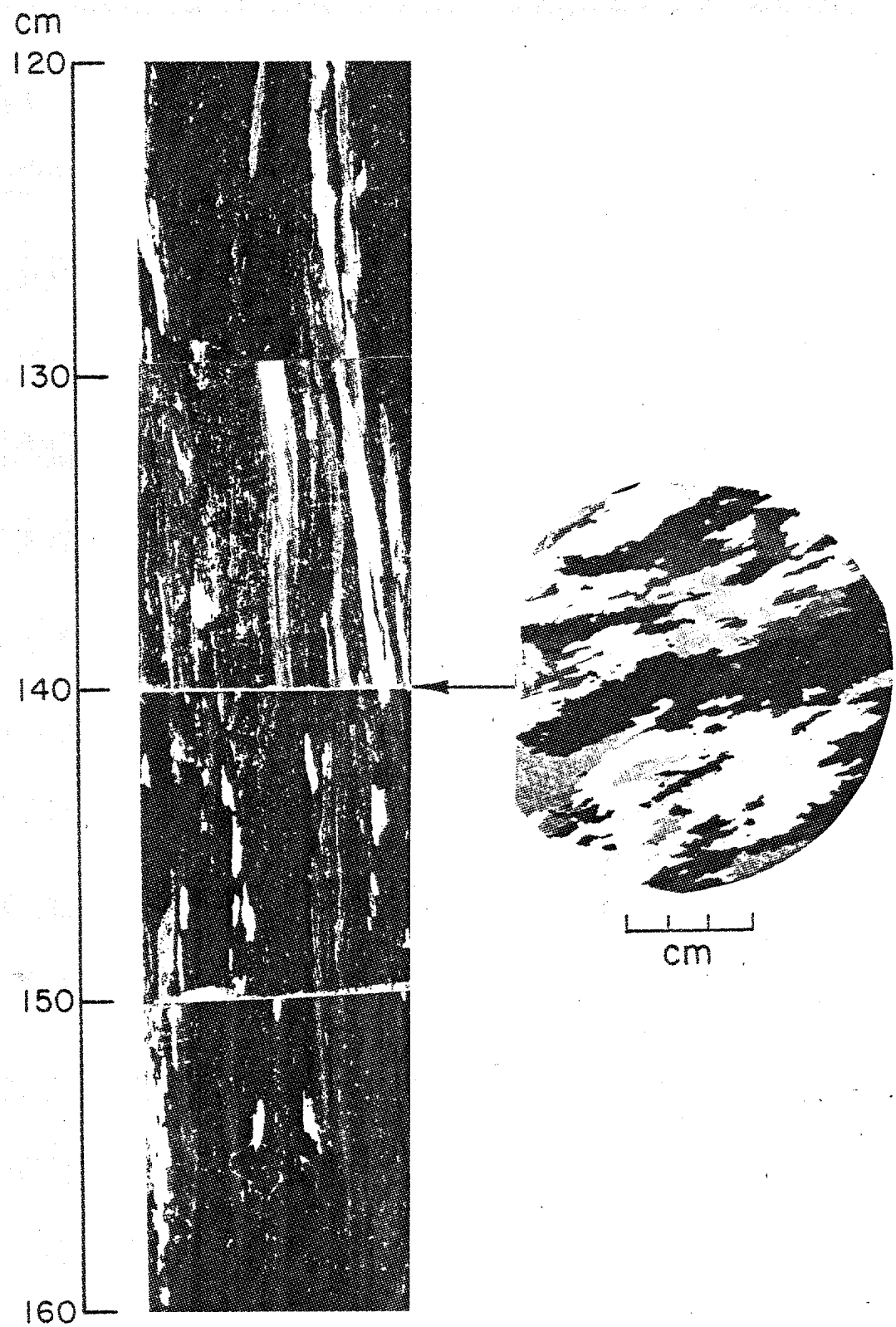
cm
120
130
140
150
160
cm

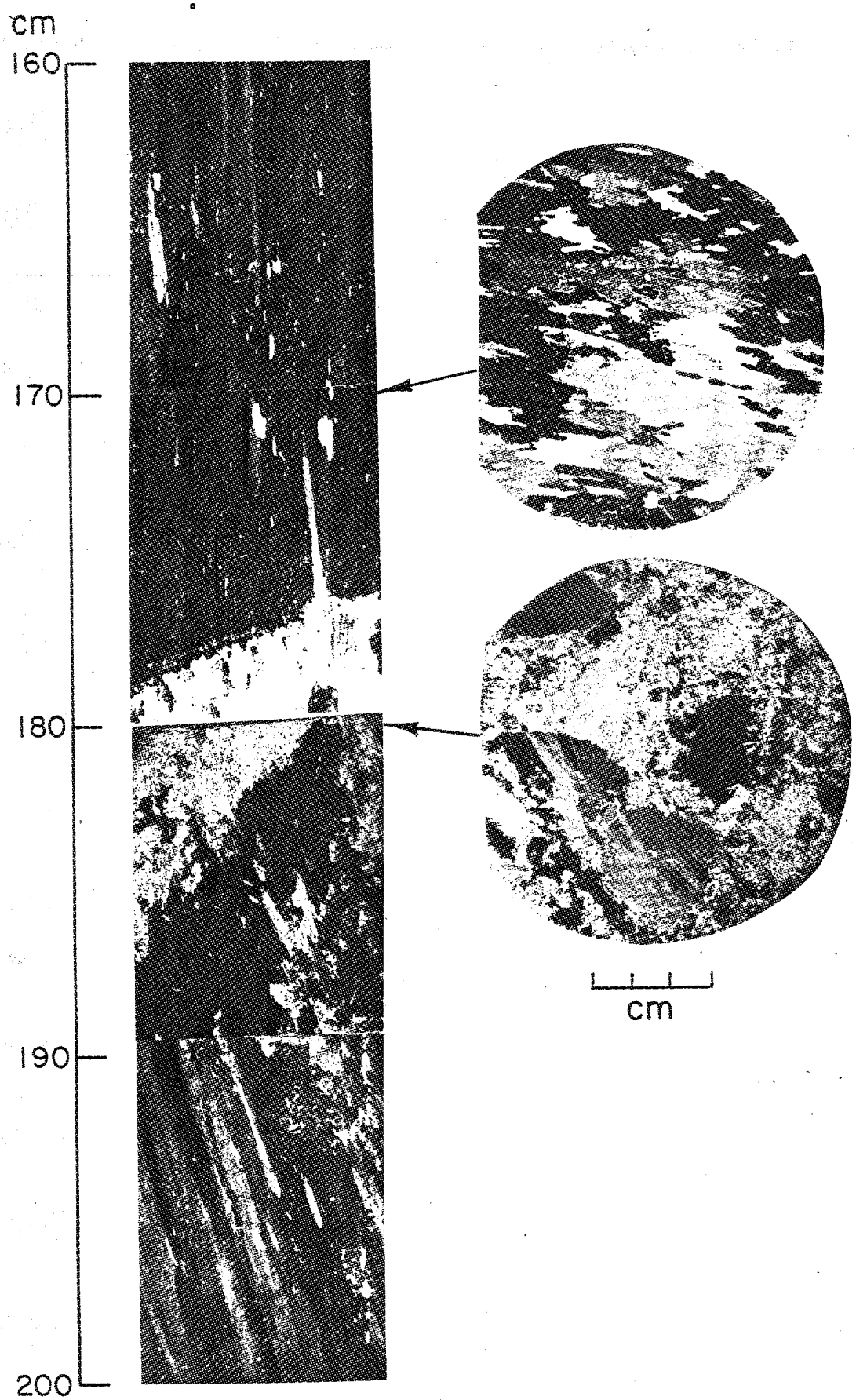
cm
160
170
180
190
200
cm

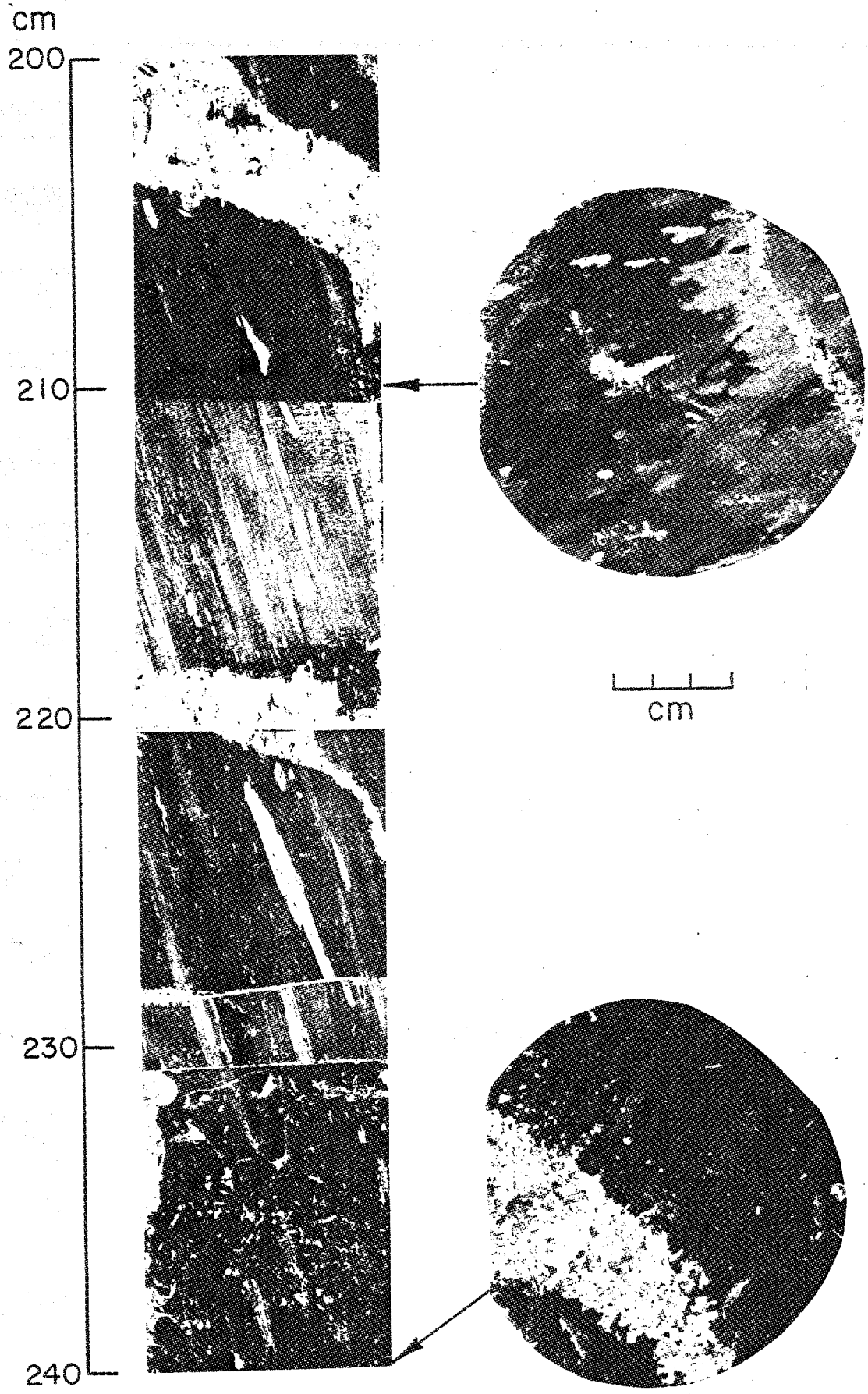
cm
200
210
220
230
240
cm

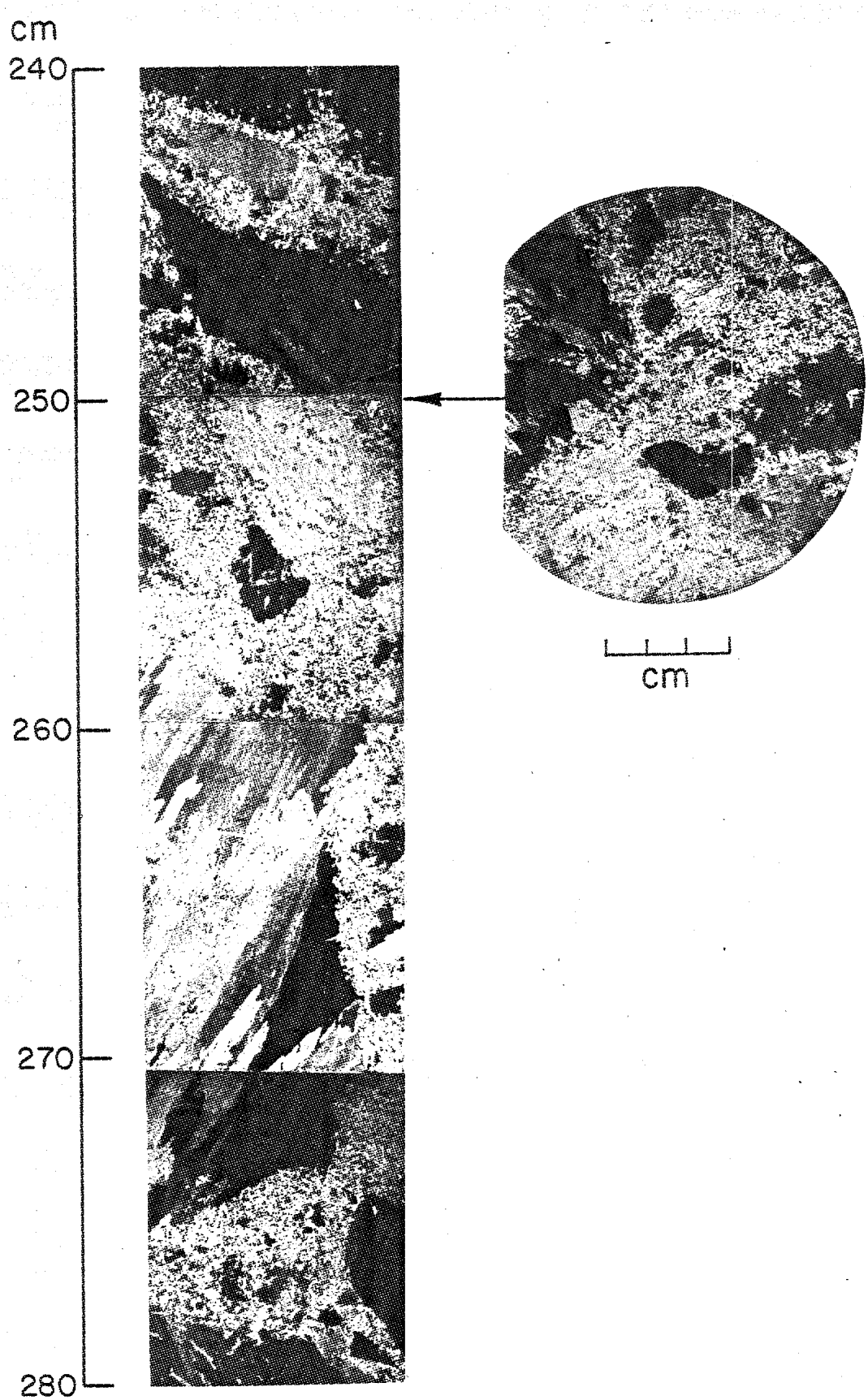
cm
240
250
260
270
280
cm

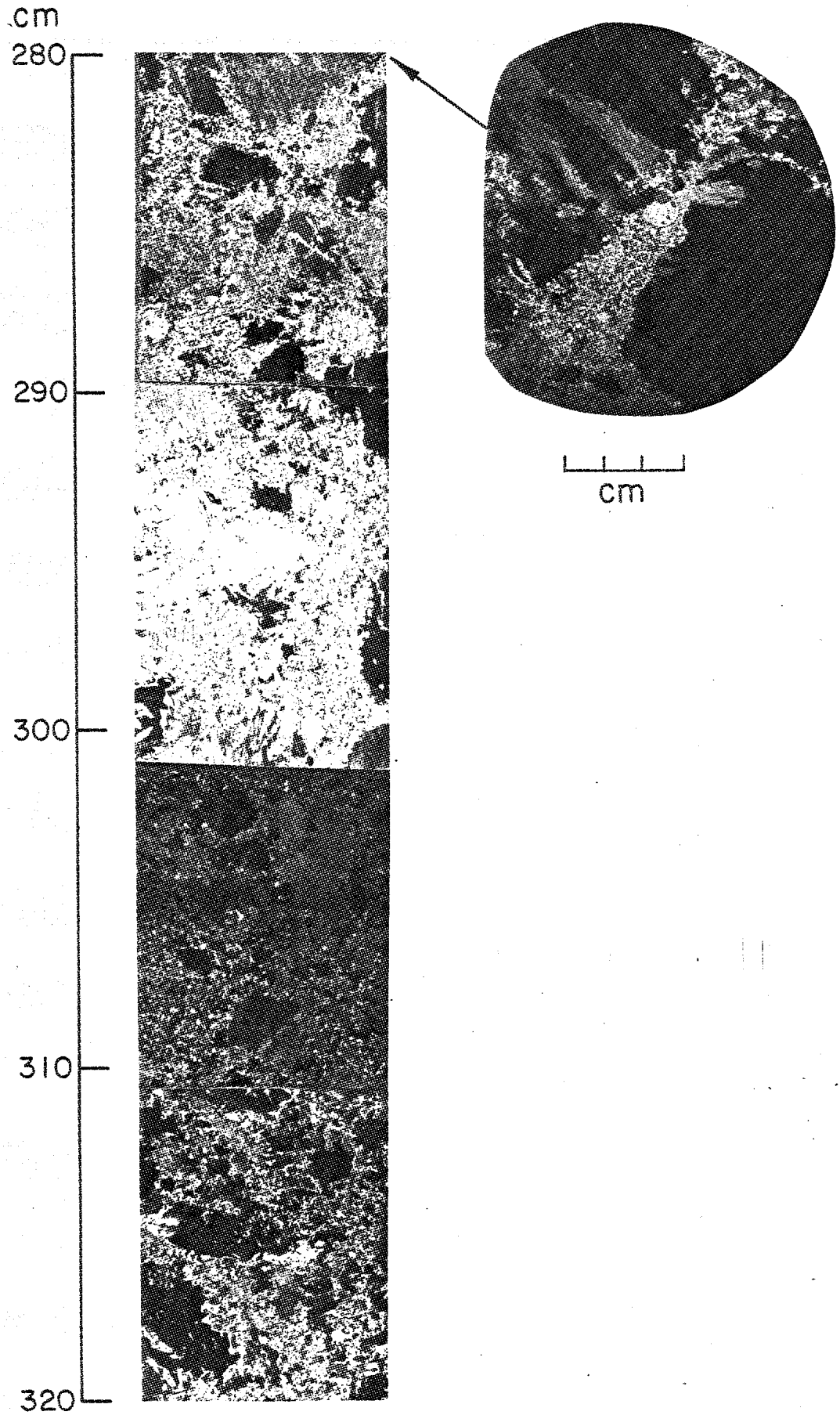
cm
280
290
300
310
320
cm

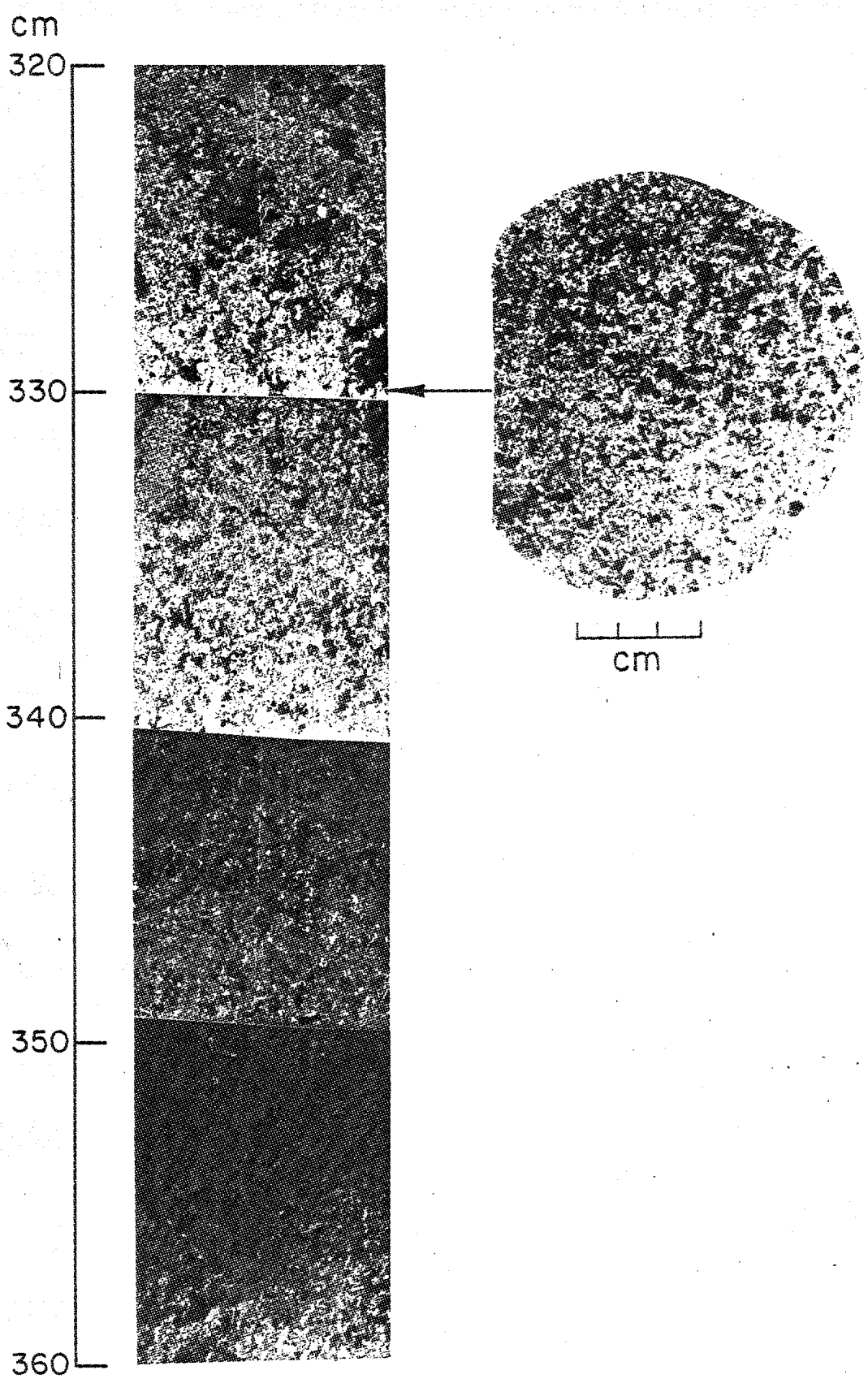
cm
320
330
340
350
360
cm

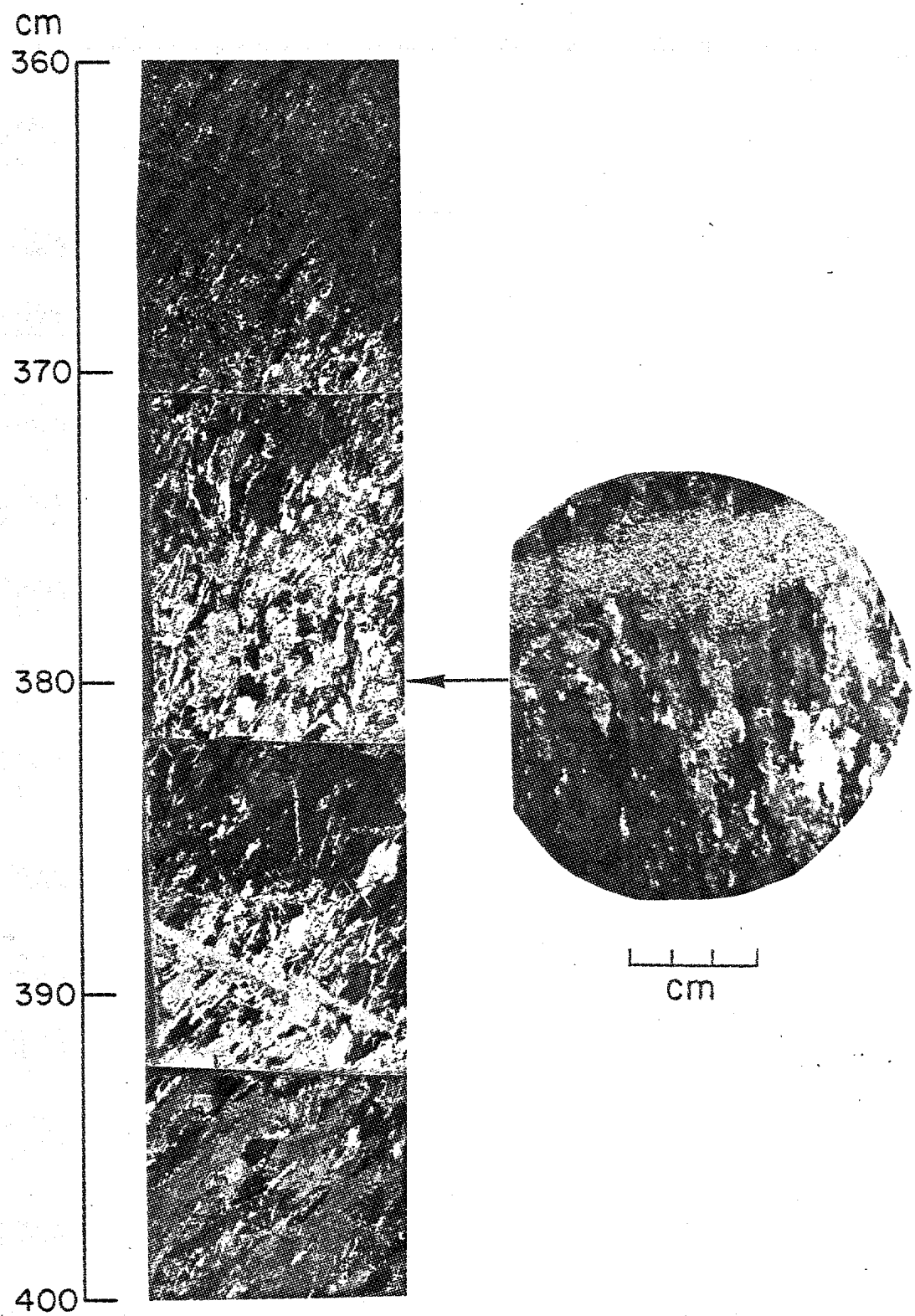
cm
360
370
380
390
400
cm

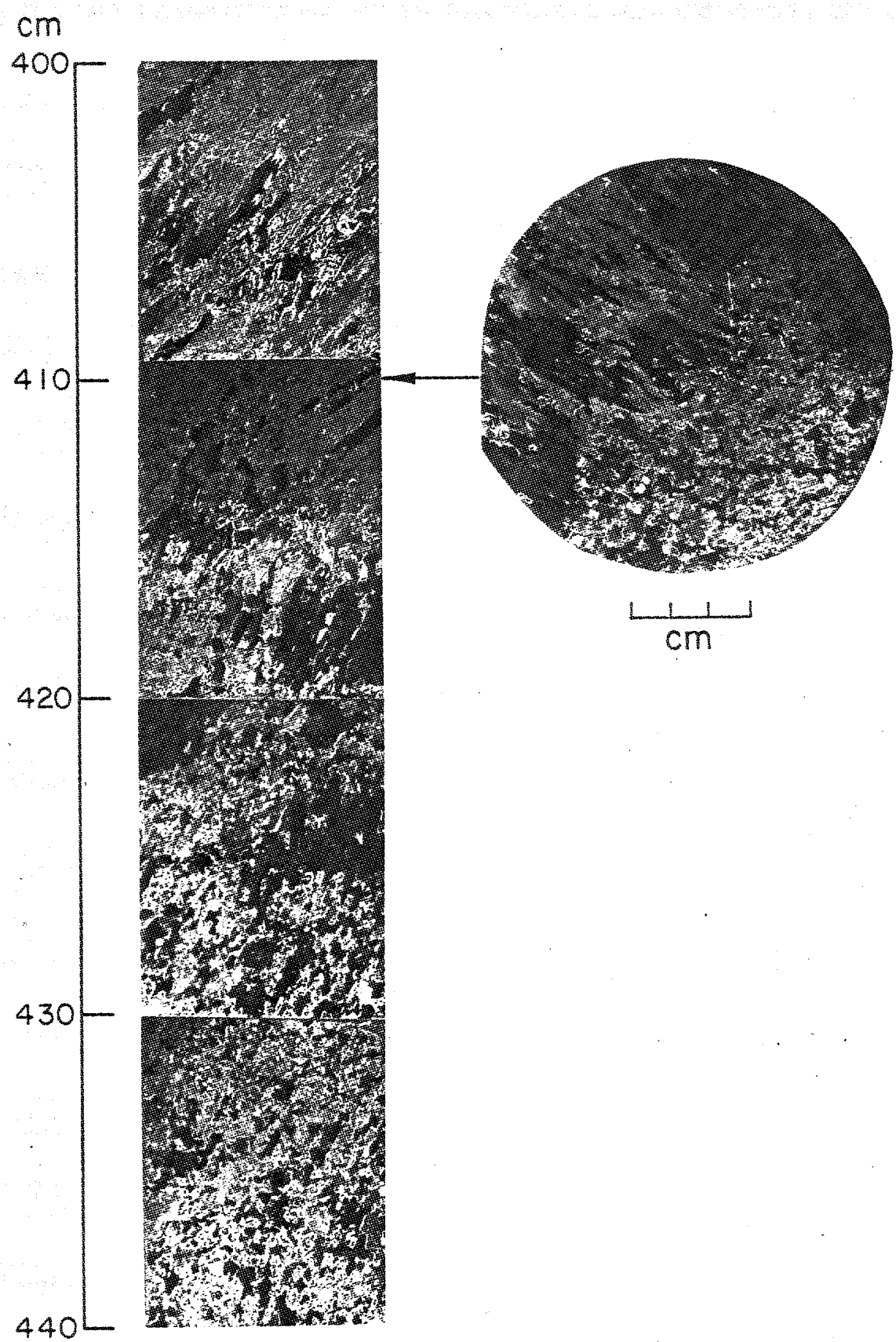
cm
400
410
420
430
440
cm

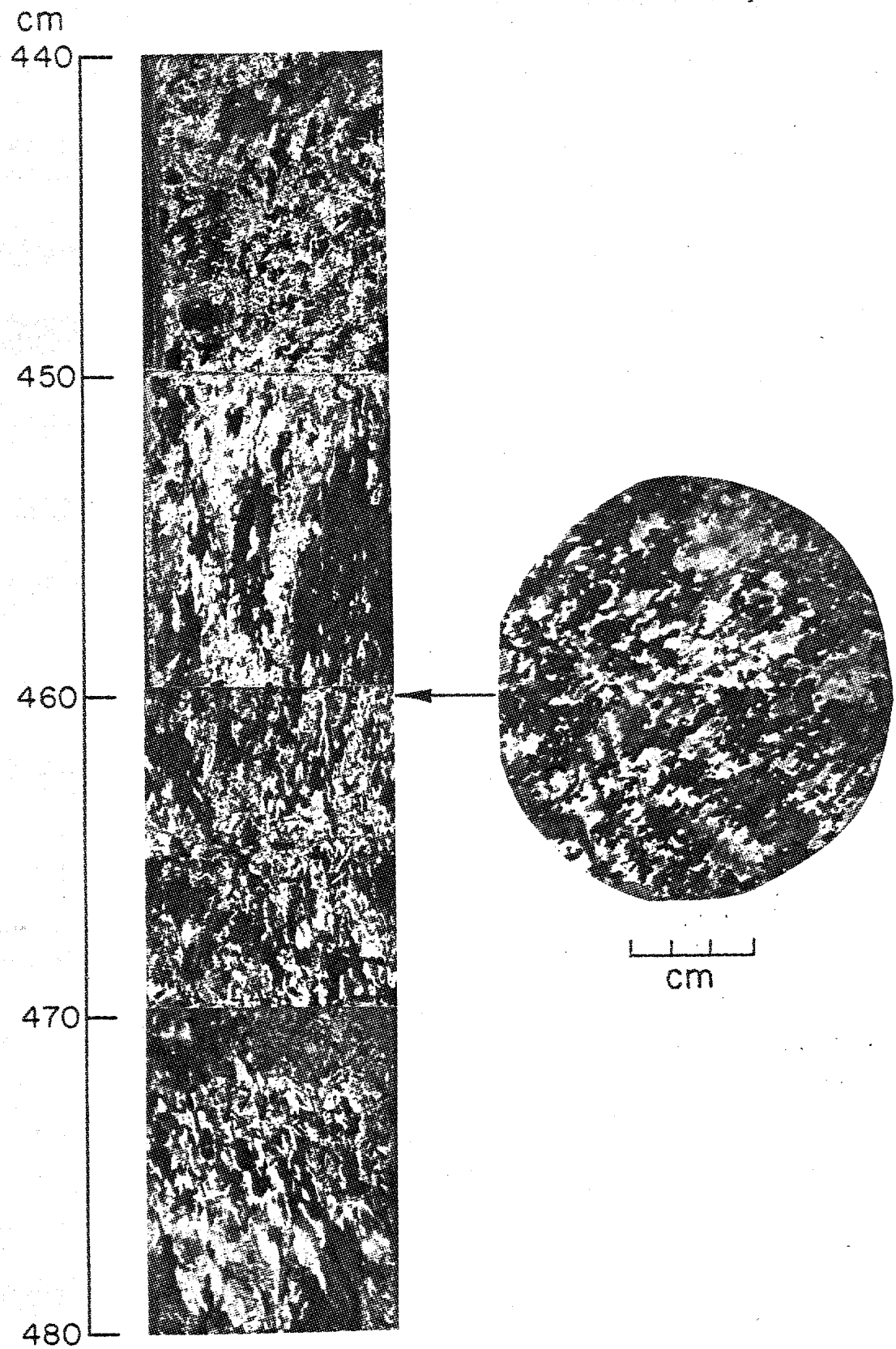
cm
440
450
460
470
480
cm

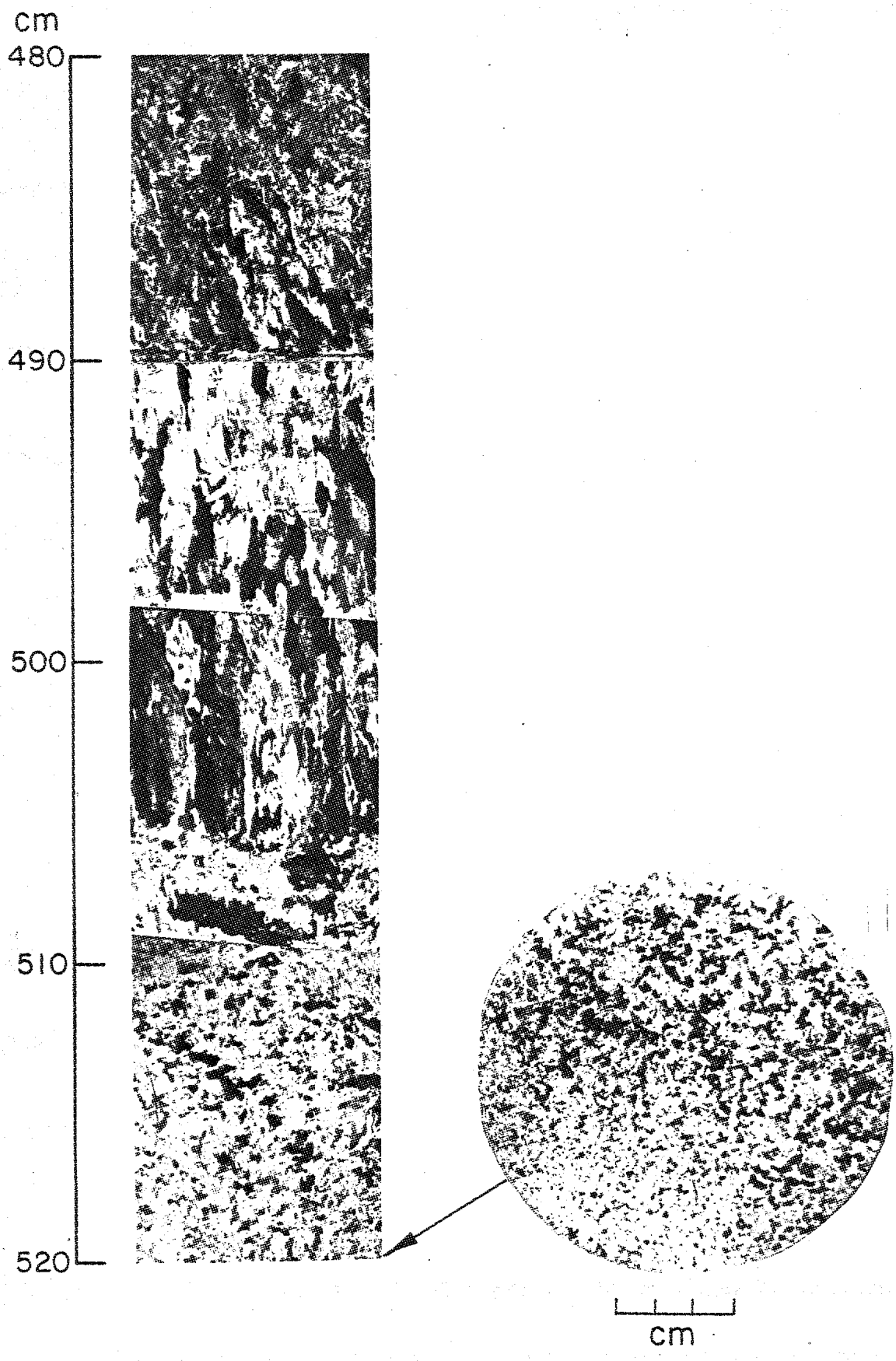
cm
480
490
500
510
520
cm

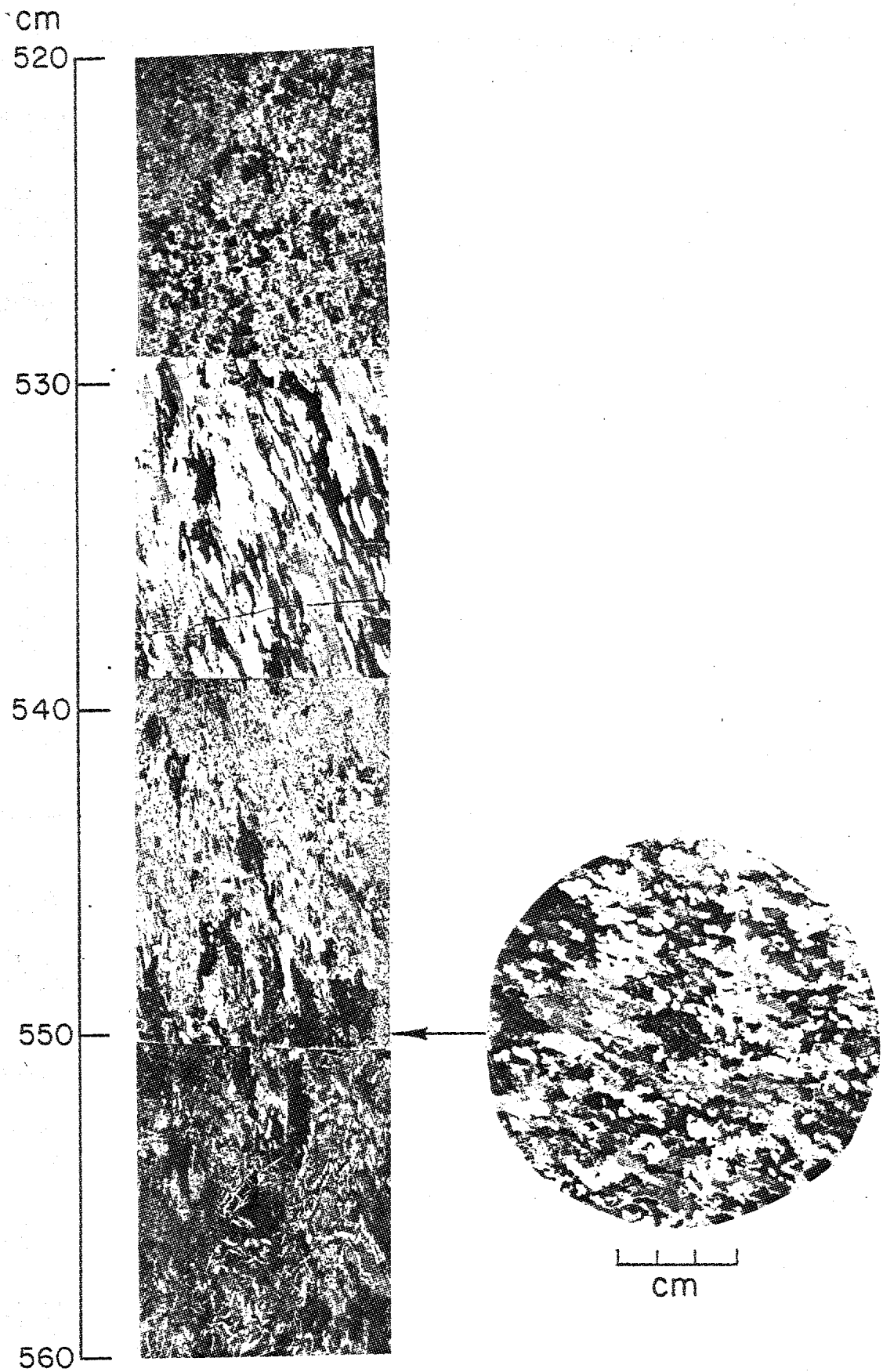
cm
520
530
540
550
560
cm

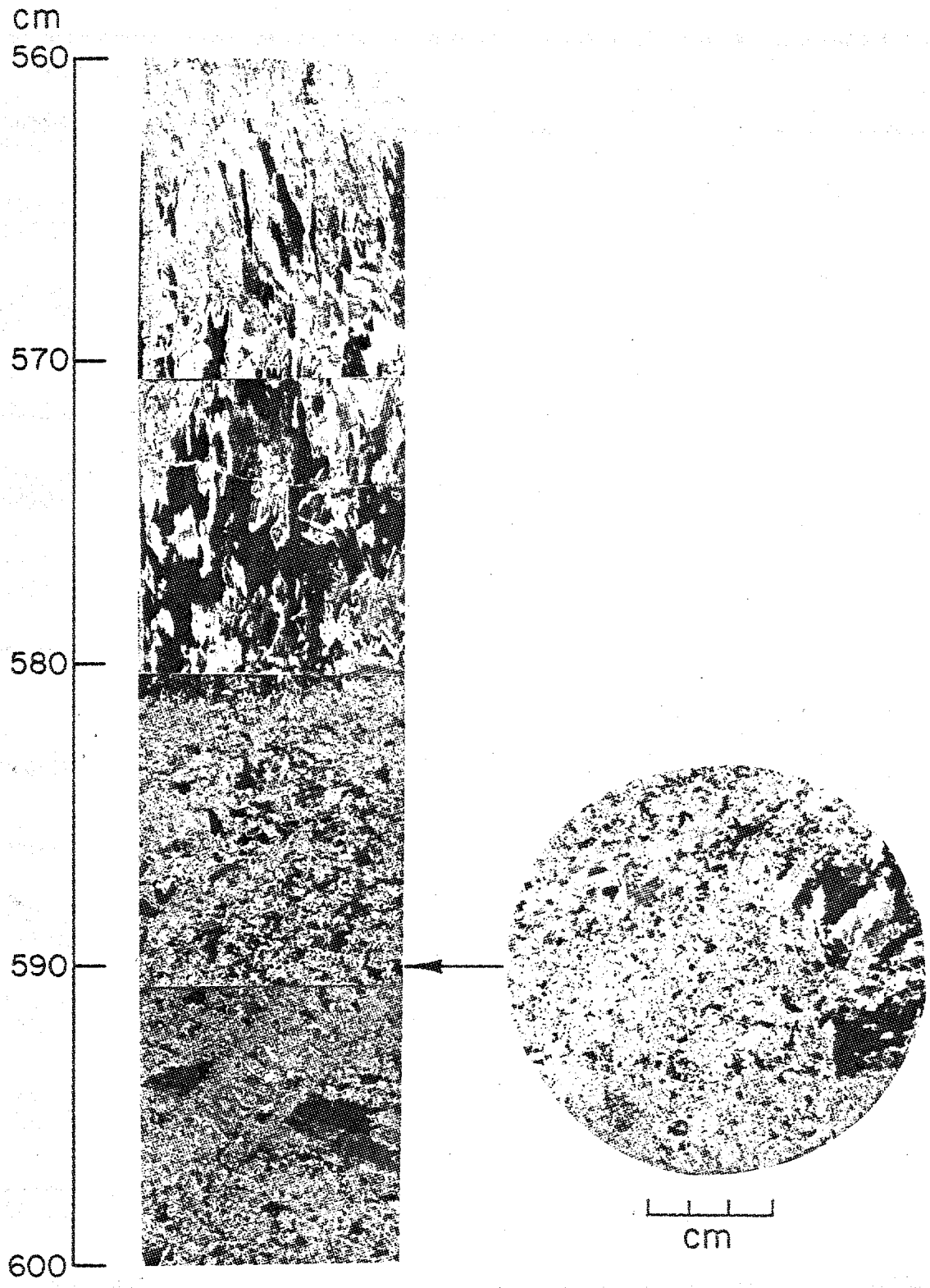
cm
560
570
580
590
600
cm

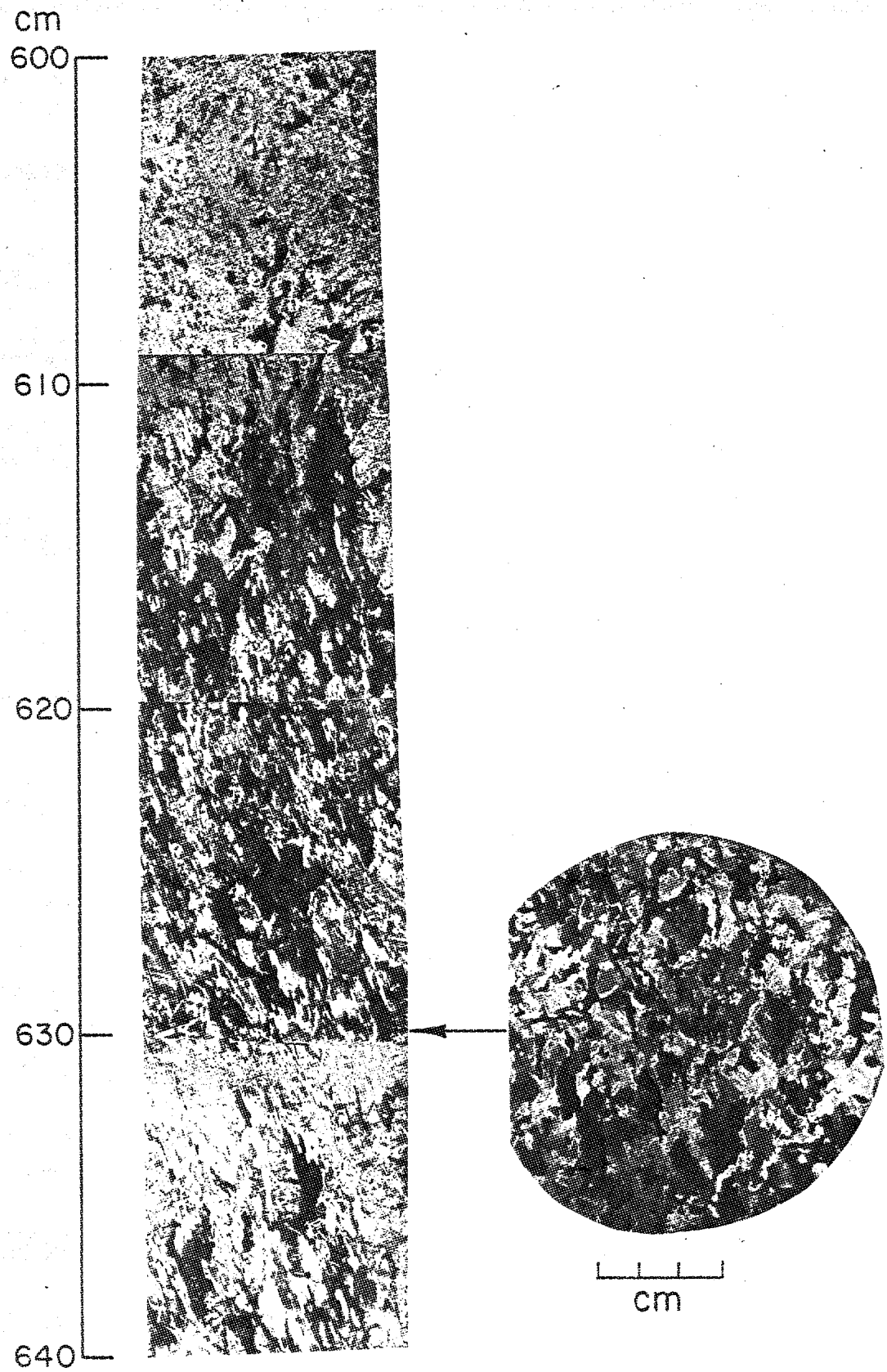
cm
600
610
620
630
640
cm

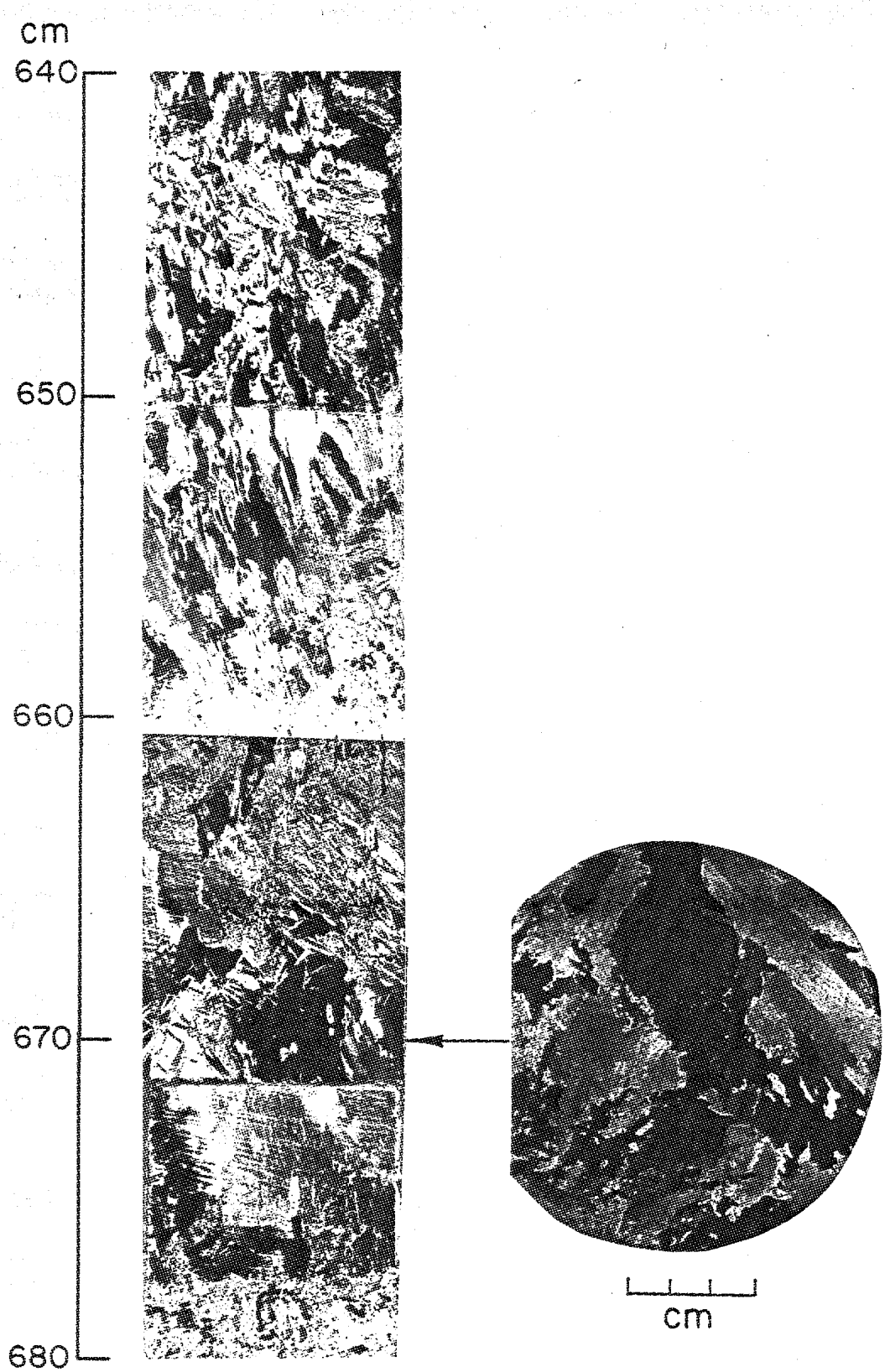
cm
640
650
660
670
680
cm

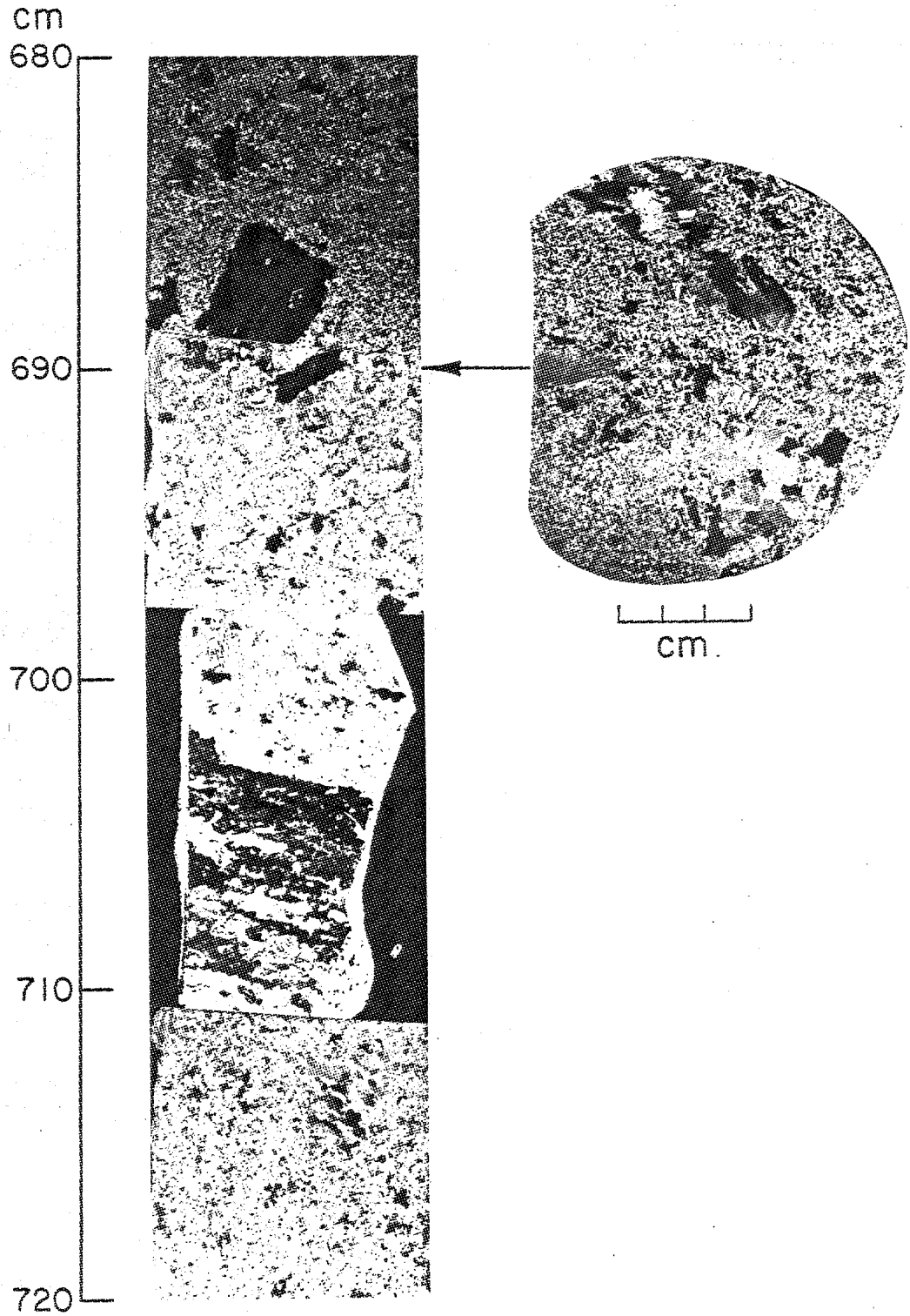
cm
680
690
700
710
720
cm.

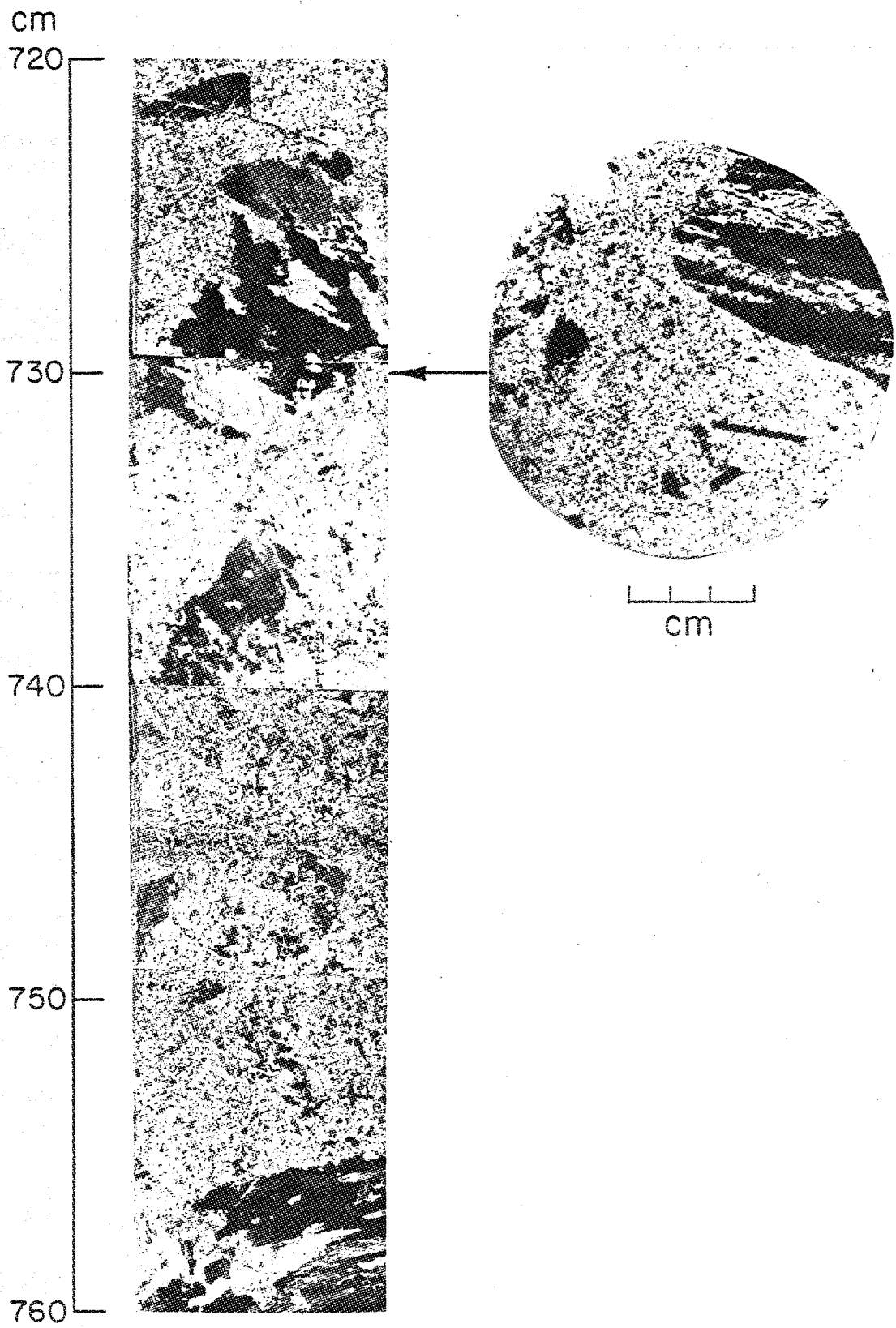
cm
720
730
740
750
760
cm

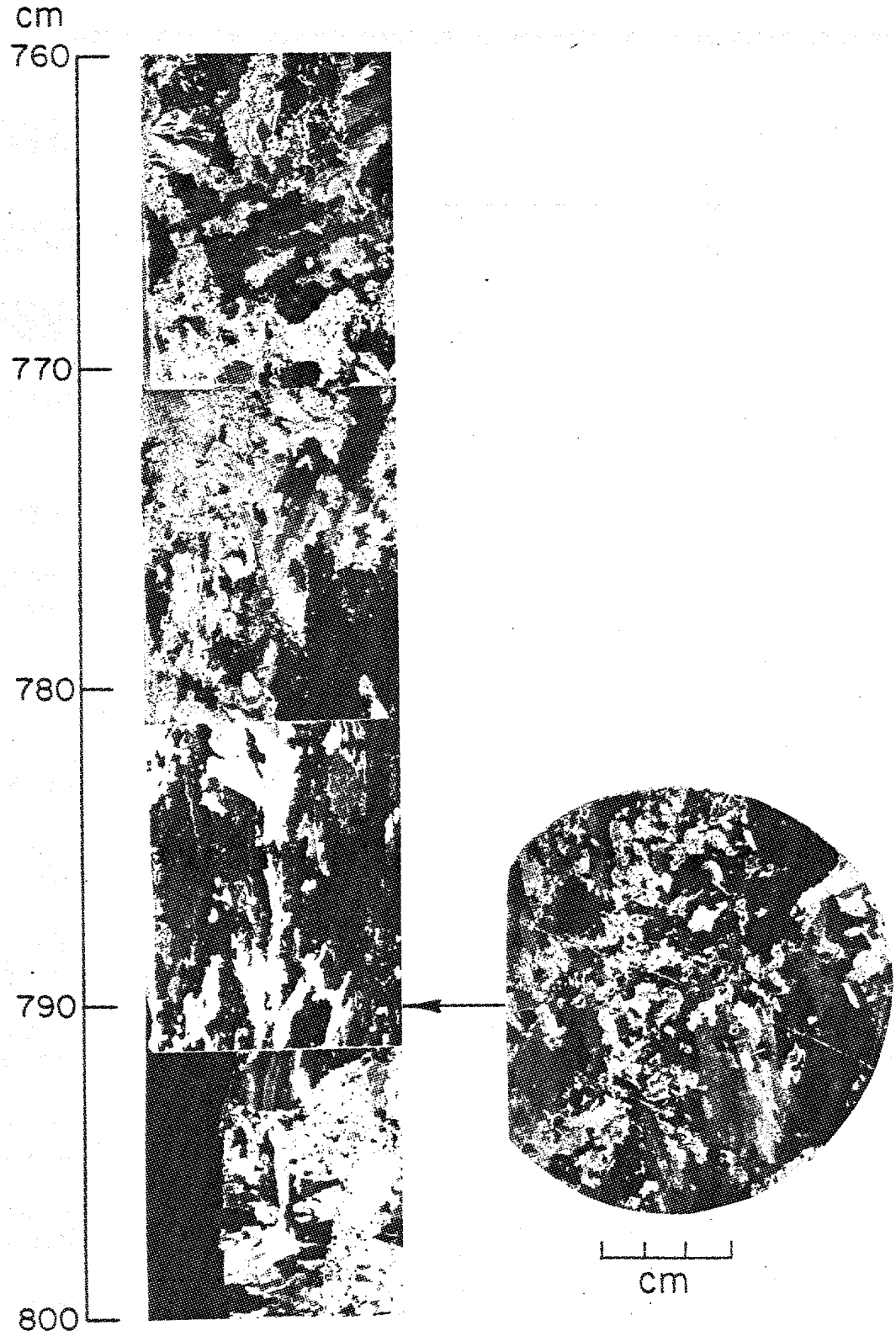
cm
760
770
780
790
800
cm

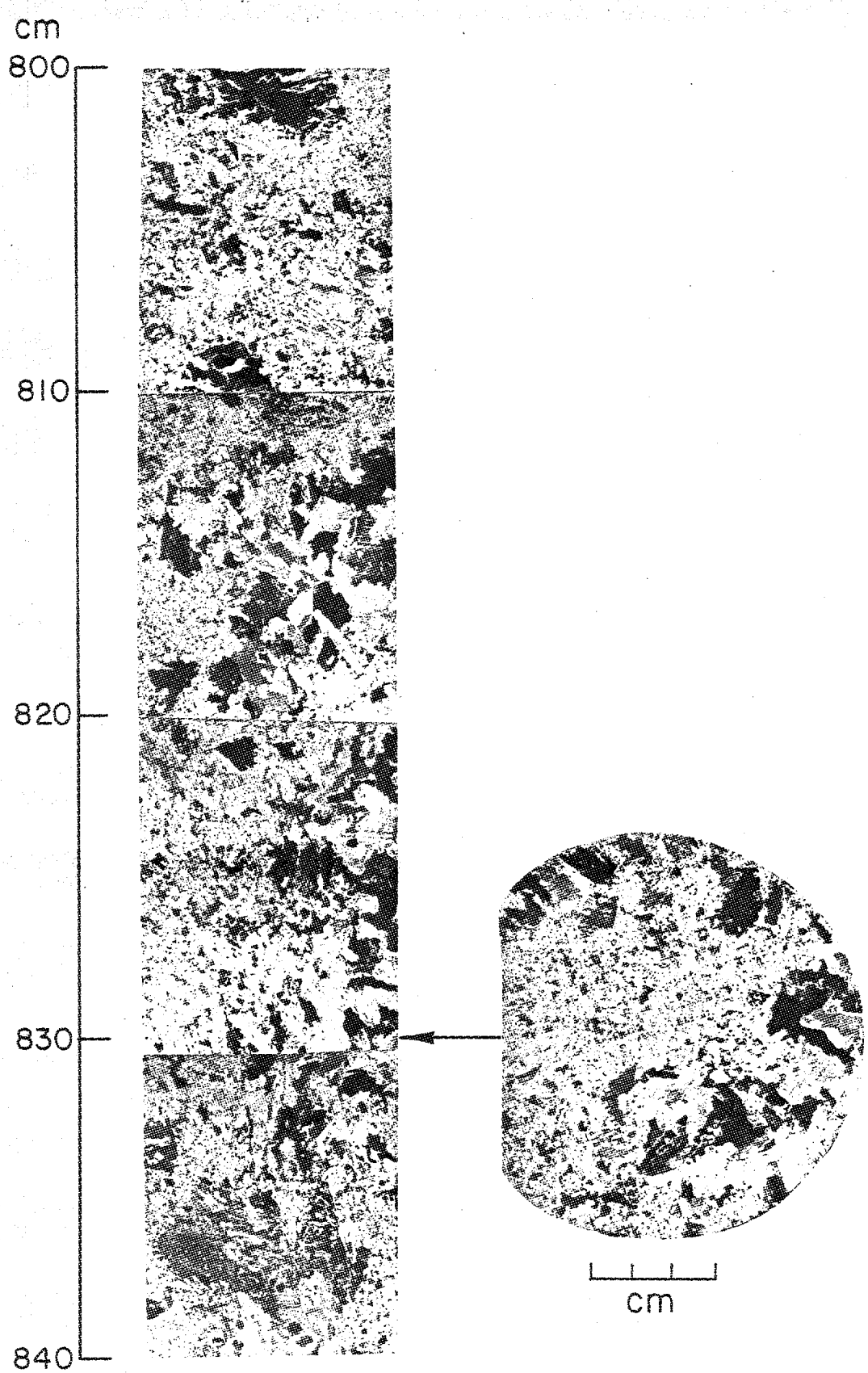
cm
800
810
820
830
840
cm

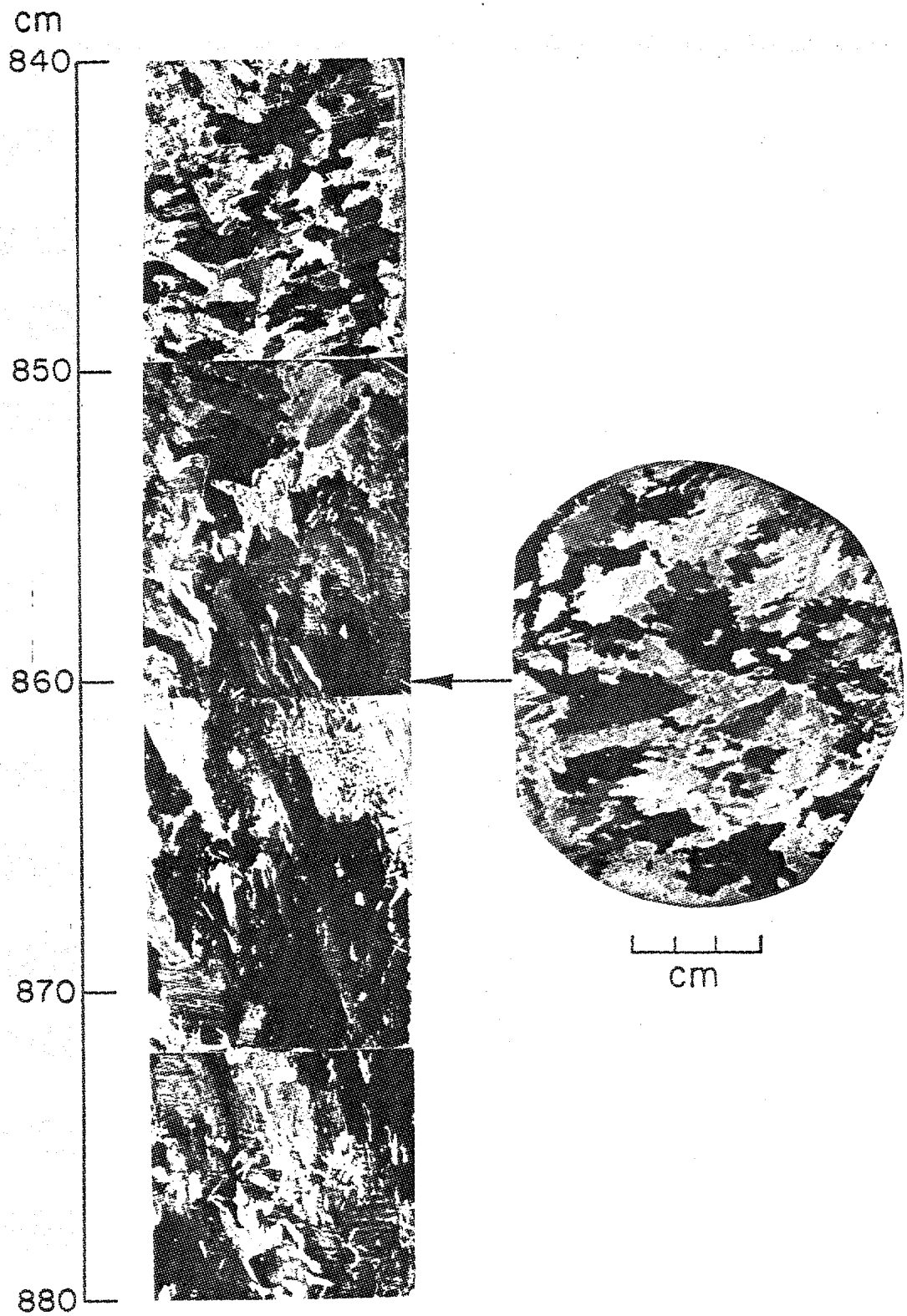
cm
840
850
860
870
880
cm

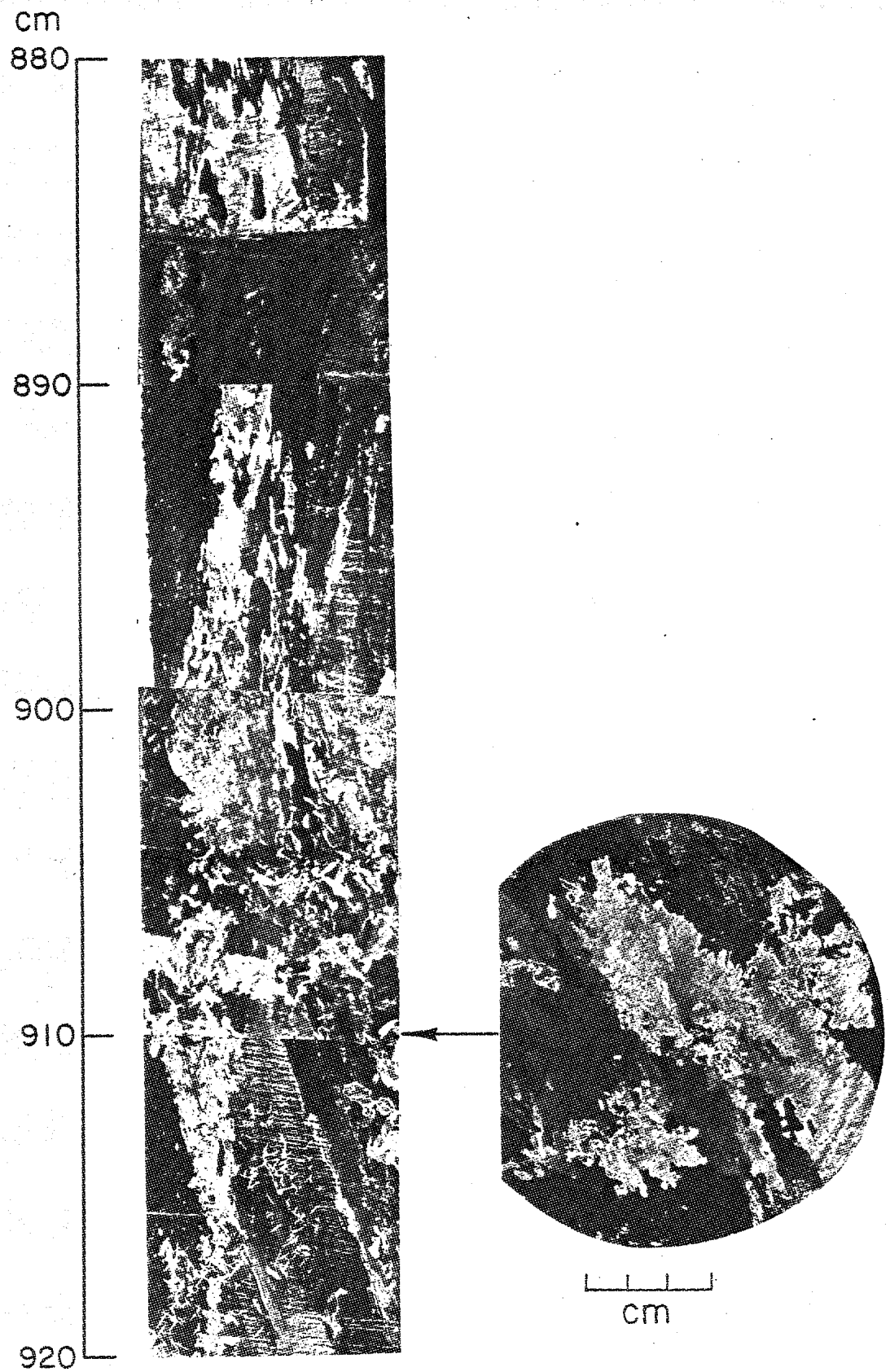
cm
880
890
900
910
920
cm

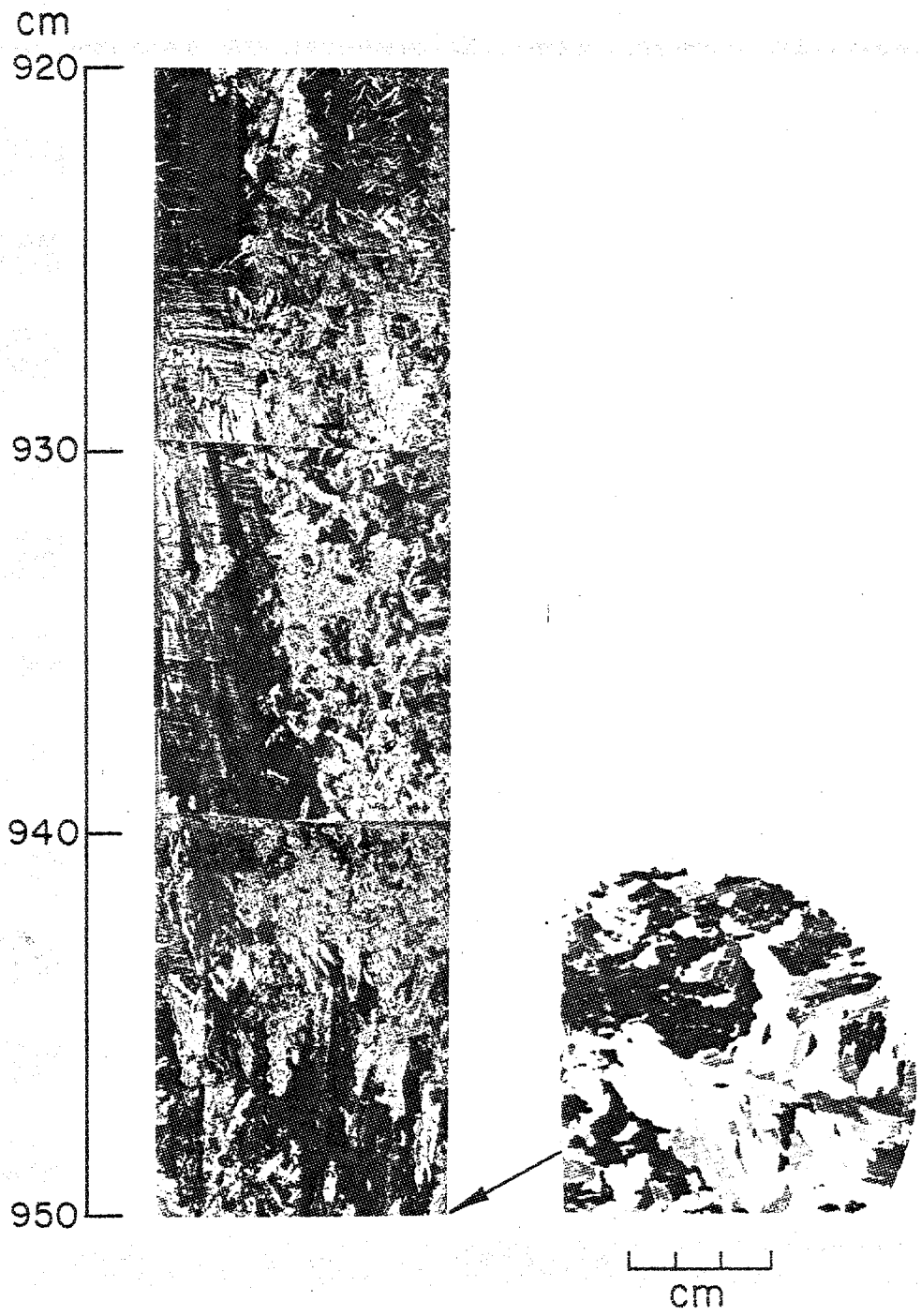
cm
920
930
940
950
cm

APPENDIX B

CONSTANT STRAIN-RATE COMPRESSION DATA

This appendix contains the results from the constant strain-rate, uniaxial compression tests (CSC). The parameters listed for each test are defined in Index B. CSC - 4-5 denotes those compression tests conducted at a strain-rate of 10^{-4} s^{-1} and a temperature of -5°C (23°F), etc. The sample number RC32-133/160V gives the location and depth of the sample, that is, Ridge C, hole 32, at a depth of 133 to 160 cm. V indicates a vertically oriented sample and H a horizontal sample.

INDEX B

Column No.	Symbol	Description
1	σ_m(psi)	Peak stress, or strength
2	ε_m(GL)(%)	Strain at σ_m determined by the DCDTs over a gauge length of 5.5 in. (4.5 in. for tension tests)
3	e_m(FS)(%)	Strain at σ_m determined by the extensometer over the full sample length of 10 in.
4	t_m(S)	Time to peak stress
5	σ_e(psi)	Stress at end of test
6	ε_e(FS)(%)	Full sample strain at end of test
7	t_e(s)	Time to end of test
8	E_i(GL)(10^6 psi)	Initial tangent modulus determined using strains found over the gauge length
9	E_0(GL)(10^6 psi)	Secant modulus determined using gauge length strains
10	E_0(FS)(10^6 psi)	Secant modulus determined using full sample strains
11	S_i(°/oo)	Sample salinity at test temperature
12	ρ(lb/ft^3)	Sample weight density at test temperature
13	V_b(^{0}/oo)	Brine volume at test temperature
14	V_a(^{0}/oo)	Air volume at test temperature
15	n(^{0}/oo)	Porosity at test temperature
16	σ_e/σ_m	Ratio of end to peak stress at 5% full sample strain
17	Ice squareness (in.)	Sample squareness departure after ends are milled
18	End cap squareness (in.)	Sample squareness departure after end caps are mounted
19	Shim (in.)	Amount of shim stock inserted between low end of sample and actuator before testing

FILE CSC-4-5

SAMPLE # 01	02	03	04	05	06	07	08	09	10	11	12	13	14	15	16	17	18	19
RC32-133/160V																		
330	0.150	0.170	16.50	195	5.00	500.0	0.771	0.220	0.194	1.17	53.50	10.8	68.0	78.8	0.591	0.003	0.006	0.006
RC43-150H																		
386	0.110	0.110	10.60	223	5.00	500.0	0.739	0.351	0.351	0.48	51.62	4.3	99.7	104.0	0.578	0.048	0.010	0.010
RC33-205/232V																		
478	0.100	0.090	7.80	207	5.00	500.0	0.983	0.478	0.531	3.05	55.18	29.0	41.6	70.6	0.433	0.007	0.005	0.005
RC43-222H																		
402	0.260	0.270	25.40	203	5.00	500.0	0.871	0.155	0.149	1.82	54.98	17.3	43.1	60.4	0.505	0.090	0.012	0.012
RC46-047/073V																		
362	0.090	0.080	7.10	131	5.00	500.0	0.807	0.402	0.453	0.92	54.24	8.6	54.6	63.3	0.362	0.009	0.003	0.003
RC44-073H																		
326	0.090	0.040	5.90	123	5.00	500.0	0.921	0.362	0.815	1.28	53.13	11.7	74.5	86.2	0.377	0.027	0.016	0.016
RC44-060H																		
227	0.110	0.110	11.70	91	5.00	500.0	0.639	0.206	0.206	1.23	50.69	10.8	116.9	127.7	0.403	0.033	0.000	0.004
RC46-083/110V																		
800	0.620	0.400	37.70	247	5.00	500.0	1.068	0.129	0.200	2.62	55.12	24.9	41.8	66.7	0.309	0.006	0.005	0.005
RC44-086H																		
390	0.110	0.090	9.80	95	5.00	500.0	0.999	0.355	0.433	1.85	57.03	18.2	7.6	25.8	0.245	0.035	0.009	0.009
RC46-147/173V																		
271	0.150	0.120	14.00	115	5.00	500.0	0.846	0.181	0.226	2.99	55.19	28.5	41.2	69.7	0.424	0.006	0.003	0.003
RC44-156H																		
175	0.060	0.090	5.50	139	5.00	500.0	0.834	0.292	0.194	2.64	55.89	25.5	28.5	54.0	0.794	0.013	0.004	0.004
RC44-256H																		
271	0.080	0.080	6.60	111	5.00	500.0	0.818	0.339	0.339	2.62	55.74	25.2	31.2	56.4	0.410	0.033	0.015	0.013
RC47-025/053V																		
322	0.100	0.090	9.00	127	5.00	500.0	0.782	0.322	0.358	1.05	53.25	9.6	72.2	81.8	0.394	0.005	0.011	0.011
RC45-040H																		
306	0.060	0.080	6.30	111	5.00	500.0	0.671	0.510	0.383	0.30	49.32	2.6	139.6	142.2	0.363	0.045	0.041	0.041
RC47-191/217V																		
669	0.110	0.070	6.00	163	5.00	500.0	1.144	0.608	0.956	2.83	56.25	27.5	22.7	50.2	0.244	0.007	0.013	0.013
RC44-204H																		
561	0.160	0.180	16.60	151	5.00	500.0	1.074	0.351	0.312	3.91	57.19	38.6	8.2	46.7	0.269	0.034	0.001	0.001
RC47-275/302V																		
326	0.170	0.200	18.50	123	5.00	500.0	0.815	0.192	0.163	4.31	56.67	42.1	17.8	59.9	0.377	0.004	0.008	0.008
RC44-288H																		
366	0.120	0.130	15.00	163	5.00	500.0	0.854	0.305	0.282	2.16	54.43	20.3	53.3	73.5	0.445	0.034	0.015	0.015

FILE CSC-4-20

SAMPLE #	01	02	03	04	05	06	07	08	09	10	11	12	13	14	15	16	17	18	19
RC32-231/258V																			
	963	0.210	0.280	22.50	485	5.00	500.0	1.233	0.459	0.344	3.76	55.68	12.2	34.0	46.2	0.504	0.002	0.000	0.000
RC43-245H																			
	546	0.080	0.100	9.50	167	5.00	500.0	1.159	0.683	0.546	3.07	56.46	10.1	19.8	29.9	0.306	0.042	0.012	0.009
RC32-267/294V																			
	661	0.140	0.220	21.10	167	5.00	500.0	1.036	0.472	0.301	3.76	55.92	12.3	22.9	42.1	0.253	0.012	0.010	0.010
RC33-268/295V																			
	899	0.140	0.170	13.50	334	1.40	13.50	1.278	0.642	0.529	4.35	57.13	14.5	9.4	24.0		0.010	0.001	0.001
RC43-280H																			
	708	0.110	0.100	9.70	143	5.00	500.0	1.490	0.644	0.708	3.39	56.04	11.1	27.4	38.5	0.202	0.033	0.006	0.006
RC32-303/328V																			
	573	0.130	0.110	11.70	223	5.00	500.0	0.878	0.441	0.521	1.48	54.09	4.7	59.4	64.1	0.389	0.010	0.005	0.005
RC43-316H																			
	342	0.070	0.090	8.20	231	5.00	500.0	1.191	0.489	0.380	3.71	56.63	12.3	17.5	29.8	0.675	0.025	0.027	0.027
RC32-343/369V																			
	485	0.170	0.240	23.90	175	5.00	500.0	0.776	0.285	0.202	2.51	52.92	7.8	80.7	88.5	0.361	0.006	0.015	0.015
RC43-357H																			
	597	0.140	0.130	14.40	239	5.00	500.0	0.965	0.426	0.459	1.67	54.45	5.3	53.4	58.7	0.400	0.038	0.006	0.006
RC33-242/268V																			
	947	0.190	0.190	19.40	700	0.59	61.00	1.287	0.498	0.498	5.01	56.94	16.7	13.4	30.1		0.005	0.005	0.005
RC43-257H																			
	541	0.100	0.100	11.00	215	5.00	500.0	1.144	0.541	0.541	3.61	56.92	12.0	12.4	24.4	0.397			0.008
RC33-368/395V																			
	939	0.180	0.160	14.20	247	5.00	500.0	1.101	0.522	0.587	4.52	56.20	14.8	25.7	40.6	0.263	0.006	0.004	0.004
RC43-381H																			
	867	0.130	0.150	14.30	207	5.00	500.0	1.179	0.667	0.578	0.44	55.74	1.3	29.7	31.0	0.239	0.025	0.003	0.003
RC46-121/147V																			
	517	0.100	0.100	10.50	163	5.00	500.0	1.101	0.517	0.517	2.58	53.89	8.1	64.0	72.1	0.315	0.012	0.006	0.006
RC44-128H																			
	255	0.080	0.090	9.50	151	5.00	500.0	0.952	0.319	0.283	3.27	56.60	10.8	17.6	28.4	0.592	0.037	0.009	0.009
RC46-173/199V																			
	493	0.110	0.120	12.10	175	5.00	500.0	0.873	0.448	0.411	1.70	53.77	5.3	65.1	70.4	0.355	0.009	0.008	0.008
RC44-186H																			
	1018	0.130	0.110	12.40	302	5.00	500.0	1.292	0.783	0.926	3.68	56.51	12.1	19.4	31.6	0.297	0.024	0.006	0.006
RC46-276/303V																			
	629	0.120	0.120	13.40	223	5.00	500.0	0.952	0.524	0.524	1.02	53.72	3.2	65.5	68.7	0.355	0.006	0.005	0.005
RC44-299H																			
	609	0.120	0.120	13.50	269	5.00	500.0	0.900	0.508	0.508	1.60	54.99	5.1	43.8	48.9	0.442	0.058	0.013	0.013

RC47-090/116V																				
1798	0.190	0.210	20.70	1397	0.27	25.70	1.311	0.946	0.856	3.49	55.92	11.4	29.6	41.0		0.026	0.002	0.002		
RC44-103H																				
505	0.100	0.080	7.30	195	5.00	500.0	1.101	0.505	0.631	3.09	56.18	10.1	24.7	34.8	0.386	0.032	0.006	0.005		
RC44-116H																				
243	0.070	0.070	6.60	111	5.00	500.0	0.921	0.347	0.347	3.31	56.79	11.0	14.3	25.3	0.457	0.010	0.005	0.005		
RC47-127/153V																				
1846	0.180	0.120	14.60	1846	0.12	14.60	1.406	1.026	1.538	3.28	56.16	10.8	25.2	36.0		0.011	0.004	0.004		
RC44-141H																				
287	0.080	0.110	9.30	135	5.00	500.0	0.896	0.359	0.261	3.54	57.35	11.9	4.7	16.6	0.470	0.040	0.003	0.003		
RC47-302/329V																				
875	0.110	0.100	10.00	247	5.00	500.0	1.352	0.796	0.875	2.57	56.71	8.5	15.0	23.5	0.282	0.005	0.009	0.009		

FILE CSC-2-5

SAMPLE #	01	02	03	04	05	06	07	08	09	10	11	12	13	14	15	16	17	18	19
RA01-262/289	820	0.100	0.120	0.14	820	0.12	0.14	0.709	0.820	0.586	0.43	53.89	4.0	60.1	64.1		0.003	0.007	0.007
RA06-131/158	390	0.050	0.060	0.07	390	0.06	0.07	0.785	0.780	0.650	0.04	48.69	0.3	150.2	150.6		0.010	0.006	0.006
RA06-337/364	621	0.070	0.110	0.11	621	0.11	0.11	0.869	0.887	0.565	1.35	51.74	12.0	98.9	110.9		0.011	0.003	0.003
RC29-112/139	708	0.070	0.030	0.09	708	0.03	0.09	0.992	1.011	2.360	0.85	56.15	8.2	21.3	29.5		0.004	0.010	0.014
RC29-179/206	716	0.080	0.080	0.11	716	0.08	0.11	0.947	0.895	0.895	1.44	55.70	13.8	30.0	43.9		0.010	0.002	0.002
RC29-342/369	470	0.020	0.060	0.08	470	0.06	0.08	0.840	2.350	0.783	2.46	55.00	23.3	43.8	67.1		0.012	0.005	0.005
RC31-125/152	788	0.080	0.110	0.13	788	0.11	0.13	1.000	0.985	0.716	0.39	54.64	3.7	47.0	50.7		0.008	0.011	0.011
RC31-197/224	645	0.070	0.090	0.12	645	0.09	0.12	0.975	0.921	0.717	2.61	55.00	24.8	44.0	68.8		0.005	0.006	0.006
RC31-278/305	931	0.080	0.100	0.12	931	0.10	0.12	0.995	1.164	0.931	1.84	56.92	18.1	9.5	27.5		0.004	0.003	0.003

FILE CSC-2-20

SAMPLE # 01	02	03	04	05	06	07	08	09	10	11	12	13	14	15	16	17	18	19
RA01-009/036																		
597	0.080	0.100	0.12	597	0.10	0.12	0.765	0.746	0.597	0.01	46.95	0.0	182.4	182.4		0.003	0.003	0.003
RA01-078/105																		
1130	0.130	0.140	0.16	1130	0.14	0.16	0.887	0.869	0.807	0.02	50.14	0.1	126.9	126.9		0.006	0.004	0.004
RA01-339/366																		
1361	0.130	0.140	0.16	1361	0.14	0.16	1.068	1.047	0.972	0.63	55.42	2.0	35.5	37.5		0.004	0.003	0.003
RA01-428/455																		
1476	0.160	0.160	0.17	1476	0.16	0.17	1.024	0.923	0.923	0.98	55.68	3.2	31.3	34.5		0.037	0.010	0.010
RA06-058/085																		
971	0.090	0.120	0.13	971	0.12	0.13	1.522	1.079	0.809	0.02	52.04	0.1	93.8	93.8		0.007	0.017	0.017
RA06-266/293																		
1194	0.130	0.120	0.15	1194	0.12	0.15	0.882	0.919	0.995	0.24	50.51	0.7	120.6	121.3		0.008	0.003	0.003
RC29-251/278																		
1448	0.130	0.120	0.16	1448	0.12	0.16	1.232	1.114	1.207	2.58	56.51	8.5	18.5	27.0		0.006	0.004	0.004
RC31-350/377																		
1058	0.090	0.090	0.13	1058	0.09	0.13	1.156	1.176	1.176	2.14	56.19	7.0	23.6	30.6		0.006	0.007	0.007
RC31-416/443																		
1520	0.120	0.160	0.18	1520	0.16	0.18	1.255	1.267	0.950	1.83	57.07	6.1	8.0	14.1		0.004	0.001	0.001

APPENDIX C

CONSTANT STRAIN-RATE TENSION DATA

This appendix contains the results from the constant strain-rate, uniaxial tension tests (CST). The parameters listed for each tests are defined in Index B. CST-3-5 denotes those tension tests conducted at a strain-rate of 10^{-3} s^{-1} and a temperature of -5°C (23°F) etc. Tension sample numbers are defined in the same manner as compression sample numbers.

FILE CST-5-5

SAMPLE #	01	02	03	04	05	06	07	08	09	10	11	12	13	14	15	16	17	18	19
RA07-181/208	135	0.018	0.022	21.80				0.913	0.750	0.614	0.05	52.87	0.5	77.2	77.6		0.006	0.007	
RA09-036/063	149	0.022	0.026	21.20				1.100	0.677	0.573	0.03	50.85	0.3	112.3	112.6		0.006	0.009	
RA09-291/318	138	0.019	0.029	28.60				1.020	0.726	0.476	0.76	56.36	7.4	17.3	24.7		0.006	0.004	
RB20-129/156	94	0.014	0.014	14.00				0.990	0.676	0.676	0.94	53.25	8.6	71.9	80.5		0.006	0.000	
RB21-164/191	113	0.020	0.020	19.80				0.889	0.565	0.565	1.63	54.64	15.4	48.8	64.2		0.005	0.006	
RB21-196/223	82	0.019	0.032	32.30				0.887	0.432	0.257	1.99	55.31	19.0	37.5	56.5		0.007	0.009	
RB21-257/284	136	0.019	0.026	25.30				0.817	0.716	0.523	1.12	53.96	10.4	59.8	70.2		0.005	0.009	
RB22-018/045	94	0.021	0.025	24.90				0.786	0.451	0.378	0.02	49.33	0.2	138.9	139.1		0.010	0.005	
RB22-163/190	130	0.018	0.017	17.00				0.940	0.722	0.765	0.91	53.37	8.4	69.8	78.1		0.005	0.003	

FILE CST-5-20

SAMPLE # 01	02	03	04	05	06	07	08	09	10	11	12	13	14	15	16	17	18	19
RA03-192/219 93	0.010	0.010	9.80				1.134	0.935	0.935	0.03	53.64	0.1	65.8	65.9		0.006	0.005	
RA03-243/270 123	0.014	0.014	14.10				1.011	0.879	0.879	0.51	52.12	1.6	92.7	94.3		0.005	0.001	
RA03-341/368 126	0.014	0.016	15.50				1.069	0.900	0.788	1.41	55.46	4.6	35.4	40.0		0.007	0.002	
RA07-005/032 78	0.014	0.015	14.60				0.604	0.557	0.520	0.01	45.93	0.0	200.1	200.1		0.003	0.010	
RA09-129/156 92	0.011	0.012	12.10				0.967	0.841	0.771	0.08	52.69	0.2	82.4	82.6		0.011	0.007	
RA09-160/187 89	0.012	0.012	12.30				0.788	0.745	0.745	0.01	51.40	0.0	104.8	104.8		0.003	0.003	
RB14-185/212 71	0.009	0.011	10.60				0.919	0.793	0.649	0.47	53.23	1.5	73.3	74.8		0.005	0.003	
RB14-368/395 134	0.022	0.025	24.50				1.039	0.609	0.536	3.16	56.84	10.4	18.4	28.8		0.016	0.007	
RB20-231/258 124	0.012	0.018	15.80				1.006	1.033	0.689	0.97	55.03	3.1	42.5	45.6		0.005	0.008	

FILE CST-3-5

SAMPLE # 01	02	03	04	05	06	07	08	09	10	11	12	13	14	15	16	17	18	19
RA03-073/100																		
115	0.013	0.015	0.32				0.812	0.885	0.767	0.01	51.12	0.1	107.6	107.7		0.006	0.001	
RA07-149/176																		
116	0.011	0.012	0.33				1.124	1.055	0.967	0.04	52.53	0.4	83.1	83.4		0.015	0.005	
RA07-263/290																		
71	0.008	0.009	0.26				0.943	0.891	0.792	0.57	52.94	5.2	76.7	81.9		0.006	0.004	
RB14-232/259																		
76	0.008	0.009	0.26				0.945	0.950	0.844	3.43	53.13	31.4	77.7	109.2		0.049	0.012	
RB14-263/290																		
120	0.012	0.014	0.33				1.054	1.000	0.857	1.38	54.67	13.0	47.9	60.9		0.009	0.000	
RB20-039/066																		
60	0.007	0.008	0.23				0.977	0.863	0.755	0.21	50.60	1.8	116.9	118.8		0.006	0.006	
RB20-161/188																		
91	0.009	0.009	0.27				0.931	1.017	1.017	0.38	53.77	3.5	62.0	65.5		0.010	0.003	
RB20-193/220																		
84	0.007	0.010	0.25				1.207	1.203	0.842	2.20	55.42	21.0	36.0	57.0		0.004	0.014	
RB21-005/032																		
69	0.011	0.012	0.27				0.616	0.633	0.580	0.02	40.80	0.1	287.9	288.0		0.026	0.018	

FILE CST-3-20

SAMPLE # 01	02	03	04	05	06	07	08	09	10	11	12	13	14	15	16	17	18	19
RA03-042/069																		
123	0.012	0.013	0.31				1.039	1.025	0.946	0.02	51.78	0.1	98.2	98.2		0.020	0.008	
RA03-127/154																		
121	0.012	0.014	0.32				0.967	1.008	0.864	0.01	51.53	0.0	102.5	102.6		0.004	0.004	
RA09-234/261																		
69	0.009	0.009	0.28				0.955	0.767	0.767	0.22	52.37	0.7	88.1	88.8		0.011	0.001	
RB14-025/052																		
84	0.009	0.010	0.16				1.003	0.936	0.842	0.19	50.00	0.6	129.3	129.9		0.004	0.004	
RB14-294/321																		
133	0.012	0.013	0.31				1.177	1.108	1.023	1.58	55.27	5.1	38.9	44.0		0.012	0.004	
RB20-089/116																		
134	0.012	0.013	0.32				1.158	1.117	1.031	0.69	53.89	2.2	62.1	64.2		0.010	0.013	
RB20-262/289																		
92	0.009	0.010	0.27				1.117	1.028	0.925	1.31	54.86	4.2	45.8	50.0		0.006	0.012	
RB21-361/388																		
124	0.012	0.015	0.32				1.072	1.033	0.827	1.41	54.53	4.5	51.6	56.1		0.006	0.003	
RB22-132/159																		
104	0.010	0.012	0.31				1.048	1.040	0.867	0.55	54.22	1.7	56.2	57.9		0.006	0.011	

APPENDIX D

TRIAXIAL TEST DATA

This appendix contains the results from the constant strain-rate triaxial tests (TRI). The parameters listed for each test are defined in Index B. As no displacement transducers were placed directly on the sample, the initial tangent modulus data given in Column 8 is based on the full sample strain. The strain and modulus data are measured values and have not been corrected for deformation of the synthane end caps. Corrected data are given in the text. TRI-3-5/.5 denotes those tests conducted at a nominal strain-rate of 10^{-3} s^{-1}, a temperature of -5°C, and a confining pressure/axial stress ratio of 0.5, etc. Triaxial sample numbers are defined in the same manner as compression sample numbers.

FILE TRI-3-5/.5

SAMPLE # 01	02	03	04	05	06	07	08	09	10	11	12	13	14	15	16	17	18	19
RA10-490/517 1830		0.590	5.80	1369	5.00	50.00	0.574		0.310	0.32	53.58	3.0	65.2	68.2	0.748	0.004	0.006	0.006
RA11-233/260 1544		0.440	4.20	979	5.00	50.00	0.461		0.351	0.04	52.34	0.4	86.4	86.7	0.634	0.007	0.016	0.016
RB13-286/313 1870		0.410	4.00	1432	5.00	50.00	0.650		0.456	1.34	55.14	12.7	39.5	52.2	0.766	0.010	0.003	0.004
RB16-124/151 1926		0.520	4.70	979	5.00	50.00	0.685		0.370	1.50	53.32	13.8	71.5	85.3	0.508	0.007	0.010	0.010
RB16-262/289 1294		0.350	3.10	1019	5.00	50.00	0.526		0.370	0.95	51.61	8.5	100.4	108.9	0.554	0.012	0.013	0.014
RB17-236/263 1838		0.420	3.90	1424	5.00	50.00	0.601		0.438	0.40	53.13	3.7	73.2	76.8	0.775	0.005	0.006	0.006
RB17-267/294 1584		0.600	5.60	1424	5.00	50.00	0.531		0.264	0.95	55.13	9.0	39.0	48.1	0.899	0.019	0.008	0.008
RB17-399/426 2602		1.010	10.60	1806	5.00	50.00	0.715		0.258	0.62	56.51	6.0	14.5	20.6	0.694	0.016	0.005	0.006
RA10-059/086 788		0.280	2.80	788	5.00	50.00	0.419		0.281	0.02	48.38	0.2	155.5	155.7	1.000	0.025	0.004	0.004

FILE TRI-5-5/.5

SAMPLE # 01	02	03	04	05	06	07	08	09	10	11	12	13	14	15	16	17	18	19
RA10-236/263																		
>330		>5.000	>5000				0.172			0.09	47.23	0.7	175.6	176.3		0.010	0.008	0.008
RA10-459/486																		
446		2.810	2810	442	5.00	5000	0.267		0.016	0.29	51.48	2.6	101.7	104.3	0.991	0.004	0.010	0.010
RA10-536/563																		
895		0.960	960.0	641	5.00	5000	0.297		0.093	0.51	55.76	4.9	27.4	32.3	0.716	0.010	0.010	0.010
RB13-255/282																		
362		0.650	660.0	350	5.00	5000	0.212		0.056	2.22	55.12	21.1	41.2	62.3	0.967	0.004	0.004	0.004
RB16-230/257																		
489		0.730	730.0	430	5.00	5000	0.209		0.067	1.43	53.11	13.1	75.1	88.2	0.879	0.005	0.004	0.004
RB16-330/357																		
350		0.910	910.0	330	5.00	5000	0.362		0.038	1.15	54.69	10.8	47.2	58.0	0.943	0.006	0.006	0.006
RB17-367/394																		
577		0.900	910.0	525	5.00	5000	0.287		0.064	1.31	56.42	11.0	16.9	27.9	0.910	0.011	0.009	0.010
RB17-443/470																		
959		0.520	540.0	625	5.00	5000	0.436		0.184	1.04	56.62	10.1	15.0	25.2	0.652	0.034	0.014	0.014
RA10-372/399																		
557		1.320	1340	485	5.00	5000	0.339		0.042	0.09	45.66	0.7	203.1	203.8	0.871	0.006	0.006	0.006

FILE TRI-5-5/.25

SAMPLE # 01	02	03	04	05	06	07	08	09	10	11	12	13	14	15	16	17	18	19
RA08-134/161																		
460		0.940	930.0	360	5.00	5000			0.049	0.03	51.12	0.3	107.6	107.9	0.783	0.009	0.000	0.000
RA08-166/193																		
427		0.790	750.0	310	5.00	5000	0.707		0.054	0.04	52.77	0.4	78.9	79.3	0.726	0.004	0.003	0.004
RA08-198/225																		
366		0.920	940.0	326	5.00	5000	0.168		0.040	0.16	51.22	1.4	106.1	107.5	0.891	0.009	0.007	0.008
RA08-259/286																		
515		0.580	590.0	334	5.00	5000	0.408		0.089	0.80	52.65	7.3	82.1	89.4	0.649	0.003	0.006	0.006
RB12-077/104																		
166		0.360	342.0	165	5.00	5000	0.217		0.046	1.24	54.60	11.7	48.9	60.6	0.994	0.004	0.004	0.004
RB12-163/190																		
555		1.000	999.0	377	5.00	5000	0.309		0.056	0.12	53.34	1.1	69.1	70.2	0.679	0.008	0.002	0.002
RB12-194/221																		
549		1.000	999.0	376	5.00	5000	0.245		0.055	0.33	53.75	3.1	62.3	65.3	0.685	0.009	0.009	0.010
RB13-066/093																		
286		0.450	444.0	230	5.00	5000	0.179		0.064	1.03	54.05	9.6	58.1	67.7	0.804	0.009	0.016	0.016
RB13-097/124																		
253		0.390	390.0	201	5.00	5000	0.194		0.065	1.21	53.73	11.2	64.0	75.2	0.794	0.010	0.006	0.006
RA08-290/317																		
573		0.790	820.0	402	5.00	5000	0.291		0.073	0.79	54.10	7.4	56.9	64.3	0.702	0.011	0.007	0.008

FILE TRI-3-20/.25

SAMPLE # 01	02	03	04	05	06	07	08	09	10	11	12	13	14	15	16	17	18	19
RA08-025/052 2125		0.610	6.00	1114	5.00	50.00	0.482		0.348	0.02	50.07	0.1	128.0	128.0	0.524	0.004	0.002	0.002
RA08-340/367 2467		0.700	7.20	995	5.00	50.00	0.334		0.352	1.10	56.46	3.6	17.7	21.4	0.403	0.031	0.012	0.012
RA11-078/105 1679		0.460	4.60	1679	0.46	4.60	0.428		0.365	0.02	50.95	0.1	112.6	112.7		0.006	0.002	0.002
RA11-127/154 1822		0.470	4.80	740	5.00	50.00	0.470		0.388	0.03	49.36	0.1	140.3	140.4	0.406	0.010	0.004	0.004
RB12-132/159 2475		0.650	6.40	1066	5.00	50.00	0.555		0.381	0.23	52.60	0.7	84.1	84.8	0.431	0.007	0.003	0.004
RB12-326/353 2157		0.610	6.30	1027	5.00	50.00	0.297		0.354	1.28	54.89	4.1	45.2	49.3	0.476	0.006	0.004	0.004
RB12-047/074 1974		0.610	6.10	788	5.00	50.00	0.546		0.324	0.81	53.36	2.5	71.4	73.9	0.399	0.003	0.006	0.006
RB12-239/266 2236		0.580	5.70	931	5.00	50.00	0.589		0.386	1.70	55.39	5.5	36.9	42.4	0.416	0.007	0.004	0.004
RB13-156/183 2332		0.690	6.90	1027	5.00	50.00	0.536		0.338	1.58	55.48	5.1	35.3	40.4	0.440	0.007	0.005	0.006

FILE TRI-5-20/.5

SAMPLE # 01	02	03	04	05	06	07	08	09	10	11	12	13	14	15	16	17	18	19
RA10-90/117																		
>740		>5.000	>5000				0.303			0.03	50.33	0.1	123.4	123.5		0.004	0.007	0.008
RA10-133/160																		
851		1.520	1530	851	5.00	5000	0.479		0.056	0.03	50.94	0.1	112.8	112.9	1.000	0.000	0.005	0.006
RA11-266/293																		
1039		0.700	710.0	772	5.00	5000	0.297		0.148	0.04	51.92	0.1	95.8	95.9	0.743	0.007	0.006	0.006
RB16-156/183																		
>573		>5.000	>5000				0.282			1.96	50.55	5.8	121.3	127.1		0.005	0.010	0.010
RB16-188/215																		
820		1.010	1030	820	5.00	5000	0.300		0.081	0.66	51.88	2.0	97.0	99.0	1.000	0.006	0.022	0.022
RB16-361/388																		
971		0.780	750.0	812	5.00	5000	0.318		0.124	1.00	55.71	3.3	30.7	33.9	0.836	0.025	0.004	0.004
RB16-432/459																		
1600		0.680	670.0	947	5.00	5000	0.452		0.235	1.47	56.53	4.9	16.9	21.7	0.592	0.015	0.010	0.010
RB17-191/218																		
963		1.390	1380	939	5.00	5000	0.386		0.069	0.53	53.11	1.6	75.5	77.1	0.975	0.007	0.013	0.014
RB17-335/362																		
1050		1.100	1110	955	5.00	5000	0.391		0.095	1.83	54.96	5.9	44.5	50.4	0.910	0.008	0.005	0.006

FILE TRI-3-20/.5

SAMPLE # 01	02	03	04	05	06	07	08	09	10	11	12	13	14	15	16	17	18	19
RA10-194/221																		
2674		0.610	5.40	1942	5.00	50.00	0.830		0.438	0.02	51.77	0.1	98.4	98.4	0.700	0.002	0.004	0.004
RA10-341/368																		
2578		0.790	7.80	1958	5.00	50.00	0.689		0.326	0.11	51.48	0.3	103.5	103.8	0.760	0.011	0.003	0.004
RA10-567/594																		
4011		0.880	8.50	2196	5.00	50.00	1.021		0.456	0.83	56.43	2.7	18.0	20.7	0.547	0.007	0.003	0.004
RB13-225/252																		
3008		0.680	6.60	1448	5.00	50.00	0.901		0.442	2.22	55.25	7.2	39.9	47.0	0.481	0.004	0.004	0.010
RB13-342/369																		
4584		1.000	9.40	2992	5.00	50.00	0.936		0.458	1.65	55.60	5.4	33.2	38.6	0.653	0.004	0.004	0.004
RB16-089/116																		
3374		0.490	4.50	3374	0.49	4.50	0.838		0.689	0.29	52.55	0.9	85.0	89.9		0.006	0.004	0.004
RB16-392/419																		
3629		0.910	9.00	1974	5.00	50.00	0.860		0.399	1.78	56.22	5.8	22.6	28.4	0.544	0.007	0.010	0.010
RB17-052/079																		
1210		0.210	2.00	1210	0.21	2.00	0.639		0.576	0.14	53.71	0.4	64.7	65.1		0.007	0.002	0.002
RB18-363/390																		
5602		1.200	12.00	2929	5.00	50.00	1.000		0.467	0.55	56.60	1.8	14.8	16.6	0.523	0.005	0.005	0.006

APPENDIX E

CONSTANT LOAD COMPRESSION DATA

This appendix contains the results from the constant load compression tests. Most variables have been defined in Index B, with the following exceptions: σ is the applied stress on the sample; $\dot{\varepsilon}_{min}$ (FS) is the strain-rate minimum determined from the full sample displacement, $\dot{\varepsilon}_f$ (FS) is the full sample strain at the strain-rate minimum or failure, t_f is the time to failure, and $\dot{\varepsilon}_e$ (FS) is the full sample strain-rate at the end of the test.

CONSTANT LOAD COMPRESSION TEST DATA

Sample No.	σ (lbf/in.^{2})	T (°F)	$\dot{\varepsilon}_{min}$ (FS) (s^{-1})	ε_f (FS) (%)	t_f (s)	$\dot{\varepsilon}_e$ (FS) (s^{-1})	$\dot{\varepsilon}_e$ (FS) (%)	t_e (sec)	S_i (°/oo)	ρ (lb/ft^3)	V_b (°/oo)	V_a (°/oo)	n (°/oo)	ISQ. (in.)	ESQ (in.)
BELLOFRAM TESTS															
RC31-473/500	100	23	8.47×10^{-8}	0.70	6.39×10^{4}	1.46×10^{-7}	2.10	3.33×10^{5}	1.94	56.87	19.0	10.5	29.6	0.012	0.005
RA02-036/063	100	23	1.65×10^{-7}	1.28	6.31×10^{4}	2.40×10^{-7}	4.35	2.20×10^{5}	0.01	49.89	0.1	129.2	129.3	0.004	0.003
RA02-086/113	100	23	1.47×10^{-8}	0.18	7.50×10^{4}	2.22×10^{-8}	1.15	5.69×10^{5}	0.02	51.45	0.2	102.0	102.2	0.005	0.000
RC28-158/185	100	23	4.45×10^{-8}	0.51	1.01×10^{5}	7.46×10^{-8}	2.75	5.13×10^{5}	0.79	55.12	7.5	39.1	46.6	0.003	0.009
RA06-368/395	100	23	7.78×10^{-8}	0.65	6.53×10^{4}	1.60×10^{-7}	2.64	2.42×10^{5}	1.22	53.26	11.2	72.3	83.5	0.004	0.011
RA02-268/295	100	23	6.31×10^{-8}	0.47	6.36×10^{4}	1.51×10^{-7}	4.85	5.81×10^{5}	0.26	54.07	2.4	56.7	59.1	0.003	0.005
RC31-383/410	100	23	2.77×10^{-8}	0.69	2.03×10^{5}	3.68×10^{-8}	2.10	6.67×10^{5}	1.69	56.62	16.5	14.5	31.0	0.005	0.007
RA01-047/074	100	23	9.12×10^{-7}	0.77	6.59×10^{3}	1.07×10^{-6}	2.82	2.75×10^{4}	0.02	48.52	0.2	153.1	153.3	0.007	0.003
RC28-322/351	100	23	6.70×10^{-8}	0.74	8.31×10^{4}	2.95×10^{-7}	6.57	4.92×10^{5}	1.51	55.12	14.4	40.2	54.6	0.008	0.004
MTS TESTS															
RC31-309/336	300	23	8.72×10^{-6}	0.45	3.02×10^{2}	1.65×10^{-4}	5.00	1.78×10^{3}	1.42	56.62	13.9	14.0	27.9	0.003	0.005
RC31-537/564	300	23	1.15×10^{-4}	0.55	4.22×10^{1}	1.40×10^{-3}	5.00	1.71×10^{2}	3.72	56.43	36.2	21.0	57.2	0.025	0.027
RC29-374/401	300	23	7.59×10^{-5}	0.22	1.59×10^{1}	1.15×10^{-3}	5.00	1.43×10^{2}	4.67	55.56	44.8	37.6	82.4	0.004	0.009
RC29-455/482	300	23	1.66×10^{-4}	0.20	8.29	2.08×10^{-3}	5.00	1.23×10^{2}	2.93	56.12	28.4	25.1	53.5	0.009	0.003
RC28-190/217	300	23	9.12×10^{-6}	0.49	3.98×10^{2}	2.09×10^{-4}	5.00	1.61×10^{3}	0.46	53.26	4.2	71.2	75.4	0.002	0.004
RC28-126/153	300	23	3.63×10^{-6}	0.64	9.12×10^{2}	1.09×10^{-5}	5.00	6.16×10^{3}	0.48	54.81	4.5	44.0	48.6	0.008	0.003
RA01-370/397	300	23	3.29×10^{-6}	0.80	1.68×10^{3}	8.96×10^{-6}	5.00	1.00×10^{4}	0.89	56.12	8.6	21.9	30.5	0.008	0.008
RA02-339/366	300	23	7.94×10^{-6}	0.55	3.31×10^{2}	7.94×10^{-5}	5.00	1.97×10^{3}	1.71	55.56	16.4	32.9	49.3	0.005	0.003
RC29-406/433	300	-4	3.03×10^{-5}	0.07	1.82×10^{1}	4.67×10^{-4}	5.00	3.29×10^{2}	3.87	56.12	12.7	26.4	39.1	0.005	0.012
RA06-432/459	300	-4	3.77×10^{-6}	0.35	6.65×10^{2}	1.60×10^{-6}	5.00	3.00×10^{3}	1.09	55.19	3.5	40.0	43.5	0.003	0.005
RC31-166/193	300	-4	1.20×10^{-6}	0.72	3.55×10^{3}	3.47×10^{-6}	3.94	1.89×10^{4}	0.70	55.06	2.3	41.8	44.0	0.006	0.007
RC29-148/175	300	-4	3.98×10^{-7}	0.38	3.98×10^{3}	3.09×10^{-7}	1.33	3.45×10^{4}	1.19	56.62	3.9	15.1	19.0	0.008	0.005
RA06-162/189	300	-4	2.09×10^{-5}	0.05	7.94	1.11×10^{-3}	5.00	3.30×10^{2}	0.10	50.63	0.3	118.4	118.7	0.012	0.008
RC31-247/274	300	-4	4.79×10^{-6}	0.17	2.63×10^{2}	1.85×10^{-4}	5.00	1.34×10^{3}	0.77	56.69	2.5	13.6	16.1	0.004	0.011
RA06-089/116	300	-4	2.01×10^{-6}	1.03	3.16×10^{3}	2.31×10^{-6}	4.20	1.59×10^{4}	0.03	50.38	0.1	122.7	122.8	0.007	0.005
RA06-463/490	300	-4	1.28×10^{-6}	0.83	4.57×10^{3}	1.51×10^{-6}	2.24	1.59×10^{4}	0.73	55.38	2.4	36.4	38.7	0.004	0.008
RC28-251/278	300	-4	7.4×10^{-7}	0.56	4.79×10^{3}	1.11×10^{-6}	1.17	1.18×10^{4}	2.58	56.50	8.5	18.6	27.2	0.006	0.004
RC31-089/116	600	-4	9.52×10^{-5}	0.13	6.75	3.11×10^{-3}	4.23	6.98×10^{1}	0.45	55.87	1.5	27.4	28.9	0.009	0.008
RA01-294/321	600	-4	6.92×10^{-5}	0.10	11.0	3.05×10^{-3}	3.80	1.00×10^{2}	1.39	55.13	4.5	41.4	45.8	0.004	0.007
RC31-505/532	600	-4	1.74×10^{-4}	0.18	7.59	5.32×10^{-3}	3.94	4.81×10^{1}	2.25	56.62	7.4	16.1	23.6	0.006	0.004
RC29-488/515	600	-4	6.92×10^{-5}	0.12	8.71	3.31×10^{-3}	2.95	6.64×10^{1}	2.64	55.94	8.6	28.5	37.1	0.008	0.005
RA02-299/326	600	-4	1.10×10^{-4}	0.12	12.0	3.92×10^{-3}	5.00	1.64×10^{2}	0.42	55.19	1.4	39.3	40.7	0.012	0.007
RA01-131/158	600	-4	5.75×10^{-5}	0.14	13.2	1.32×10^{-3}	1.23	6.68×10^{1}	0.02	51.88	0.1	96.6	96.6	0.004	0.003
RA06-297/324	600	-4	2.00×10^{-5}	0.10	12.0	2.75×10^{-3}	1.85	6.68×10^{1}	0.19	50.07	0.6	128.2	128.8	0.004	0.010
RC29-283/310	600	-4	1.00×10^{-4}	0.14	11.0	3.00×10^{-3}	3.45	8.23×10^{1}	2.33	56.12	7.6	24.9	32.5	0.007	0.002
RA02-128/155	600	-4	4.79×10^{-5}	0.15	17.4	1.10×10^{-3}	1.50	8.59×10^{1}	0.01	50.88	0.0	114.0	114.0	0.005	0.007

APPENDIX F

STATIC DETERMINATION OF YOUNG'S MODULUS IN SEA ICE

SHORT COMMUNICATION

COLD REGIONS SCIENCE AND TECHNOLOGY

STATIC DETERMINATION OF YOUNG'S MODULUS IN SEA ICE

Jacqueline A. Richter-Menge
Cold Regions Research and Engineering Laboratory
Hanover, N.H. (USA)

Numerous tests are being performed at the Cold Regions Research and Engineering Laboratory in Hanover, New Hampshire, to determine the mechanical properties of arctic sea ice. By far the most difficult measurement to obtain accurately has been the initial tangent modulus, given by the force displacement curve and interpreted as Young's modulus. The purpose of this communication is to re-emphasize a warning by Mellor (1983) that a reliable initial tangent modulus cannot be determined unless axial strain measurements are made directly on the test specimen.

In unconfined uniaxial constant-strain-rate compression tests, we successfully determined the initial tangent modulus by mounting direct current displacement transducers (DCDTs) directly on the ice sample (Mellor et al., in press). Two DCDTs were located in the center portion of the sample, measuring the axial displacement over a gauge length of 5.5 inches (14 cm). The output of the transducers was averaged and recorded on an x-y plotter and strip chart. An extensometer was also used to measure full-sample axial displacements and to provide a control signal for the closed-loop testing system. This extensometer, mounted between the bonded

end caps of the sample, measured displacements over a length of 10 inches (25.4 cm). The ice-mounted DCDTs were not used to control the strain rate because each test was designed to measure force-displacement characteristics to 5% full sample strain. At these large strains the sample undergoes gross deformations, making the readings from the DCDTs unreliable. Measurements from both the DCDTs and the extensometer were reliable to ± 0.5% of the reading for axial displacements greater than 0.0001 in. (2.54×10^{-3} mm). The axial strain measurements recorded by the DCDTs and the extensometer agreed very well up to peak load. The initial tangent modulus value was determined for each test using the initial slope of the force-displacement curve as recorded by the average of the DCDT measurements. Using the tangent modulus, we defined a Young's modulus which, on an average, agreed quite well with previous results (Cox et al., in press).

We were also interested in investigating the effect of confinement on the compressive behavior of sea ice. This included the influence that confinement might have on the initial tangent modulus. A conventional triaxial cell, pictured in Figure 1, was developed for maintaining a constant ratio between the applied axial stress and the confining pressure ($\sigma_1 > \sigma_2, \sigma_3$; $\sigma_2 = \sigma_3$; $\sigma_2/\sigma_1 = \text{constant}$). On-ice axial displacement measurements were complicated by the fact that the ice sample was to be completely immersed in a high-pressure fluid. Considering the favorable agreement between the full sample (extensometer) and on-ice (DCDTs) axial displacement measurements in the uniaxial tests, we felt that a feasible alternative would be to measure the full-sample strain externally.

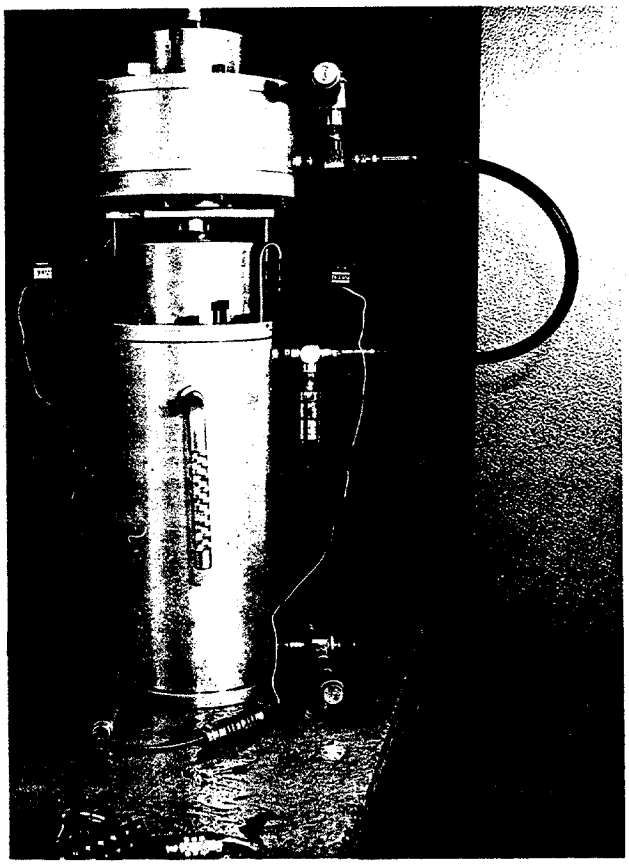

Figure 1: Triaxial cell

This alternative meant, however, that the recorded displacements would include ice end effects, end cap compression, and closure across an interface. The end cap compression was minimized by using aluminum end caps, which were very stiff relative to the ice. The interface of closure occurred between the loading piston and the top end cap of the sample. At this interface, we often had an imperfect contact due to a lack of parallelism in our machined samples. To correct for any lack of squareness, we measured the variation in sample height by running a comparator around the perimeter of the top end cap. Steel shimstock of the required gauge was then placed at the low point of the top end cap. Earlier evaluation of the uniaxial compression tests indicated that the use of shimstock was an effective means of compensating for the machining error.

It was still necessary to test the reliability of the external measurement more thoroughly. A series of three uniaxial compression tests was performed on ice samples at -10°C. Two of the samples were tested at a constant strain rate of 7.14×10^{-6} s^{-1}, and one was tested at a rate of 7.14×10^{-4} s^{-1}. The ice samples were instrumented with DCDTs and an extensometer as described earlier. In addition, a pair of extensometers was mounted between the loading ram and the top end cap as shown in Figure 2. These extensometers were 180° apart, with one extensometer located at the low point of the upper end cap. Axial displacement measurements were recorded by the DCDTs mounted on the ice sample, the extensometer mounted between the bonded aluminum end caps, and the extensometers mounted across the shimmed interface. A comparison was then made of the initial portion

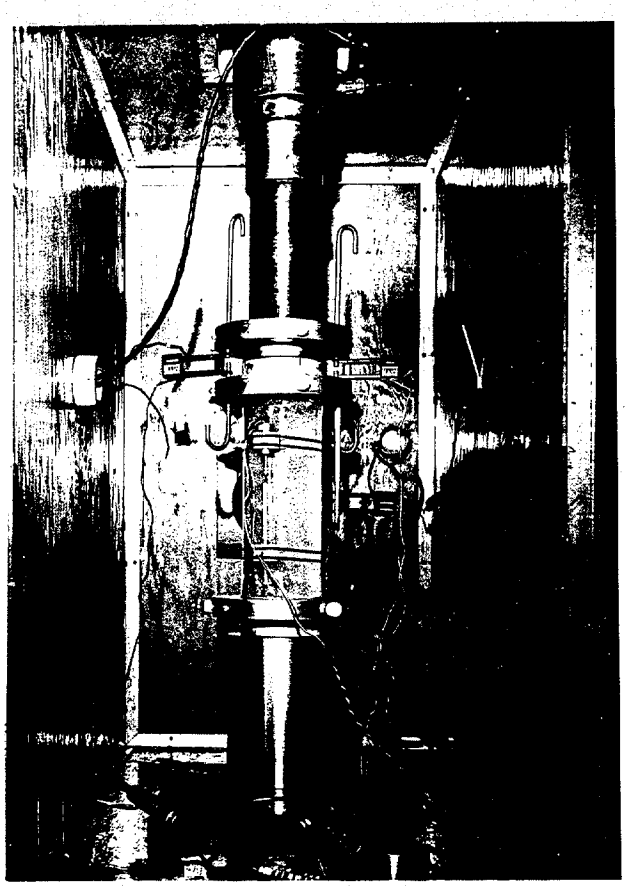

Figure 2: Test configuration to determine effect of closure.

of the force-displacement curves using 1) the DCDT output and 2) the full-sample extensometer output plus the displacement measurement across the shimmed interface. The latter curve simulated the axial displacements that would be obtained using the externally mounted extensometers on the triaxial cell.

The results are presented in Table 1, and Figure 3 shows a representative pair of curves. The initial tangent modulus values reported in Table 1 were defined by the initial slope of the recorded force-displacement curve. $E_i(GL)$ represents the modulus value determined using the axial displacement measured by the ice-mounted DCDTs, and $E_i(FS+P)$ is the modulus value determined using the full-sample and interfacial displacements. The percent reduction indicates the effect that external measurement techniques would have on the modulus value. The squareness value denotes the comparator readings on each sample and hence the shimstock used to correct for machining error. It is apparent that while the displacement across the shimmed interface is small, it is significant during the initial portion of the test, where displacements in the ice are also small. If we used the externally mounted extensometers in the triaxial tests, we could expect the initial tangent modulus value to be reduced to as much as one half the value that would be obtained in a uniaxial compression test on the same sample. As the axial force increases, the ice displacement continues to increase while the displacement across the shimmed interface remains constant. Therefore, the closure has a significant influence only during the initial portion of the test. Measurement of the displacement between

Table 1. Test results.

Sample No.	E_i(GL) [GPa]	E_i(FS+P) [GPa]	Reduction [%]	Squareness [inches]
$\dot{\varepsilon} = 10^{-5}\ s^{-1}$, T = -10°C				
12B	5.61	3.24	42	0.007
14C	5.14	4.26	17	0.009
$\dot{\varepsilon} = 10^{-3}\ s^{-1}$, T = -10°C				
1C	7.19	4.53	37	0.003

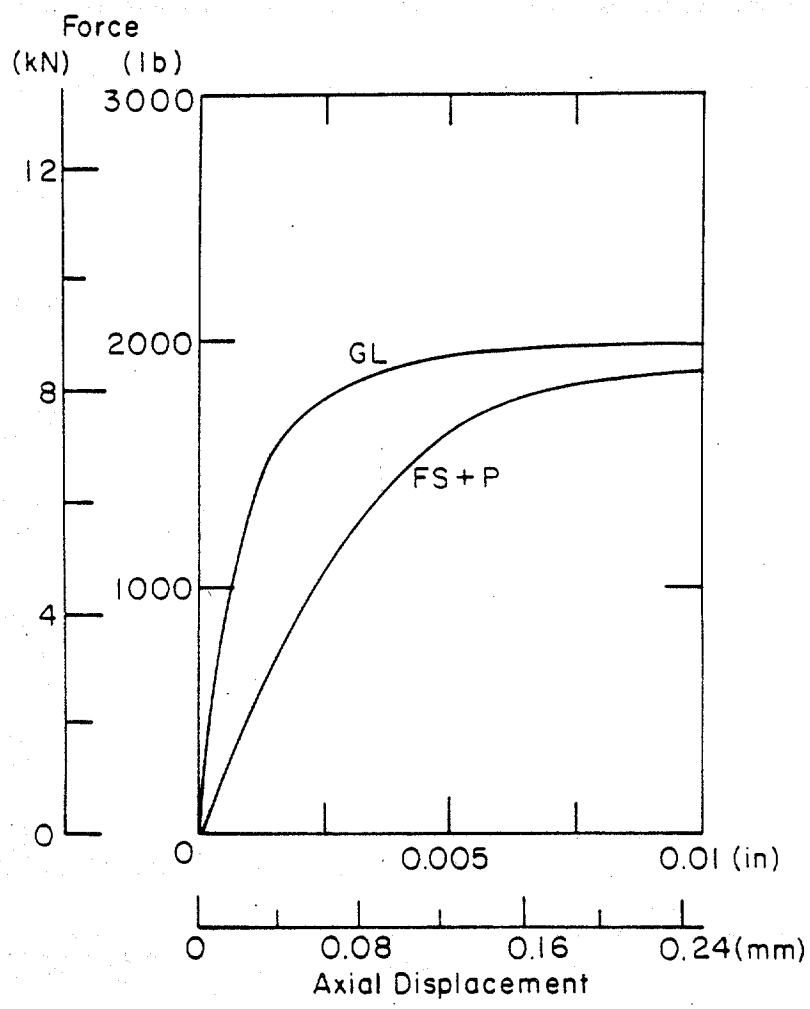

Figure 3a: Force-displacement curve for Sample 12B, $T = -10°C$, $\dot{\varepsilon} = 7.14 \times 10^{-6}\ S^{-1}$.

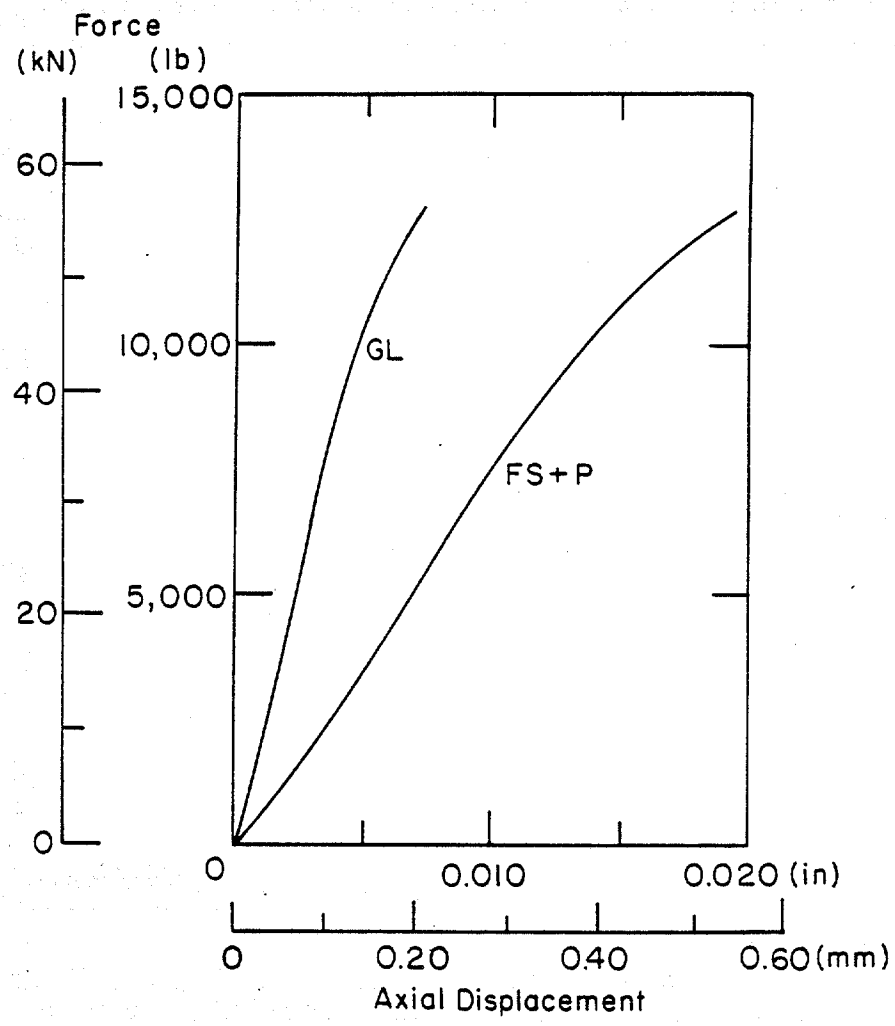

Figure 3b: Force-displacement curve for Sample 1C, $T = -10^{\circ}C$, $\dot{\varepsilon} = 7.14 \times 10^{-4}\ S^{-1}$.

the loading ram and the top end cap indicates that the shimstock reduces the net closure at this interface to less than 0.002 inches.

These tests do indicate that displacement measurements made on the ice itself are necessary for reliably determining the initial tangent modulus, and hence Young's modulus. As a result of this study, modifications will be made to our triaxial cell so that it can accomodate an instrumented sample. Displacement transducers that can withstand high pressures, low temperatures and immersion will be used to measure the axial strain. These transducers will be mounted on the ice and the electrical signals that they transmit will pass through bulkhead connectors located in the cell wall. Once these changes have been completed, tests will be performed on ice samples to demonstrate the reliability of the displacement measurements.

ACKNOWLEDGEMENTS

The author is grateful to Mr. David Cole, Dr. Gordon Cox and Mr. Glenn Durell for many helpful suggestions. This work was supported by the U.S. Army Cold Regions Research and Engineering Laboratory, In-House Laboratory Independent Research (ILIR) DA Project 4A161101A91D, Work Unit 412, Triaxial Testing of Sea Ice.

REFERENCES

Cox, G.F.N., J.A. Richter, W.F. Weeks, M. Mellor and H.W. Bosworth (In press) Mechanical properties of multi-year sea ice, Phase I: Test results. U.S. Army Cold Regions Research and Engineering Laboratory, CRREL Report.

Mellor, M. (1983) Mechanical behavior of sea ice. U.S. Army Cold Regions Research and Engineering Laboratory, Monograph 83-1.

Mellor, M., G.F.N. Cox and H.W. Bosworth (In press) Mechanical properties of multi-year sea ice: Testing techniques. U.S. Army Cold Regions Research and Engineering Laboratory, CRREL Report.